MAGNETIC IMAGING OF MICROMETER AND NANOMETER-SIZE MAGNETIC STRUCTURES AND THEIR FLUX-PINNING EFFECTS ON SUPERCONDUCTING THIN FILMS

A Dissertation

by

ALI ESAD ÖZMETIN

Submitted to the Office of Graduate Studies of
Texas A&M University
in partial fulfillment of the requirements for the degree of

DOCTOR OF PHILOSOPHY

May 2009

Major Subject: Materials Science and Engineering

MAGNETIC IMAGING OF MICROMETER AND NANOMETER-SIZE MAGNETIC STRUCTURES AND THEIR FLUX-PINNING EFFECTS ON SUPERCONDUCTING THIN FILMS

A Dissertation

by

ALI ESAD ÖZMETIN

Submitted to the Office of Graduate Studies of
Texas A&M University
in partial fulfillment of the requirements for the degree of

DOCTOR OF PHILOSOPHY

Approved by:

Chair of Committee,	Donald G. Naugle
Committee Members,	Ibrahim Karaman
	Igor Lyuksyutov
	Joseph Ross
Intercollegiate Faculty Chair,	Tahir Cagin

May 2009

Major Subject: Materials Science and Engineering

ABSTRACT

Magnetic Imaging of Micrometer and Nanometer-size Magnetic Structures and Their Flux-Pinning Effects on Superconducting Thin Films. (May 2009)

Ali Esad Özmetin, B.S., Bogazici University;

M.S., Texas A&M University

Chair of Advisory Committee: Dr. Donald G. Naugle

In this work the interactions between neighboring superconducting thin film and ferromagnetic structures, i.e. superconductor-ferromagnet hybrid systems, were studied. A type-II superconducting thin film ($Pb_{82}Bi_{12}$), was deposited in close proximity to various ferromagnetic structures. These magnetic structures include: (i) alternating iron-brass shims of $275\mu m$ period, (ii) an array of $4\mu m$ wide Co stripes with smaller period ($9\mu m$), (iii) a square array of 50nm diameter, high aspect ratio (5-7) Ni rods with 250nm period. Measurements of critical transport current (I_C), resistance ($R_H(T)$) and second critical field (H_{C2}) are reported. A variety of novel effects (enhancement of (I_C) and (H_{C2}), matching field effect, field compensation effect, and large hysteresis) are also reported. Using measurements on thin superconducting films atop a Co stripe array with a $9\mu m$ period, a superconductor-ferromagnet hybrid device (a mechanical superconducting persistent switch) is proposed.

In addition, scanning Hall probe microscopy (SHPM) and other imaging techniques were used to characterize the magnetic properties of the systems mentioned. The SHPM was also used to acquire B-H and M-H curves. An additional sharp magnetic needle and electromagnetic coil assembly intended for micromanipulation of small magnetic particles and individual cells was also characterized.

To my wife, Jennifer, for her endless support

ACKNOWLEDGMENTS

Completion of this dissertation would have been impossible without the contribution of many people. First and foremost, I would like to express my heartfelt gratitude to my adviser, Dr. Donald G. Naugle, for his support, leadership and patience. He not only mentored me through the difficulties of experimental physics but also set an example to become a well-rounded scientist. I am gratefull to Dr. K. D. D. Rathnayaka for his tireless technical assistance. Thanks are due to Dr. Igor Lyuksyutov for sharing his deep knowledge on the subject.

I must acknowledge my colleagues, Dr. KyongWang Kim, Dr. Zuxin Ye, Hangil Lee and Haidong Liu for their help and contribution and Dr. Naugle's group as a whole for being great team players. I would like to thank Dr. Jun Zou and Dr. Murat Yapici for their cooperation.

I am deeply indebted to my wife, parents, family and friends for their love, support and encouragement. Without them none of this would have been possible. Countless thanks be to God, the Master of this universe that we love studying so much, for providing me the patience, opportunity and skills to finish this work.

TABLE OF CONTENTS

CHAPTER Page

LIST OF FIGURES

FIGURE Page

FIGURE Page

FIGURE Page

FIGURE Page

FIGURE Page

CHAPTER I

INTRODUCTION

Brief Review of Superconductivity and Magnetism

The microscopic theory of superconductors (SC) was first proposed by J. Bardeen, L. Cooper, and R. Schrieffer [1] in what is now known as the BCS theory. In the qualitative description of the BCS theory, electrons act as pairs coupled by lattice vibrations in the material. This coupling is due to the electron - phonon interaction, where phonons are the quanta of lattice vibration energy. An electron in the cation lattice will distort the lattice around it, creating an area of greater positive charge density around itself. Another electron is then attracted to this charge distortion. These electrons are thus indirectly correlated to each other and form a bound state of two electrons. These bound electron pairs are called Cooper pairs. Although single electrons obey the Pauli exclusion principle, which forbids electron-like particles from being able to occupy the same quantum state, and are classified in Fermi statistics, the pairs of electrons behave more like Bosons which can condense into the same energy level. Due to this behavior, Cooper pairs at sufficiently low temperature, form a large Bose-Einstein condensate. A finite amount of energy is needed to break these bounded electrons (Cooper pairs) apart into two independent electrons. This means unlike electrons in a normal metal, where an arbitrary small amount of energy can be added or removed, there is an "energy gap". Cooper pairs have slightly lower energy than a single electron state therefore move through the lattice relatively unaffected by thermal vibrations. This effect is also what makes them feel no resistance when traveling through the lattice, therefore it makes the material

---

The journal model is *Journal of Magnetism and Magnetic Materials*.

a "perfect conductor" [2, 3].

Diamagnetism and Meissner Effect

If a perfect conductor is initially in a zero magnetic field and later the field is turned on, Faraday's Law of induction predicts the formation of eddy currents that cancel the magnetic field on the inside resulting in a time independent field. However, in a SC the magnetic field inside is not only time independent, but also it is zero thus exhibiting perfect diamagnetism (DM).

The field configuration inside the SC which minimizes the free energy must satisfy the condition first proposed by F. & H. London

$$h + \lambda_L^2 \nabla^2 h = 0 \tag{1.1}$$

and, combined with Maxwell's equations, Eqn. 1.1 allows one to calculate the distribution of fields and currents within the superconductor. The London penetration depth is defined as

$$\lambda_L = [\frac{mc^2}{4\pi n_s e^2}]^{1/2} \tag{1.2}$$

By applying London's equation to h and J_s that are related by Maxwell's equations one ends up with a solution of the field distribution for a semi-infinite slab with the field parallel to the surface of the form

$$h(z) = h(0)exp(-z/\lambda_L) \tag{1.3}$$

where x and z are the position inside the SC. Since the penetration depth λ_L is small in all cases, a weak field does not effectively penetrate into the specimen. In other words, field lines are excluded from the SC. This effect is called the Meissner-Ochsenfeld effect and was first experimentally observed by Meissner and Oschsenfeld

in 1933 [4]. The result can be generalized to any macroscopic system of arbitrary shape.

Two Kinds of Superconductors

The velocities of two electrons are correlated within a certain range $\xi_0 = \frac{\hbar v_F}{\pi \Delta}$, called the coherence length, where v_F is the Fermi velocity and 2Δ is the energy gap. h and J_s vary on a scale λ_L according to Eqn. 1.3, thus London's equation holds only for $\lambda_L >> \xi_0$. For non-transition metals v_F is large ($v_F > 10^8 cm/sec$) therefore, the coherence length is large ($\xi_0 > 10^4 \mathring{A}$). Consequently, the London equation (Eqn. 1.1) does not apply. Although they still show the Meissner effect, calculation of λ_L requires more sophisticated derivations which were first suggested by Pippard [5]. This kind of SC is classified as a SC of the first type (Type I). On the other hand for transition metals and inter metallic compounds, λ_L is large and v_F is small, ($v_F > 10^6 cm/sec$) therefore ξ_0 is also very small ($\xi_0 \sim 50 \mathring{A}$) consequently Eqn. 1.1 is applicable. This kind of SC is called a London SC or SC of the second kind (Type II).

Magnetic Properties of Type I Superconductors

A complete flux expulsion is observed when the applied field is less then a certain critical field $H < H_c$, but when H reaches H_c the field becomes uniformly distributed across the crossection and SC is destroyed. Therefore a Type I SC displays perfect diamagnetism, provided that the field is smaller than the critical field.

Magnetic Properties of Type II Superconductors

Type II superconductors do not exhibit perfect DM except for very weak applied fields $H < H_{C1}$. On the other hand, they show partial flux expulsion maintaining the superconducting state within a certain field range $H_{C1} < H < H_{C2}$, but beyond the

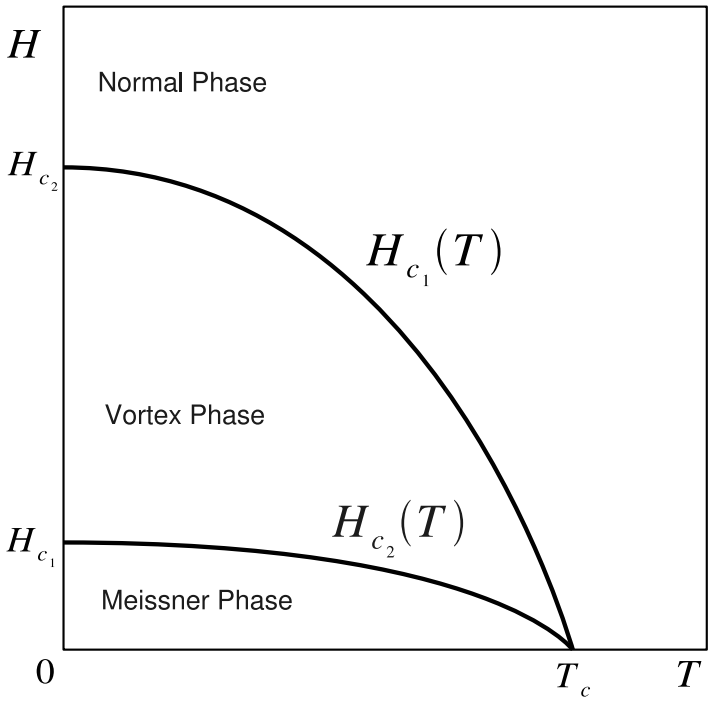

Fig. 1. Vortex state phase diagram.

value H_{C2} of field, flux expulsion seems to vanish, although the SC state remains at the sample surface below a third field H_{C3}. Surface SC vanishes too above H_{C3}.

Vortex State

When the applied field is in the range $H_{C1} < H < H_{C2}$, the magnetic field starts to partially penetrate the SC. Partial flux penetration was first experimentally observed by Shubnikov in 1937 (Fig. 1). This phase is called the Shubnikov or Vortex state. In this phase, the applied field penetrates the specimen through quantized flux tubes called vortices. Each vortex has a normal core of radius on the length scale of coherence length ξ_0 and a supercurrent encircles this normal core. Supercurrent around each vortex generates one flux quantum of magnetic flux $\phi_0 = \frac{ch}{2e} = 2 \cdot 10^{-7} G/cm^2$ over the length scale of λ.

In the vortex state, the presence of vortices drastically modifies the magnetic and transport properties of the superconductor. In the case of an applied current density $\vec{J}$ each vortex feels a Lorenz force $\vec{F_L}$ perpendicular to the current density and the applied field $\vec{B}$ [6].

$$\vec{F_L} = \vec{J} \times \frac{\phi_0 \hat{n}}{c} \tag{1.4}$$

In the absence of a balancing pinning force, the vortices will start moving in the direction of the Lorenz force. As a result, moving vortices induce an electric field $\vec{E}$ along the direction of the current density

$$\vec{E} = \vec{B} \times \frac{\vec{v}}{c} \tag{1.5}$$

where $\vec{v}$ is the velocity of the individual vortices. If a viscosity-like relation between the force $\vec{F}$ and the velocity $\vec{v}$ is assumed $\vec{F} = -\alpha\vec{v}$, using Eqn. 1.4 and Eqn. 1.5 a simple expression for magneto-resistance can be calculated.

$$\rho = \frac{E}{J} = \frac{B\phi_0}{c^2\alpha} \tag{1.6}$$

It can be concluded that there will be a form of resistive dissipation proportional to the applied field unless the vortices are prevented from moving or in other words pinned.

In situations where the pinning forces are larger than the Lorenz force acting on the vortex, it will stay pinned in a particular location. These locations are called the pinning sites. Depending on the pinning energy and the vortex-vortex interaction, vortices can either stay in their random pinning sites forming a vortex glass or form an ordered lattice. This ordered lattice is referred to as the vortex lattice or Abrikosov Lattice [7, 8]. As the field or the current density increases more and more vortices will leave their pinning sites and start moving. Eventually, all the vortices will enter a

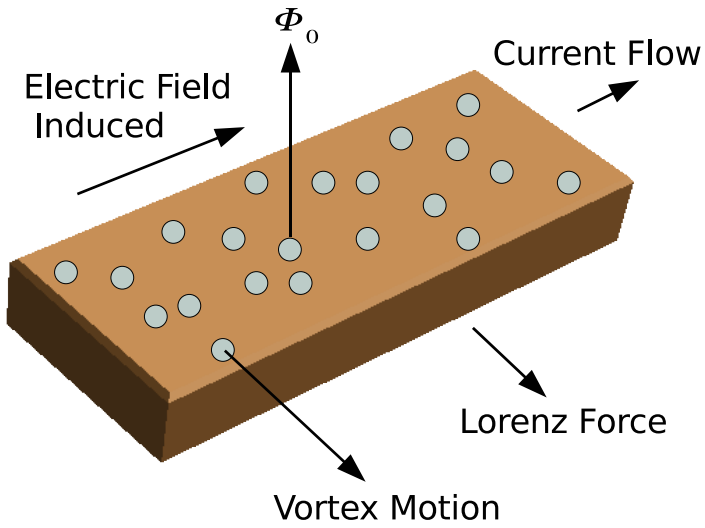

Fig. 2. Vortex motion.

steady flow state, in other words the superconductor will enter a vortex liquid phase.

Superconductor and Ferromagnet Hybrid Systems and Novel Effects

As discussed in the previous section, magnetism and superconductivity are competing orders. Suppression of SC by a neighboring FM can be via either the stray field of the FM or the injection of spin to the SC by splitting the Cooper pairs due to the exchange field of the FM. On the other hand, FM is also suppressed due to the field generated by super currents. Within the last decade the interplay between ferromagnetic (FM) and superconducting systems have been studied by experimental groups [9, 10, 11, 12, 13] focusing on transport properties, and also imaging techniques have been employed [14, 15, 16]. Two comprehensive reviews are available by Lyuksyutov and Pokrovsky [17], and the Schuller group [18].

In this study, arrays of FM structures creating magnetic modulation (artificial pinning sites) on a SC thin film deposited above the FM structures, have been the

focus of research. Arrays of FM stripes and high aspect ratio rods have been fabricated and their effects have been studied in various length scales ranging from micrometer to nanometer size. Due to the relatively high permeability of magnetic materials such as Co, Fe, Ni and permalloy these periodic structures channel the applied magnetic field and create a periodic modulation of magnetization. In cases of high aspect ratio FM structures, once the FM is magnetized, it preserves its out-of plane magnetization, even in the absence of an applied field. These artificial magnetic field modulations result in various exotic behaviors and novel phenomena.

Magnetization Controlled and Magnetization Induced Superconductivity

It has been shown that it is possible to switch the SC on and off by changing the direction of magnetization in FM structures [19, 20, 21]. Depending on their intrinsic or shape anisotropy, FM structures will have a preferred magnetization direction, but this can be modified by applying an external field. Therefore the SC in a hybrid system can be controlled by changing the magnetization direction of the FM structures.

Also, due to relative high permiablity of FM structures, the applied field is effectively channeled through the FM materials. The ratio of the flux lines channeled through the FM depends on the size and the period of these structures and can be calculated as well as measured with scanning Hall probe microscope. This channeling effect continues as the applied field is increased until the particular FM material reaches saturation. Using this property, hybrid systems can be designed in such a configuration to create high and low magnetic field regions on the SC (Fig. 3). If this field variation is strong enough, parts of the SC can be driven normal resulting in an anisotropic dependence of SC on current direction.

In the case of FM structures fabricated in close proximity to the SC film, the

requirement that the net flux due to the individual magnetic feature be zero, the field in between the magnets are in opposite direction compared to that of the magnets. This negative field can be compensated as the applied field is increased, creating a counter intuitive re-emergence of superconductivity (Fig. 4).

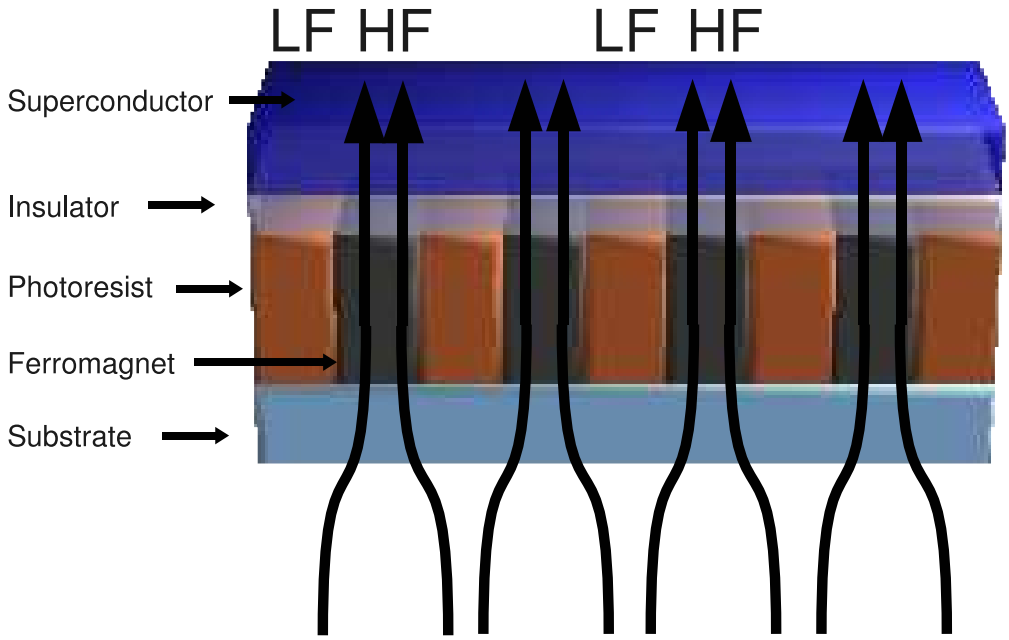

Fig. 3. Illustration of applied field channeling and resulting high and low field regions.

Enhancement of Superconducting Properties and Vortex Pinning

SC properties such as H_{C2} and J_C are strongly field dependent. It is possible to enhance these properties in hybrid systems with respect to a control sample consisting of an isolated SC by creating artificial regions of high and low field inside the SC film (Fig. 3). Although in the high field regions SC is either weakened or destroyed, in the low field regions locally SC persists. Therefore there are regions of the sample that are still SC even at higher values of H. In other words the apparent H_{C2} for

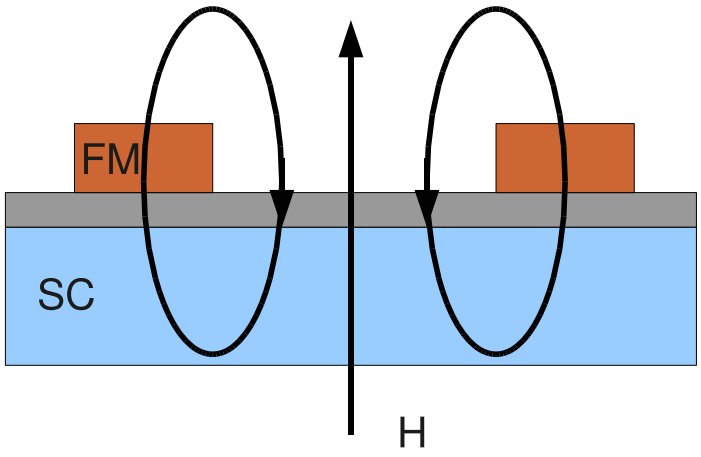

Fig. 4. Illustration of the field compensation effect.

the hybrid system is increased. Also with careful consideration of FM structure size and SC order parameters this field modulation can effectively pin SC vortices. Thus higher values of current can be passed through the SC film without creating vortex motion. This means enhancement of SC overall (both H_{C2} and J_C).

Field Matching Effect

In hybrid systems with periodic arrays of FM structures, as the magnetic field is scanned periodic oscillations in resistance $R(H)$ and critical transport current $I_C(H)$ are observed [22, 23, 24]. This observation is attributed to an increase in pinning when the vortex lattice is commensurate with the lattice of pinning centers. When the applied field generates integer multiples of flux quanta per unit cell of pinning sites, the pinning becomes stronger. As a result a decrease in $R(H)$ and an increase in $I_C(H)$ is observed for field values that are integer multiples of flux quanta per area of unit cell of pinning sites. Since the vortices usually prefer to form a hexagonal lattice, this effect is strongest when FM lattice is hexagonal or triangular.

CHAPTER II

SAMPLE FABRICATION

Construction of micrometer and nanometer size magnetic samples, and deposition of various superconductor magnetic hybrid systems require two basic steps of fabrication. These fabrication steps are patterning various different photoresists on a silicon wafer or glass substrate and later filling these patterned structures with magnetic materials such as Co, Ni or permalloy. Thermal evaporation was used to deposit a superconducting thin film. I mainly used a well studied type-II superconductor, a lead - bismuth alloy ($Pb_{82}Bi_{18}$) for fabricating the superconducting thin films. Details of these techniques are explained in next sections.

Patterning the Sample

Lithography is a printing technique invented in the late 18^{th} century in Europe. Early lithography used water soluble substances, such as gum Arabic, to design a negative version of the desired pattern on a smooth limestone. Later, water is applied to stick to gum Arabic and seal it. Limestone then is pressed against the paper to leave oil based dyes on the paper surface with the desired pattern. This idea of selectively applying desired agents on a smooth surface has remained virtually unchanged for nearly three centuries.

Photolithography and electron beam lithography refer to two different lithographic methods used for different feature sizes. In today's technology, photolithography can comfortably be used for feature sizes down to 1μm. For features smaller than 1μm, interference of ultra-violet light causes problems and photolithography becomes unreliable; consequently, electron beam lithography is used for smaller feature sizes. Accelerated electrons have smaller wavelength due to their high energy. Thus,

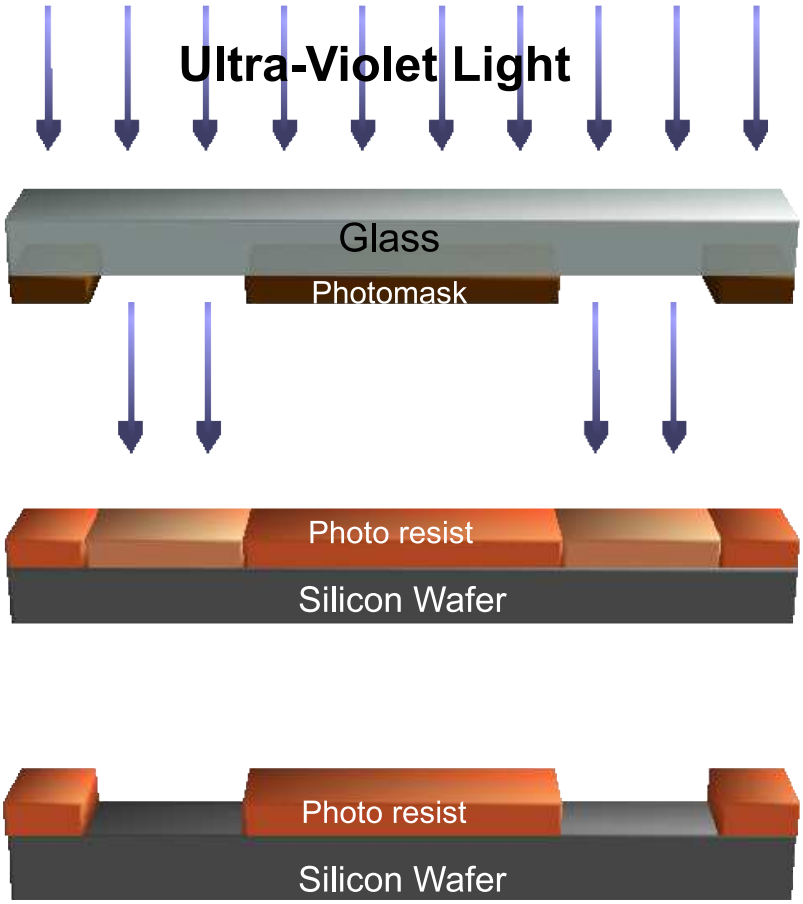

Fig. 5. Photolithography.

interference happens at a smaller length scale.

Photolithography

The photolithography technique typically starts by fabricating a photo mask to be used as a master to transfer the desired pattern onto a substrate. Later, the appropriate photoresist is spin coated on a silicon wafer and soft baked. There are two types of photoresists used (positive and negative). One of these types is chosen depending on the area of the pattern desired to be removed. A photomask is placed on the substrate and ultra-violet light is applied. The photomask acts as a shadow mask

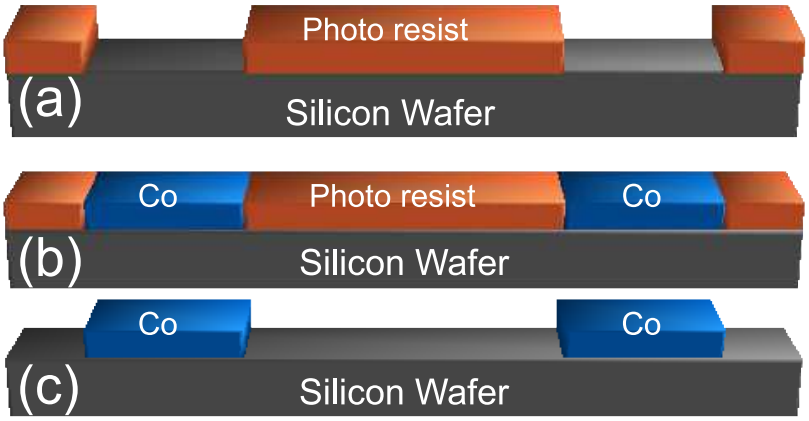

Fig. 6. Photolithography processes (a) etching exposed resist, (b) deposition, (c) photoresist removal.

and shields desired regions from UV-light (Fig. 5). Regions that are exposed to UV light change their chemical composition and become vulnerable to specific etchants. These regions are etched and the pattern becomes ready for deposition after a hard baking procedure (Fig. 6). Details of the deposition procedure are explained in the following sections. Finally, a different solvent is used to remove the photoresist altogether. This last removal step was deliberately omitted in some of the samples I have fabricated in order to have a continuous and smooth sample surface, leaving the deposited magnetic material embedded in the photoresist polymer (Fig. 7,8).

In this study, various types of photoresists were used. For low temperature applications SU(8) group photoresists are ideal due to their ability to stay intact at all temperatures down to 4K. If coated with small thicknesses, photoresist AZ-5214 can also be used for low temperature applications. The other photoresists generally crack or shatter at around 100 K, possibly due to having a different thermal expansion coefficient from the underlying substrate.

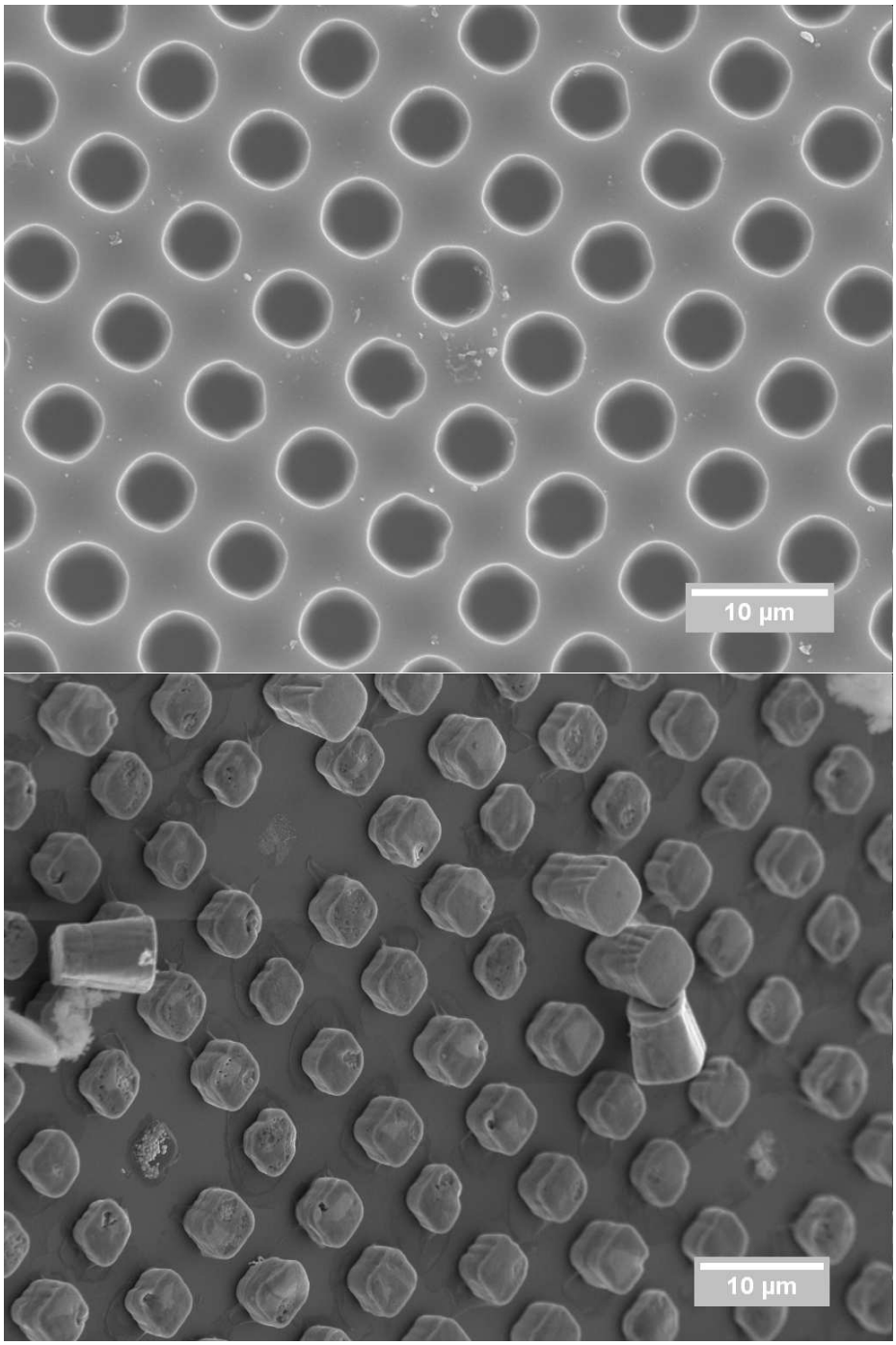

Fig. 7. (Upper) Nearly filled 4μm permalloy dots embedded in photoresist. (Lower) Free standing permalloy dots after photoresist removed (imaged at 45^o angle).

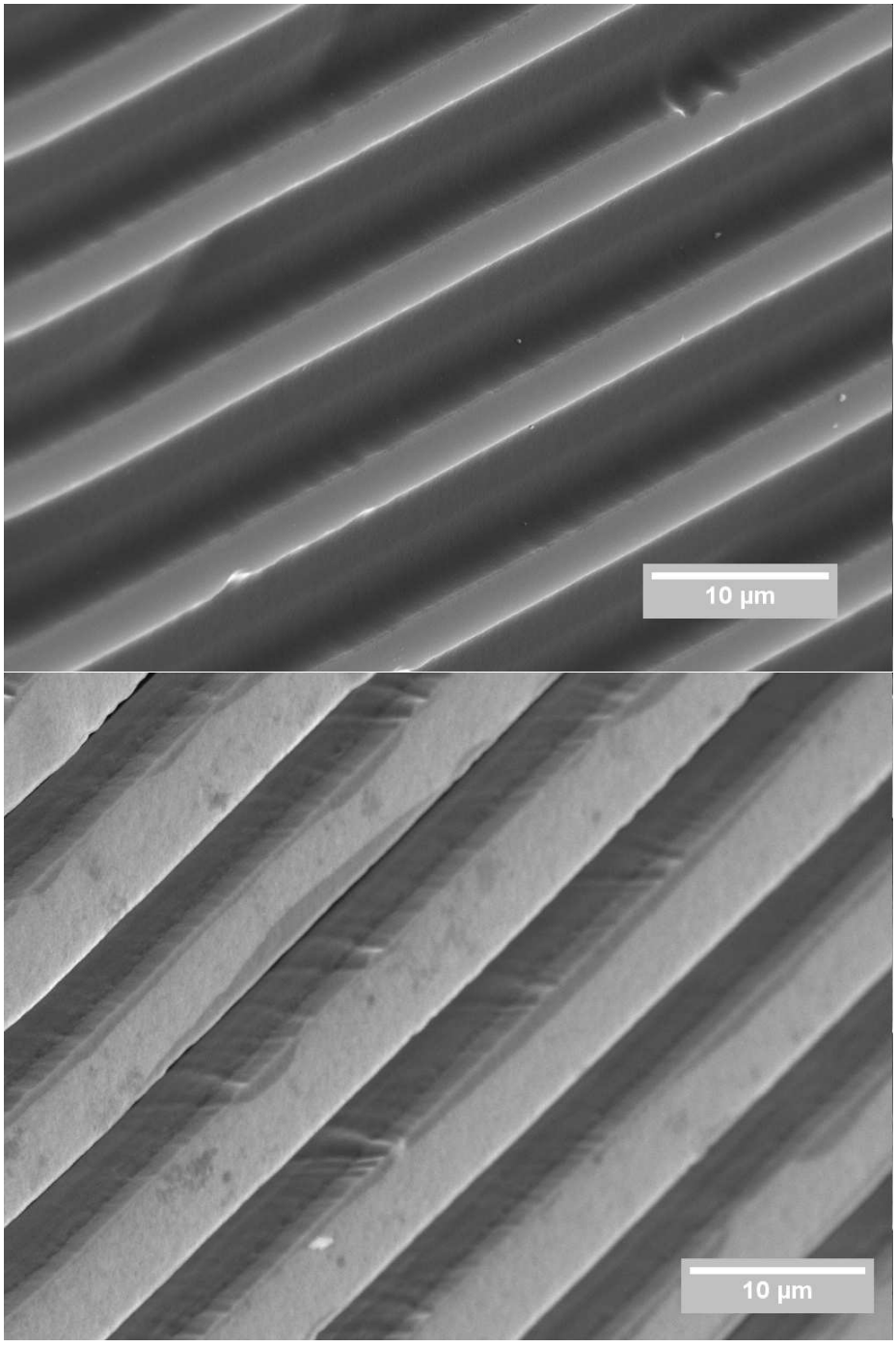

Fig. 8. (Upper) 5μm trenches nearly filled with permalloy embedded in photoresist. (Lower) Free standing permalloy walls after photoresist is removed (imaged at 45^o angle).

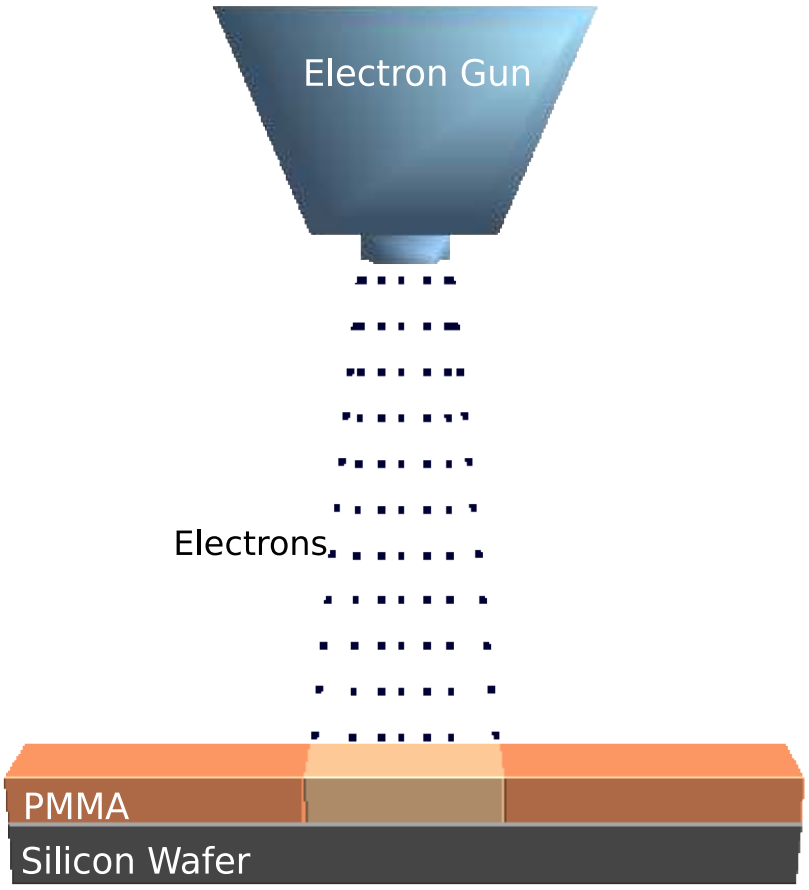

Fig. 9. Electron beam lithography.

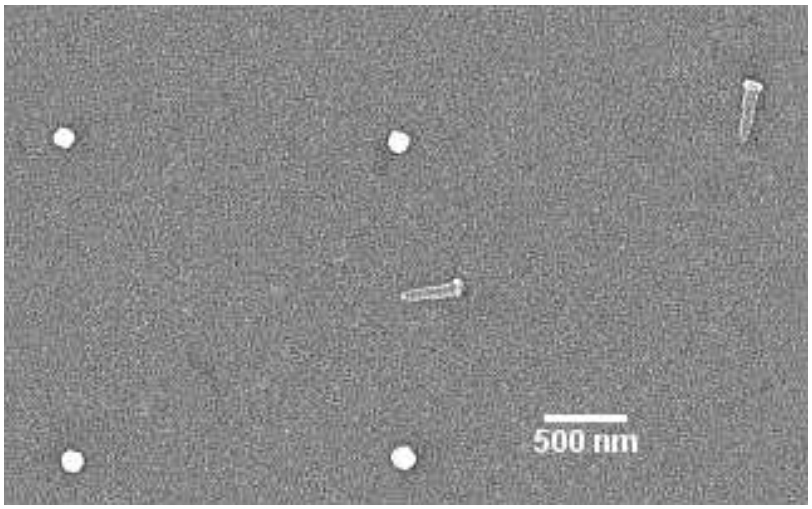

Fig. 10. Ni nano-dot array fabricated by electron beam lithography.

Electron Beam Lithography

Electron beam lithography (generally referred as e-beam lithography), is very similar to photolithography, with UV light replaced by a controlled beam of electrons. Using electrons resolves the problem of interference and therefore makes fabricating significantly smaller feature sizes possible (Fig. 9). It also makes photomasks unnecessary as the electron beam is focused and scanned directly on the resist with the help of a set of electromagnetic lenses. Using e-beam lithography, feature sizes around 50 nm have been successfully patterned (Fig. 10).

On the other hand, e-beam lithography poses a unique set of challenges. Depending on the type of resist used, charged electrons can collect and deflect the incident electron beam degrading the feature shape and size. In this study we used PMMA as the choice of resist. Also, lithography quality sharply depends on how well the e-beam is focused. This limits the size of the area to be patterned, as the beam scans further away from the original focus point, the e-beam becomes defocused. Typically, for every 100μm x 100μm section of the array to be written the user must refocus

the e-beam. Therefore, writing large arrays of dots and trenches proved to be rather difficult. Aligning a magnetic sample to be imaged in a low temperature SHPM system requires at least a 0.5 mm x 0.5 mm array size. This translates to refocusing the electron beam 25 times.

Material Deposition

Once the micrometer and nanometer size patterns are transferred to resists on the silicon wafer, magnetic materials need to be deposited to fill these features. In this study, two basic methods were used for material deposition. Details of these methods will be discussed in the next sections.

Thermal Evaporation

The technique of thermal evaporations is commonly used to deposit thin films of a wide range of material. A thermal evaporator increases the vapor pressure of the material to be deposited by melting it in a filament boat. A generic thermal evaporation system consists of three basic units; a vacuum system, an evaporation chamber, and a filament boat assembly (Fig. 11).

A high level of vacuum is needed to ensure a high quality film and to allow the vapor to reach the substrate without reacting with or scattering from gas atoms in the chamber. The system used employs a two stage vacuum system with a primary mechanical pump and a high vacuum diffusion pump. First, the system is evacuated to 10^{-4}Torr using the roughing mechanical pump. Then the diffusion pump is employed to pump the evaporation chamber continuously during evaporation. The mechanical pump used for roughing is also used to back the diffusion pump to remove its exhaust. This system is capable of maintaining vacuums around 10^{-7} Torr during evaporation.

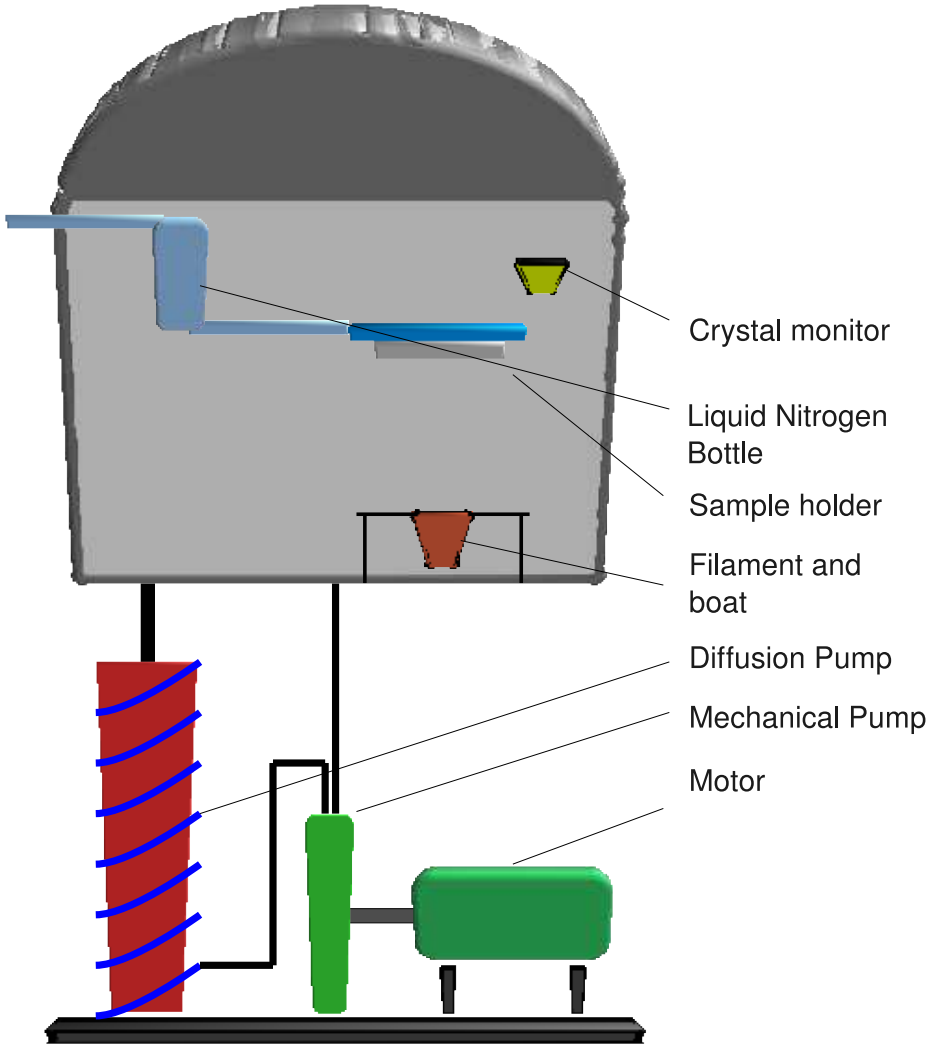

Fig. 11. Thermal evaporation deposition system.

Due to a very large chamber volume, it usually takes the vacuum system about one day to reach that vacuum level.

When the vacuum reaches the desired level, the material to be deposited is melted and evaporated in a dedicated filament boat by passing a high AC current. High energy atoms that are liberated from the melted material reach the target and are deposited on the portions of the substrate that are exposed by the shadow mask. This system has a liquid nitrogen heat sink for cooling the sample to quench the material onto the substrate. The film thickness is monitored by a crystal monitor located in the upper part of the chamber and adjusted by calculating the tooling factor. The tooling factor $F_{Tooling}$ is the square of the ratio of distance of the filament boat to the crystal monitor and that of sample (Eqn. 2.1).

$$F_{Tooling} = [\frac{R_{CrystalMonior}}{R_{Sample}}]^2 \tag{2.1}$$

The thermal evaporation system we used has the capability to do flash evaporation. Flash evaporation is performed using an homemade apparatus designed to drop small pieces of source material into the very hot filament boat. We also can mount two separate filament boats connected to two different current sources, allowing us to evaporate two different materials in situ without having to break the vacuum.

Electron Beam Deposition

A beam of electrons is typically generated by either thermionic or field emission e-beam guns under good vacuum. The generated electron beam is accelerated to a high kinetic energy and focused towards the target material. Although some of the kinetic energy of electrons is lost to X-ray excitations the rest of the energy heats up the target sample and evaporates a portion of it. Evaporated material then deposits onto the substrate, which can be cooled by liquid nitrogen if desired, allowing quench

condensation. In this study, we have used this technique to deposit an insulating oxide layer such as SiO_2.

Electrodeposition

Electrodeposition is the basic process of reducing the cations in a solution to a conducting substrate by passing a direct current through the solution (Fig. 12). Cations that are deposited in the cathode originate either from the consumable anode metal or from the dissolved salts of a desired material in the electrolyte solution that both electrodes are immersed in. In the latter method, the concentration of the desired ions needs to be continuously replenished. The electrolyte solution contains one or more dissolved metal salts. This also makes the solution conductive to facilitate the voltage source to supply the current. The PH level of the solution is measured frequently to monitor the depleting ions. The simple process of electroplating was first invented by Italian chemist Luigi V. Brugnatelli in 1805, and the process has changed very little since.

In order to achieve the same thickness electroplated with each sample of different feature shape and sizes, the user calculates the current density for the particular system at hand and keeps it constant. By keeping the current density constant and by timing the deposition, the user controls the deposition rate, and can accurately determine the plating thickness. In our studies we have used electroplating to fill small pores that we have fabricated, therefore it was very important to stop the plating at the exact time that the material reaches the surface. This cannot be achieved by calculating or by observing the surface. Instead I monitored the current that is passing through the solution in response to the constant bias voltage. When the fabricated pores were being filled the surface area that was exposed was practically constant, the current response changes very little. However, there is a sharp increase

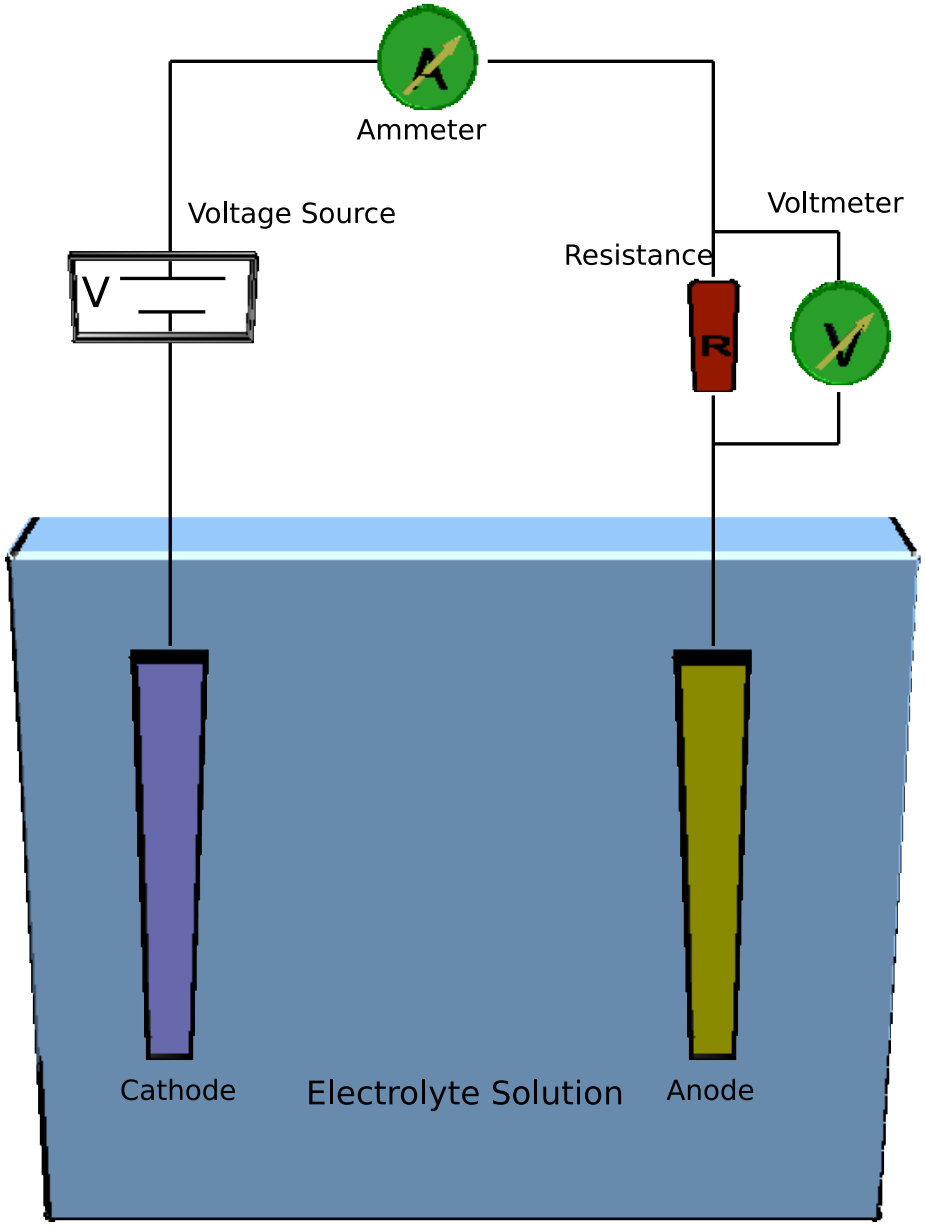

Fig. 12. Electro-deposition cell.

in the current response observed, due to increased surface area when the pores are filled and the material is being deposited outside the pores.

In this study, the electrolyte for Co plating was prepared with 1M $CoCl_2$ and $30g/L$ H_3BO_3 with pH of about 1. The applied voltage varied between 0.5V and 3V depending on exposed sample surface and geometry.

In contrast to two electrodes in an electrolyte solution, there is another method that does not require electrodes or a power source. In the electroless plating method the sample to be plated is placed in the solution with a reducing agent, typically formaldehyde, and the desired metal is plated to the sample surface by a redox reaction similar to Eqn. 2.2.

$$H_2CO + 2[Ag(NH_3)_2]OH \longrightarrow 2Ag_{(s)} + HCOONH_4 + H_2O + 3NH_3 \qquad (2.2)$$

Since a constant and uniform metal ion concentration is in contact with the sample surface at all times, the metal deposits very evenly on the surface.

CHAPTER III

EXPERIMENTAL TECHNIQUES

Cryogenic Techniques and Low Temperature Measurements

In this study low temperature experiments were conducted with a Quantum Design model 6000 physical property measurement system (PPMS) as well as a home made cryostat system.

Quantum Design PPMS

This PPMS operates in a 1.8K to 400K temperature range and a magnetic field up to 9T can be applied with its superconducting solenoid. The capability for warming the sample chamber without having to warm the magnet space permits testing of numerous different samples and running multiple experiments with one transfer of liquid helium. This saves valuable instrument time as well as cooling resources.

The low temperature Nanomagnetics scanning probe microscopy (SPM) system is also designed to fit in the PPMS cryostat. This provides the capabilities for measurements of both transport properties and use of imaging techniques such as scanning tunneling microscopy (STM), atomic force microscopy (AFM) and scanning Hall probe microscopy (SHPM) on the same sample, under the same conditions of field and temperature.

In order to minimize cryogenics boil-off, the liquid He environment is enclosed in a vacuum jacket with several layers of radiation shields. The 9T SC magnet is immersed in the liquid He bath to maintain it at 4.2K. The liquid He is also transfered to the cooling annulus through a series of capillaries in a controlled fashion to cool the sample space. The electronic control unit monitors the sample temperature with a

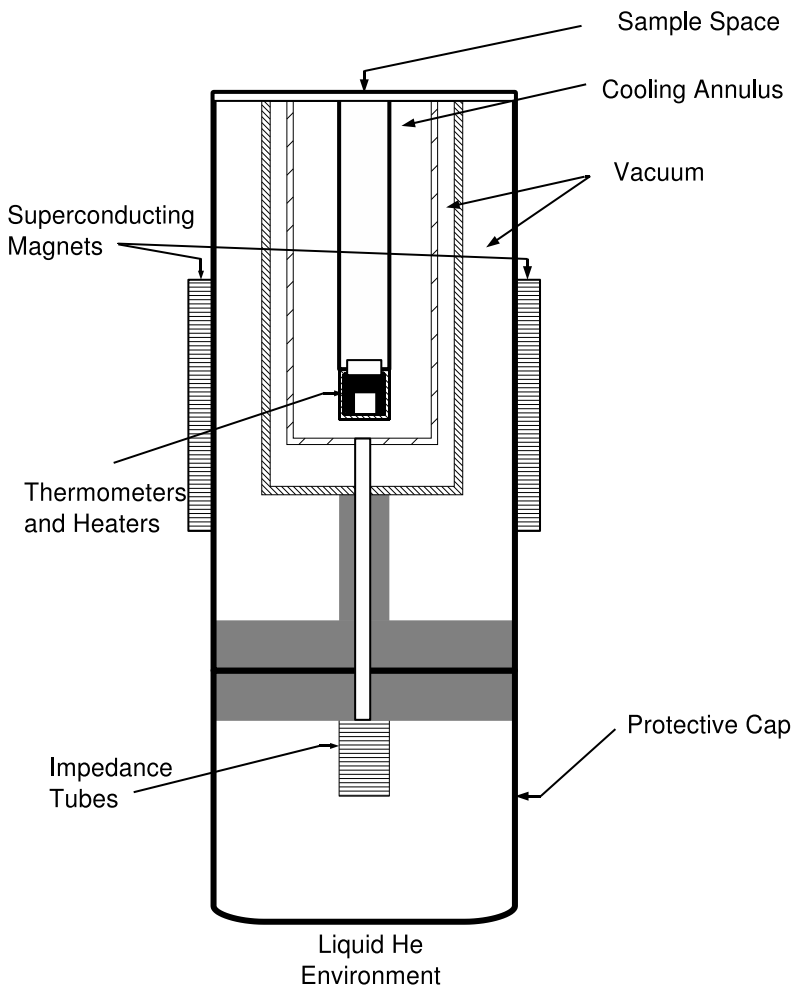

Fig. 13. Inner core structure of a Quantum Design PPMS cryostat (not to scale).

series of thermometers attached to the sample space, and heats and cools the sample space until the sample temperature stabilizes (Fig. 13).

Imaging Techniques

Direct imaging of magnetic and topographical properties of materials can be accomplished by several techniques. They include Bitter-decoration [25, 26, 27, 28, 29], magneto-optical Kerr effect (MOKE) [30, 31], scanning tunneling microscopy (STM)

[32, 33, 34, 35], atomic force microscopy (AFM) [36, 37, 38, 39, 40], magnetic force microscopy (MFM) [41, 42, 43, 44] and scanning Hall probe microscopy (SHPM) [46, 47, 48, 49, 50, 51, 52, 53, 54, 55, 56, 57, 58]. Each method presents a different set of advantages and disadvantages. In this study SHPM, STM, AFM, and MFM techniques were used extensively.

Bitter-Decoration Technique

The Bitter-Decoration method of imaging magnetic structures was developed in the 1930's [25]. In this method, fine magnetic particles are dispersed on the magnetic structure by various techniques, including evaporation or use of a liquid suspension. The magnetic particles deposit on the surface where the magnetic field diverges. The surface is then imaged with an optical microscope [25] or scanning electron microscope (SEM). More recently newer techniques have been developed utilizing STM, the magneto-optical Kerr effect and MFM techniques to observe and image the deposited magnetic particles [26, 27]. In the latter methods the resolution of the image depends practically on the magnetic particle size. In recent years this technique has been extensively used to image the superconducting vortex lattice in magnetic superconductors such as RNi_2B_2C (R=rare earth) [28, 29].

Magneto-Optical Kerr Effect

Magneto-optical Kerr effect (MOKE) is a non-invasive technique that utilizes the interaction between the magnetic field at the sample surface and the electro-magnetic field. An incident polarization-modulated electro-magnetic wave interacts with the surface magnetization and changes its polarization. The polarization change reveals the nature of the sample surface magnetization and the magnetic domain structure [30, 31].

Scanning Tunneling Microscopy

Scanning Tunneling Microscopy is based on the quantum mechanical principle of electron tunneling through a finite potential barrier. A biased sharp conducting tip scans the surface as an electronic feedback loop keeps the tunneling current constant by moving the tip up and down (Fig. 14). The tunneling current is a very sharp (exponential) function of the sample and tip separation. Typically for every 1Å decrease in sample separation the tunneling current increases an order of magnitude. The precise movement of the tunneling tip is achieved using piezoelectric crystal actuators. The resolution of the image depends on the sharpness of the tunneling tip. If an atomically sharp tip is used, it is possible to obtain atomic resolution [33].

In addition to acquiring detailed very high resolution topological images of the surface, STM can be used to perform spectroscopic studies, often referred to as Scanning Tunneling Spectroscopy (STS). By varying the bias voltage between tip and sample, it is possible to acquire $I(V)$ spectra along with the differential conductance $dI/dV(V)$ data. Analisis of the differential conductance provides information about the local electronic density of states. For a superconducting sample, one can identify and characterize the energy gap around the Fermi level (E_F). As discussed earlier, the vortex core region is not superconducting i.e. it exhibits no gap or a reduced gap. In addition to localized measurement of energy gap and $I(V)$ measurements, it is possible to create two-dimensional images by performing spectroscopy at each point of the image scan. This technique is used commonly to image magnetic flux vortices in superconductors and to observe the variation of the density of states in and around the flux lines [34, 35].

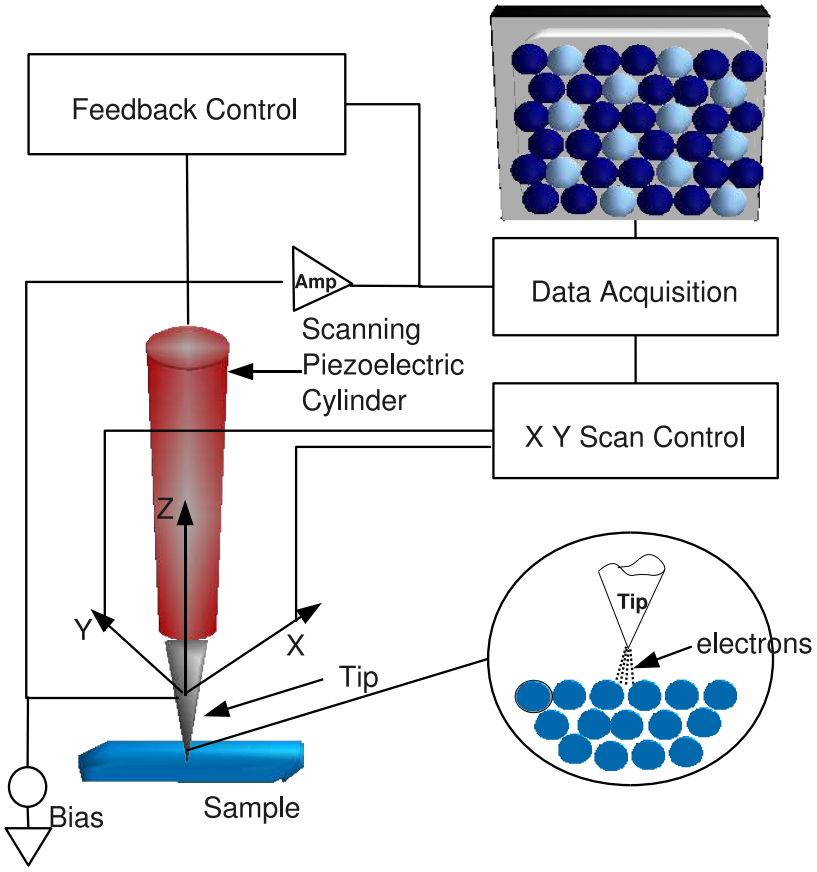

Fig. 14. Basic operation and components of STM.

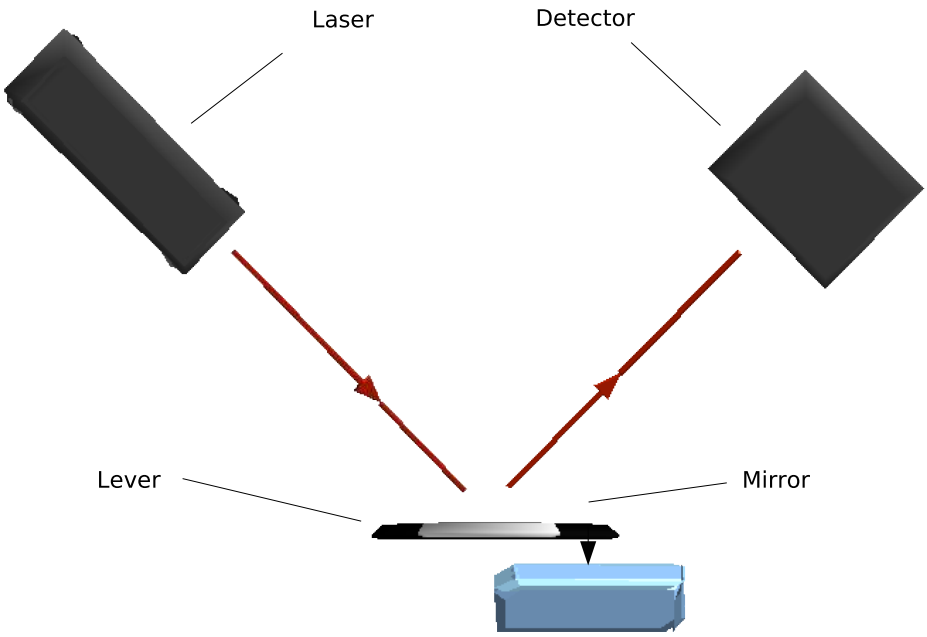

Fig. 15. Basic operation and components of AFM.

Atomic and Magnetic Force Microscopy

In Atomic Force Microscopy (AFM) the small changes in the force between a sharp cantilever tip and the surface are monitored using the shifting resonance frequency of a cantilever [36]. The dominant interactions between the cantilever tip and the surface are the longer range Van der Waals forces and short range chemical forces due to the overlapping electron wave function. There are several methods to measure the cantilever deflection, including capacitive detection [37], piezoresistance [38], interferometery [39] and the most commonly used optical beam deflection method [40] (Fig. 15).

Magnetic Force Microscopy uses the same technique with the exception that the cantilever tip is coated with ferromagnetic material [41, 42, 43]. The image acquired from an AFM with a magnetically coated tip contains information about both the topography and the magnetic properties of the surface. Therefore the microscope

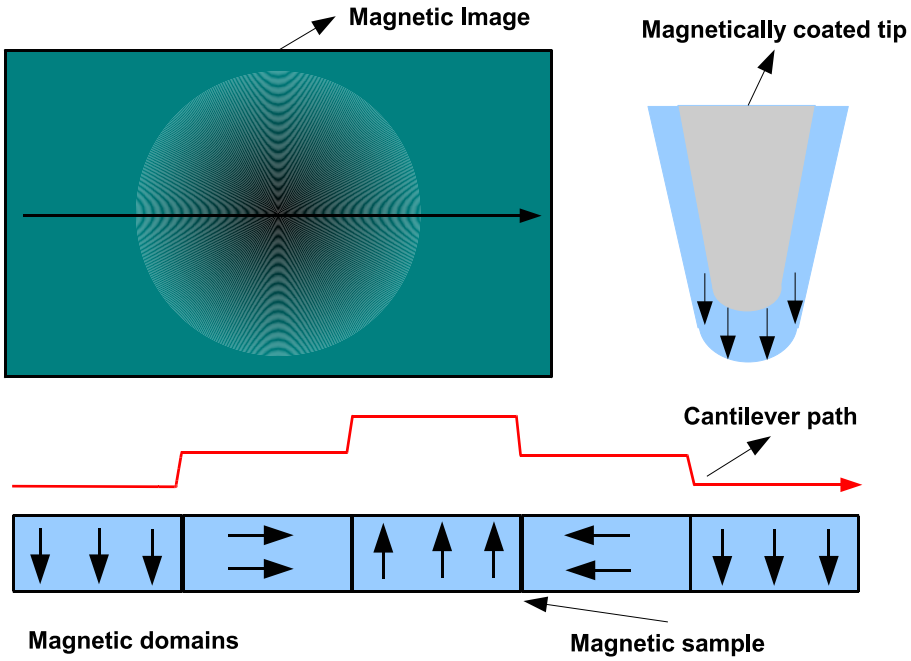

Fig. 16. Basic operation and components of MFM.

can be used as an AFM or a MFM interchangeably. This is achieved by changing the tip to sample separation. Typically, the magnetic forces dominate for greater tip-to-sample separations than the Van der Waals force. Most modern MFM systems require a preliminary topological scan at a close distance followed by a secondary scan at a further distance. The primary topological scan is later used to guide the system on the surface and to offset the topological effects (Fig. 16).

With the current MFM technique a resolution of 20 nm has been achieved [44]. Very recently a 10nm resolution MFM with low temperature imaging capability has become commercially available. Although the high resolution that the MFM technology provides makes it very useful and desirable, the fact that the MFM images map the magnetic force gradient rather than the magnetic force itself complicates their interpretation.

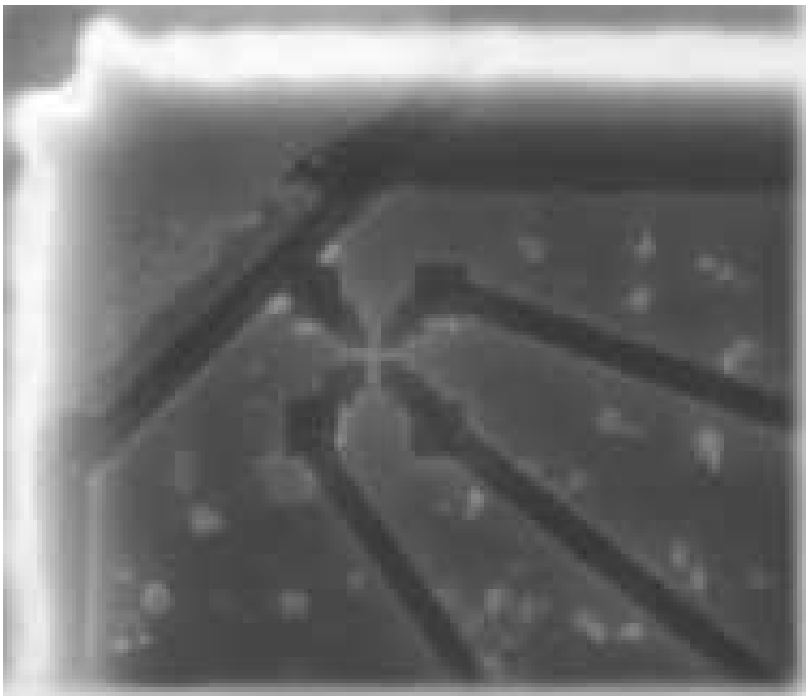

Fig. 17. SEM image of an experimental $50nm$ x $50nm$ size Hall probe [45]. Courtesy of NanoMagnetics Instruments Inc. http://web.nanomagnetics-inst.com.

Scanning Hall Probe Microscopy SHPM

Scanning Hall probe microscopy is a relatively new technique that has originated in the early 1990's [46, 47]. A small Hall probe is fabricated to detect the changes in Hall voltage as the probe is scanned over the sample, thus imaging the localized surface magnetic field distribution (Fig. 17). The typical Hall probe is a 2-D electron gas with very low charge carrier density. Typically $GaAs$, n-doped In-based semiconductors or Bi is used to increase the field sensitivity. A piezoelectric crystal is used to scan the Hall probe sensor over the surface. A STM [55, 56] or an AFM [57] is used to approach the surface and to maintain constant surface probe separation (Fig. 18). SHPM techniques provide a unique set of advantages compared to the other imaging methods presented above.

- This technique measures magnitude of the z-component of the magnetic field.
- Excellent field resolution can be achieved in the presence of a large applied magnetic fields ($7 \times 10^{-6}\, T/\sqrt{Hz}$ at $300\, K$ and $6 \times 10^{-9}\, T/\sqrt{Hz}$ at $4K$).
- Imaging is possible in a wide temperature range ($30\, mK - 340\, K$) [55].
- Relatively short scan time of ($\approx 1\, sec$) makes dynamic magnetic imaging possible [55, 58].
- Spatial resolution as high as ($50\, nm$) can be achieved [48].
- Scan areas as large as ($1\, cm$) can be achieved [49]
- The self magnetic field ($\approx 0.04\, Gauss$) is very small.

The particular SHPM system that was used in this study, was purchased from NanoMagnetics Instruments Ltd. and designed to fit the Quantum Design Ltd. Physical Properties Measurement System (PPMS) for low temperature applications. In this system, the Hall probe is scanned over the sample surface using a STM while the Hall voltage gives the reading of the perpendicular component of the magnetic field produced by the localized surface magnetization. The Hall sensors used are microfabricated near a gold-coated corner of the chip. The gold-coated corner includes the STM tip (Fig. 17). The Hall sensor chip is tilted ($\approx 1^o - 2^o$) with respect to the sample to ensure that the chip corner is the closest part of the chip to the sample surface.

The SHPM can be run in two distinct modes: Lift-off and STM tracking mode. In the lift-off mode, after the surface is found using the STM feedback control, the Hall probe is lifted to and maintained at the desired height above the sample during the scan. The the sample can be scanned very fast ($\approx 2 sec/frame$) in this mode (Fig.

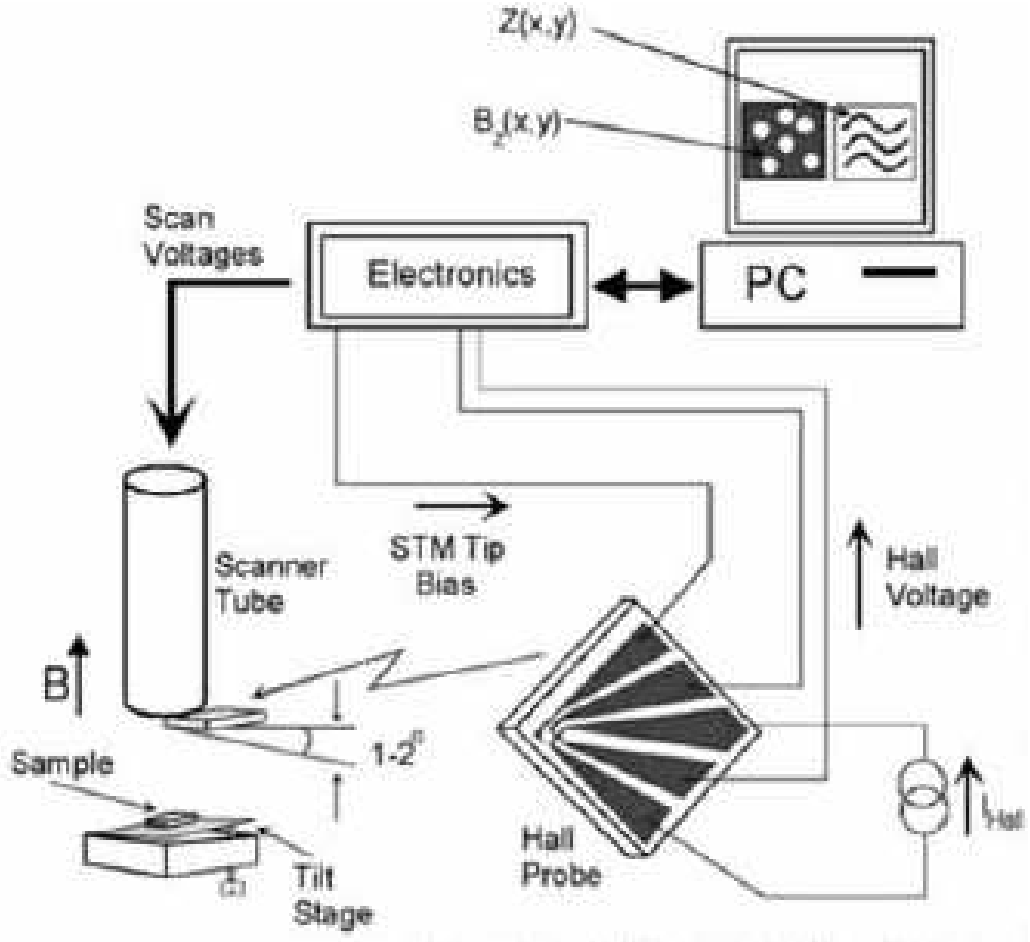

Fig. 18. Basic operation and components of SHPM. Courtesy of NanoMagnetics Instruments Inc. http://web.nanomagnetics-inst.com.

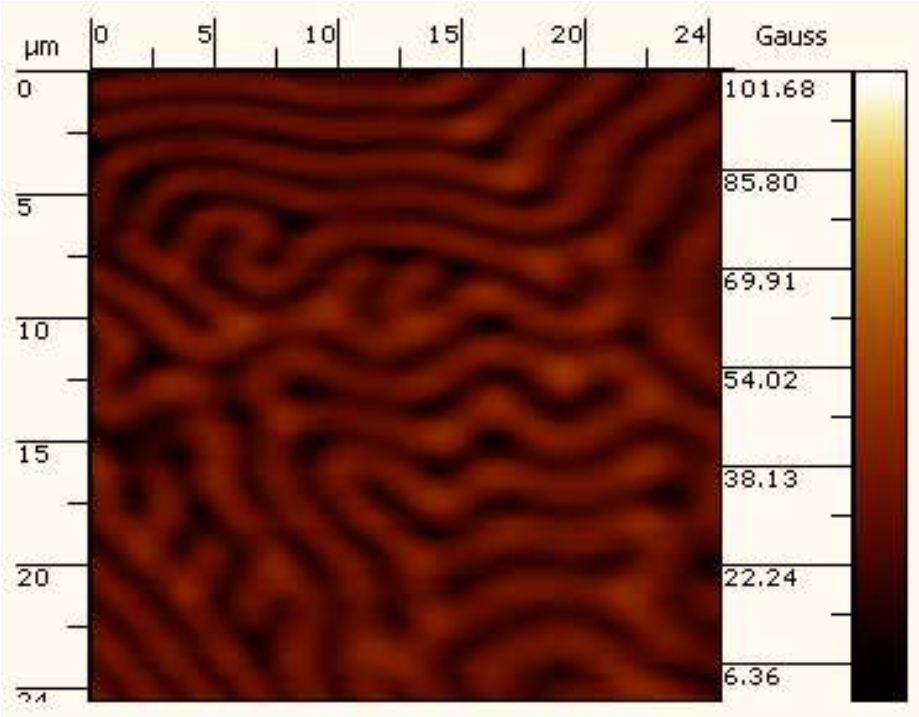

Fig. 19. A SHPM image of an Iron Garnet film in the Lift-off mode.

19). In the STM tracking mode, the tunneling current between the chip corner and the sample surface is measured and used to drive the feedback loop to maintain the constant tunneling current. This allows the experimenter to acquire a simultaneous topography image along with the magnetic field distribution. Also, the constant tunneling current assures the smallest separation between the sample and the Hall probe (Fig. 20, 21). Although this mode provides the lowest noise and highest quality images, it has the drawback of being rather slow ($\approx 5-10\,min/frame$). The detailed imaging procedure and sample preparation is discussed in Appendix A.

Transport Measurements

In this study we have used AC and DC four-probe techniques to perform transport measurements. AC transport measurements were used to acquire I-V curves and

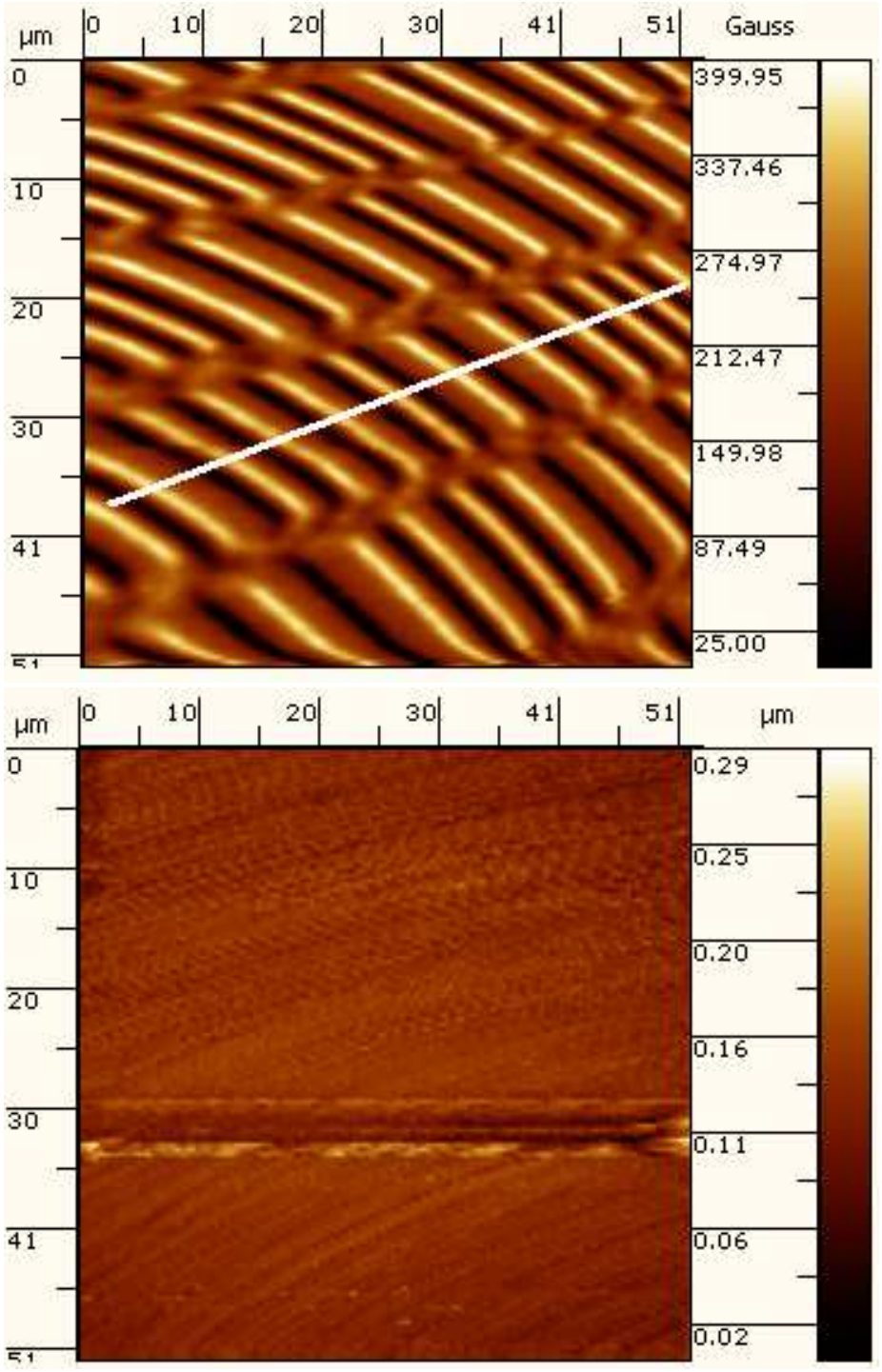

Fig. 20. (a) SHPM image of a computer harddrive in the STM tracking mode. (b) Simultaneous topography image of a computer harddrive, in the STM tracking mode.

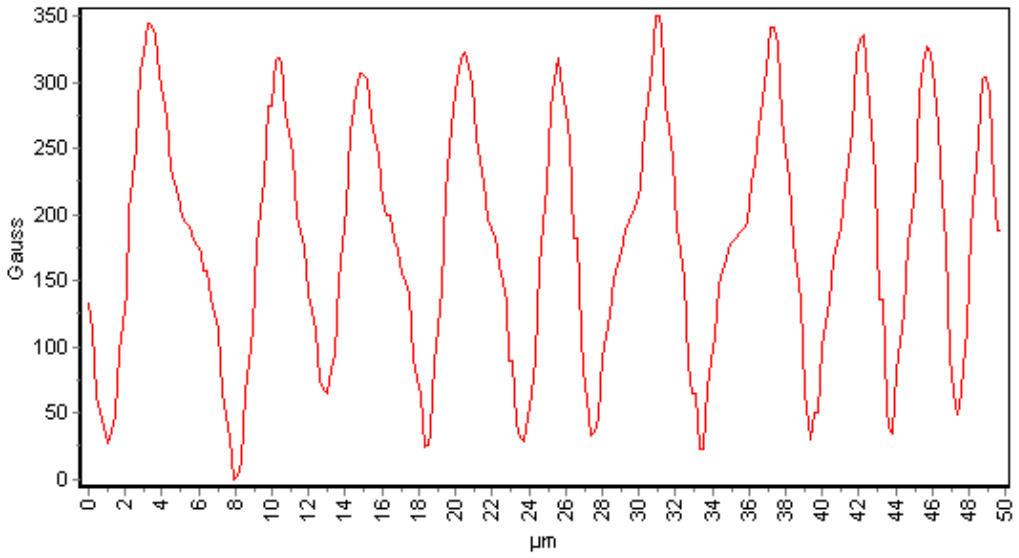

Fig. 21. Magnetic field profile of the marked line in Fig. 20(a).

critical current under varying conditions. DC transport measurements were used for resistivity and second critical field measurements. In these experiments the temperature dependence of resistivity, critical current and critical field of a lead-bismuth thin film under different conditions were studied.

Resistivity Measurement

Electrical resistivity ρ is the quantitative measure of how a medium opposes the flow of electrons that are under the influence of electric field ($\vec{E}$) and defined by Eq. 3.1, and measured in $\Omega \cdot m$ where (R) is the resistance of the medium and (J) is the current density (Fig. 23) in Eq. 3.1. Electrical conductivity (σ) is also defined as the reciprocal of resistivity $\sigma = \frac{1}{\rho}$. Resistivity is not directly measurable, but it is instead calculated by measuring R using a four-probe method with a particularly simple geometry, a slab of length (L) and cross section (A), yielding

$$\rho = \frac{E}{J} = \frac{R \cdot A}{L} \tag{3.1}$$

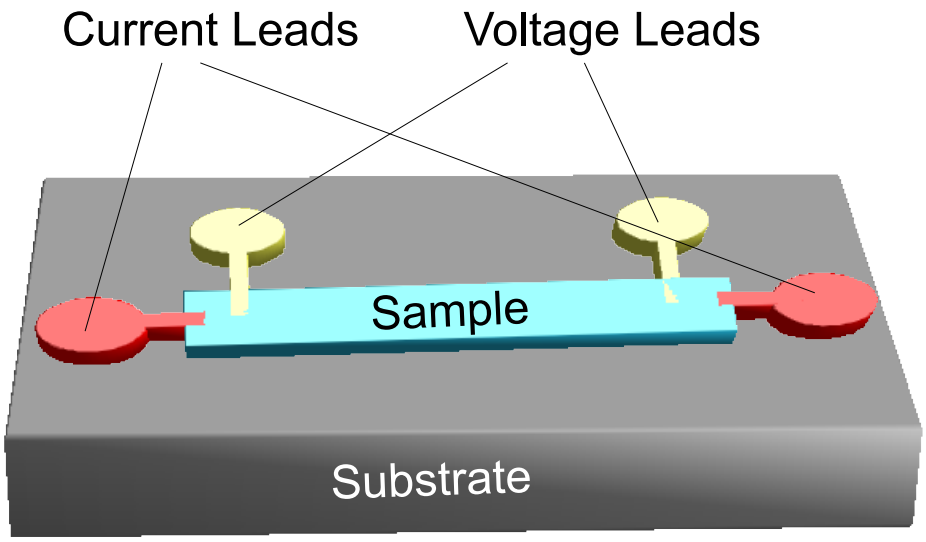

Fig. 22. Four-probe technique.

.

The resistivity of various types of materials behaves differently with changing temperature. Above the Debye temperature the resistivity of a typical metal changes linearly with temperature due to the thermal motion of the ions. This property is often used to calculate the thickness of a thin film of a known metal by measuring the slope of the resistance versus temperature. At lower temperature the temperature dependence is predicted as T^5 due to the electron scattering by phonons or as T^2 due to electron electron scattering. On the other hand, in the case of a typical intrinsic semiconductor, this dependence is exponential $R = R_0 e^{-\alpha/T}$.

The four probe method is based on passing a known current through the material via the two current leads and measuring the voltage drop across the two voltage leads (Fig. 22). Thus, the contact resistances have no effect on the measured voltage since the voltmeter draws negligible current. Effects due to thermal emfs were offset by averaging the values of the voltage acquired for forward and backward current at each temperature. Resistance is then calculated using Ohm's Law (Eq. 3.1) and resistivity

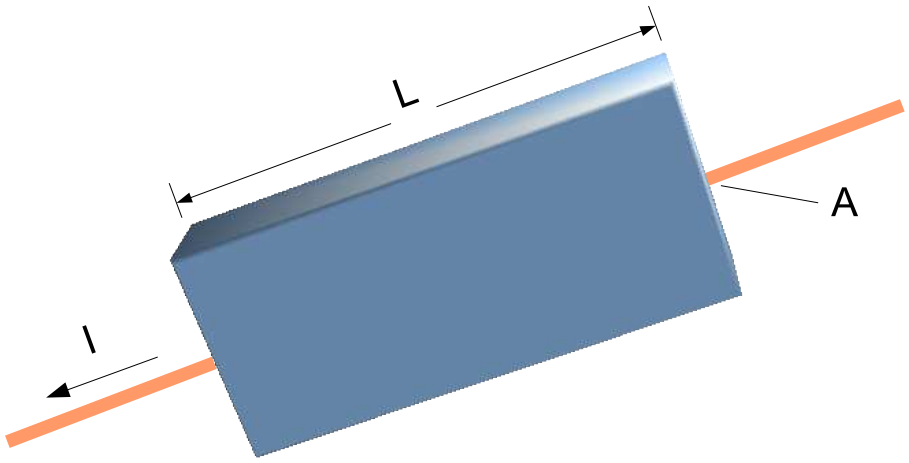

Fig. 23. Slab of length L and cross section A.

$\rho(T)$ is, in turn, calculated using the physical dimensions of the sample. Materials start to deviate from Ohm's Law when the applied current is high. Therefore the resistivity measurements should be performed with small applied currents, to ensure that the material is ohmic.

Superconducting materials exhibit a sharp drop in the resistivity below a certain temperature value. The temperature at which the resistivity starts to deviate from that of the normal state is considered the onset of superconductivity. On the other hand the temperature at which the material becomes fully superconducting is considered to indicate the critical temperature T_C. There are several conventions to define T_C, any of which is acceptable provided that the choice is made considering the specific physical changes that take place in the system:

- Extrapolation to the normal; The transition curve is extrapolated in its steepest part by a tangent line and the intercept with the residual resistance in the normal state is chosen as T_C.

- The onset of superconductivity; Typically this is taken as the temperature at which $\rho(T)$ has dropped 10% from the normal state value.
- The midpoint of the transition; This point is identified as the temperature at which $\rho(T)$ has drpped to 50% of the normal state value.
- Extrapolation to the SC state; The transition curve is extrapolated in its steepest part by a tangent line to the T axis intercept (i.e. $\rho = 0$).
- Full transition point; Typically this point is the temperature marks at which $\rho(T)$ has dropped by 95% of the normal state value.

Critical Electrical Current Density

Electrical current I is a macroscopic, average quantity defined using the charge passing through an area A, i.e. the surface integral of the electrical current density $\vec{J}$ over the area (Eq. 3.2). In turn the current density $\vec{J}$ can be defined by Eq. 3.3, where n is the charge carrier density, q is the unit charge, $\vec{v_d}$ is the drift velocity and ρ_c the charge density. Thus,

$$I = \int_S \vec{J} \cdot \, d\vec{A} \tag{3.2}$$

$$\vec{J} = n\, q\, \vec{v_d} = \rho_c\, \vec{v_d} \tag{3.3}$$

. Using the divergence theorem and the fact that charge is conserved, we get (Eq. 3.4). Therefore, current density is a conserved quantity in the DC measurement, and (Eq. 3.5) is called the continuity equation.

$$\int_S \vec{J} \cdot \, d\vec{A} = \int_V (\vec{\nabla} \cdot \vec{J})\, dV = -\frac{d}{dt} \int_V \rho_c \, dV \tag{3.4}$$

$$\vec{\nabla} \cdot \vec{J} = -\frac{\partial}{\partial t}\, \rho_c \tag{3.5}$$

For superconductors there is an intrinsic critical value of current density $\vec{J_C}$ above

which superconductivity is spontaneously suppressed when the kinetic energy of the charge carriers exceeds the condensation energy. SC could also be destroyed by the magnetic field created by the current itself. Critical current is typically determined by measuring I-V curves and marking the current value where the voltage reaches a certain pre-determined value. An accepted convention for this critical voltage value is $1 - 2\mu V$ for every cm of sample length. Usually the measured critical currents are far below that from the expected intrinsic or the self-field valued and result from flux flow as described in Chapter I.

Critical Magnetic Field

The critical magnetic field (H_C), is defined as the maximum value of magnetic field that can be applied without destroying superconductivity. This maximum field value naturally is attained at absolute zero, since there is no experimental equipment that can reach 0K, $H_C(T = 0)$ is an extrapolated value. There are in fact two values of critical field for Type-II superconductors each defining the upper and lower boundary of the vortex state (Fig. 1). The first one, H_{C1}, is reached at the onset of the pure superconducting to the mixed (vortex) state transition, and the second and higher one, H_{C2}, is reached when superconductivity is suppressed altogether. This is explained in more detail in Chapter I.

The upper critical field, H_{C2} , is usually reported in literature by H_{C2} vs. Temperature plots, and the maximum value of critical field at 0K $H_{C2}(T = 0)$ is estimated from this plot. Therefore in order to measure H_{C2}, resistivity measurements are taken at a series of fixed magnetic fields and T_C is recorded at each field value.

Magnetization Measurements

Magnetization measurements were performed with the SHPM. Although the SHPM is not as sensitive as a SQUID, it can yield B-H curves at chosen locations on the sample. With SHPM the we can acquire images of the surface magnetic field variation, and later relocate the Hall probe at a chosen location on the sample and acquire B-H curves. Alternatively, a set of SHPM images can be acquired over a range of different conditions, and regions of interest in these images then can be integrated to reveal the localized surface magnetization of the sample. This feature enabled us to further investigate the magnetic properties of the artificial magnetic structures fabricated in this work.

The SQUID directly measures the magnetization M of the material. However, a SHPM records the magnetic flux density B as a function of applied magnetic field H. Since in this study we use the magnetic substructures to create artificial magnetic field variations on the superconductor, the B data is more informative and convenient than M. To obtain M the CGS equation $\vec{B} = \vec{H} + 4\pi\vec{M}$ can be used.

CHAPTER IV

CHARACTERIZATION OF SOME MICRON-SIZE MAGNETIC SYSTEMS WITH SCANNING HALL PROBE

Imaging of small magnetic structures has been of interest for several decades. Images of the local magnetic field distribution provide insights about the the material and open up new possibilities for research. In this study my intention was to use scanning Hall probe microscopy to image the normal component of the surface magnetic field distribution and obtain information about the size, orientation, field and temperature dependence of the magnetic domain structure.

Reasons for choosing SHPM were discussed in the earlier Chapter. There are several groups that have successfully used this technique for several years. The group headed by K. A. Moler in Stanford University has been using a large scan area SHPM as well as Scanning Squid Microscopy [51, 52, 53]. S. J. Bending's contribution in University of Bath has been critical in developing Hall-probe microscopy [46, 54, 55, 56]. A. Oral at Bilkent University has fabricated and made commercially available a room temperature and low temperature version of the SHPM [55, 56, 57, 58]. The system he designed has been used around the world in many research institutions, including Texas A&M University .

Micro-machined Permalloy Needle

In this study, experimental characterization of a new micromachined electromagnetic probe, intended for various biological manipulation and stimulation applications is presented. The micro electromagnetic probe consists of a protruding (out-of-chip), sharp permalloy needle embedded into a three-dimensional gold conducting coil. The probe fabrication is carried out using traditional surface micromachining processes

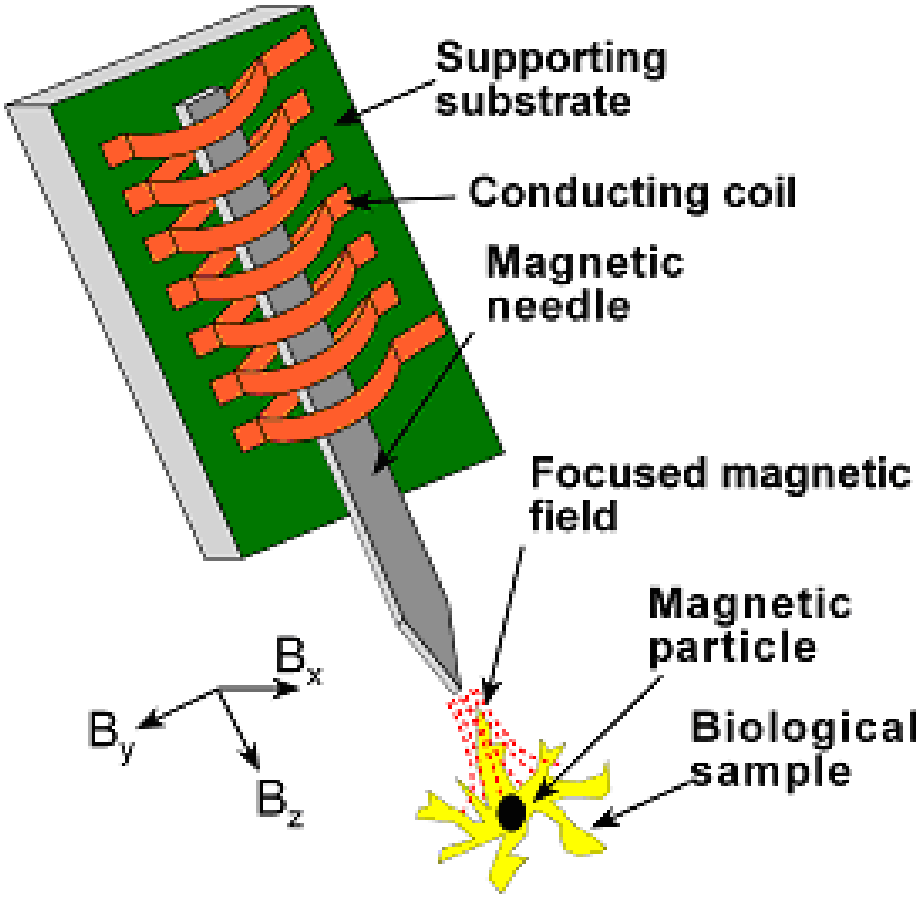

Fig. 24. Protruding (permalloy) magnetic core with a sharp tip.

coupled with assembly techniques [59, 60] by M. Yapici and J. Zou in the Texas A&M University Electrical Engineering department (Figs. 24, 25). Magnetic characterization of the probe performance by SHPM (e.g. peak magnetic intensity and spatial field distribution) was achieved for the first time for such a system. A comparison of electromagnetic simulations to the SHPM characterization of the micro electromagnetic probe [59] is presented. The manipulation of sub-micron sized magnetic particles with the developed probe was also demonstrated [59].

The experimental test setup depicted in Fig. 26 includes the SHPM stage and the probe assembly designed to enable efficient testing. The probe was attached to a

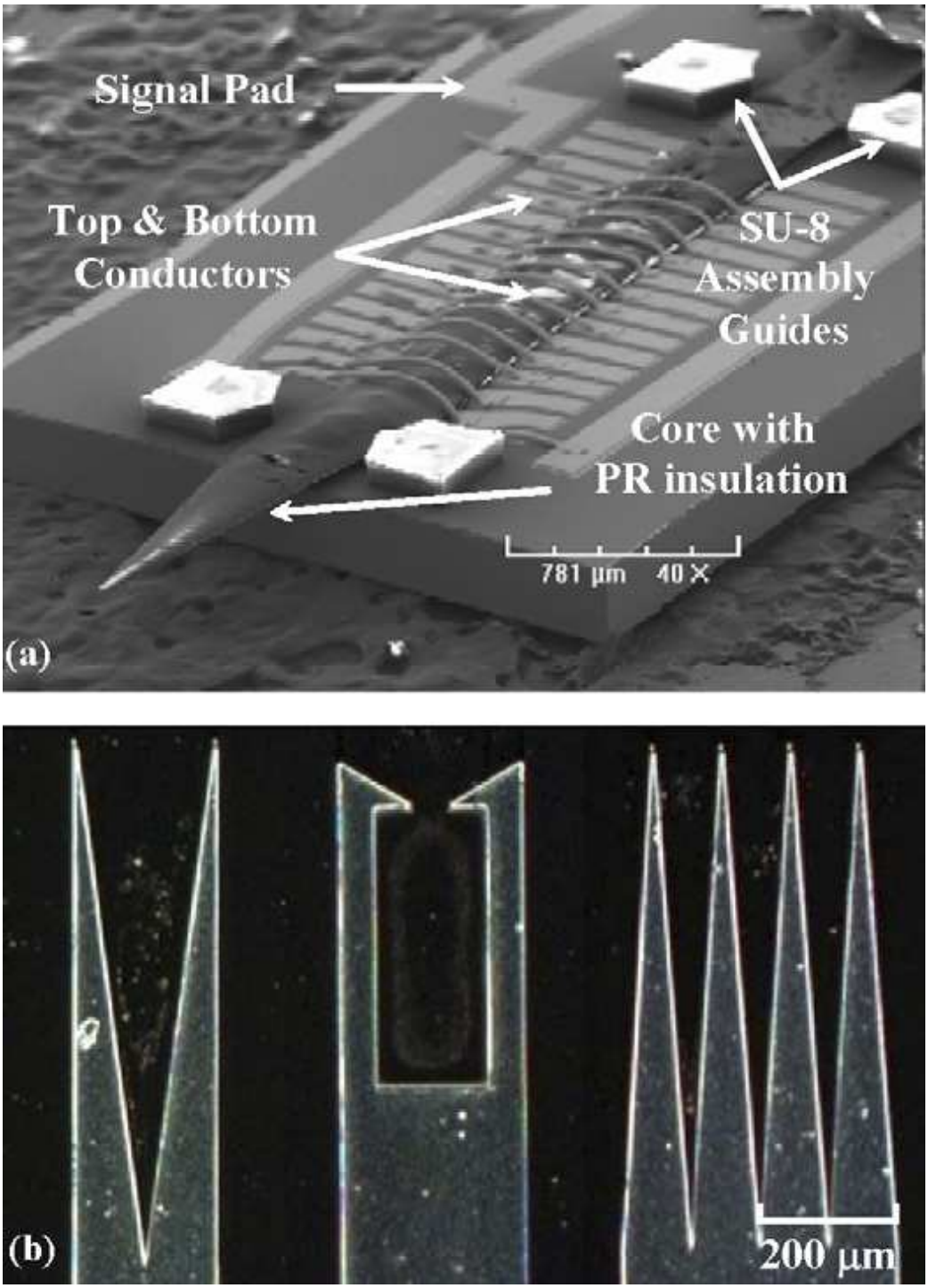

Fig. 25. (a) Scanning electron micrograph of a fabricated micro electromagnetic probe; (b) Optical microscopy pictures of permalloy magnetic cores with different tip profiles.

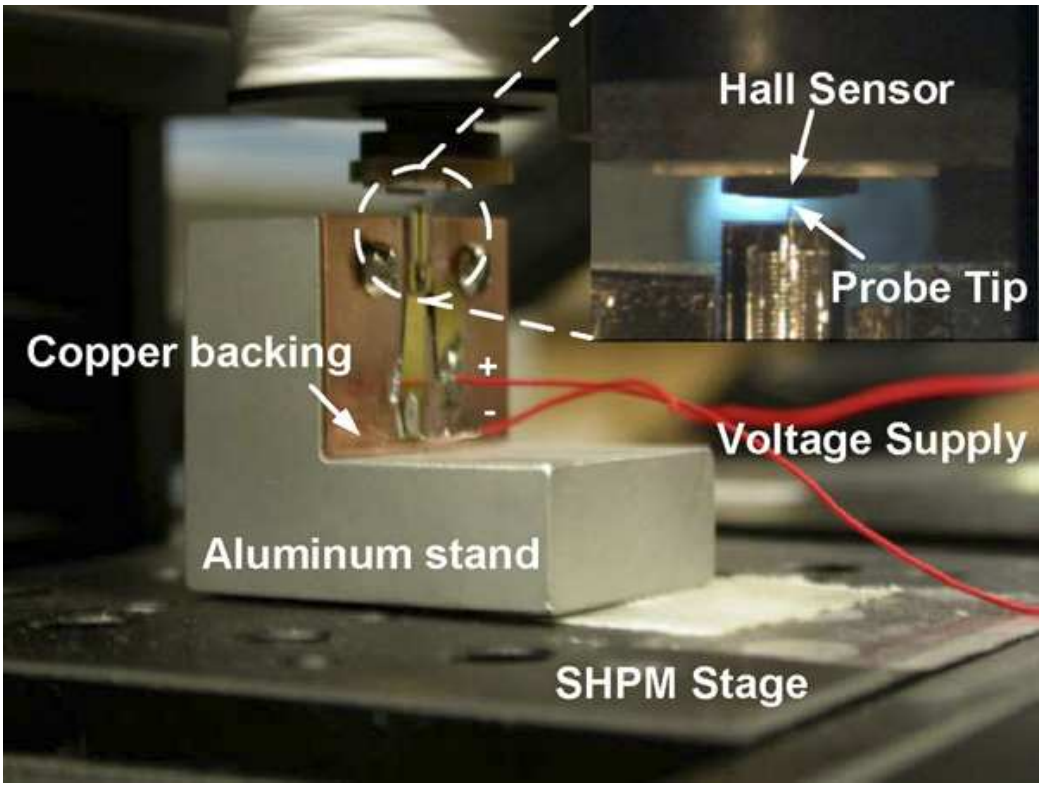

Fig. 26. Scanning Hall probe microscope setup for micro electromagnetic probe characterization. The gap between the probe tip and Hall sensor is estimated to be $\approx 20\mu m$.

larger copper plate, which facilitates both probe handling and allows rapid dissipation of the heat generated during the probe operation. Simulations under different input currents were carried out to characterize the effect of input current on the probe temperature [59]. A plot of the tip temperature under different input currents indicated an increase in tip temperature with higher current levels (Fig. 27). This heat sink mechanism ensures that the permalloy magnetic cores do not show significant displacement during probe operation, allowing proper testing conditions during characterization experiments and actual operation of the probe in biological applications. The copper plate that houses the probe is attached to an aluminum stand which allows the probe tip to be easily positioned and aligned perpendicular to the Hall sensor.

Before the measurement, the probe tip was first demagnetized using the built-in coil of the SHPM by applying an exponentially decaying sinusoidal magnetic field with alternating polarity to the axis of the magnetic core. After the demagnetization, the tip of the probe was aligned to the Hall sensor and the peak output magnetic field density $\vec{B}$ as a function of the input current I was measured. As shown in Fig. 28, the output magnetic field density $\vec{B}$ first increased linearly as a function of the input current I and then saturated near 300Gauss. Next, the B-H curve of the permalloy core was characterized, which revealed a characteristic hysteresis behavior (Fig. 29). It should be noted that the measured saturation intensity of 300Gauss is much lower than the saturation magnetization of permalloy ($\approx 0.9T$) widely reported in literature [61].

This is because the Hall sensor was positioned approximately 20μm away from the probe tip. Due to the large field gradient, the magnetic field of the probe quickly diminishes at locations farther away from the probe tip. In many biological applications, the samples usually have to be placed at a small distance away from the probe

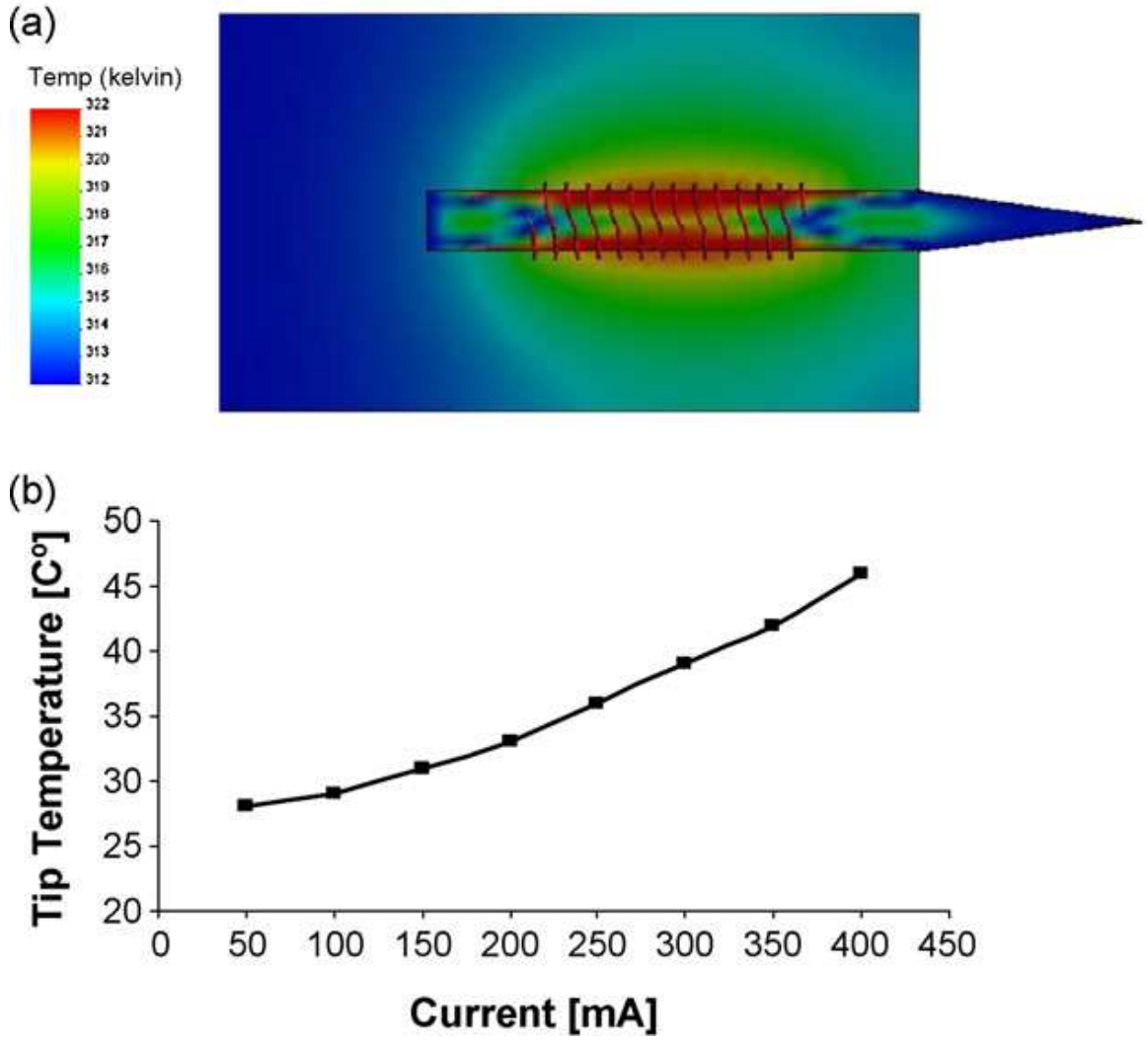

Fig. 27. (a) Finite element simulation showing the temperature distribution of the micro electromagnetic probe under 300 mA input current; (b) plot of the probe tip temperature under different input current levels.

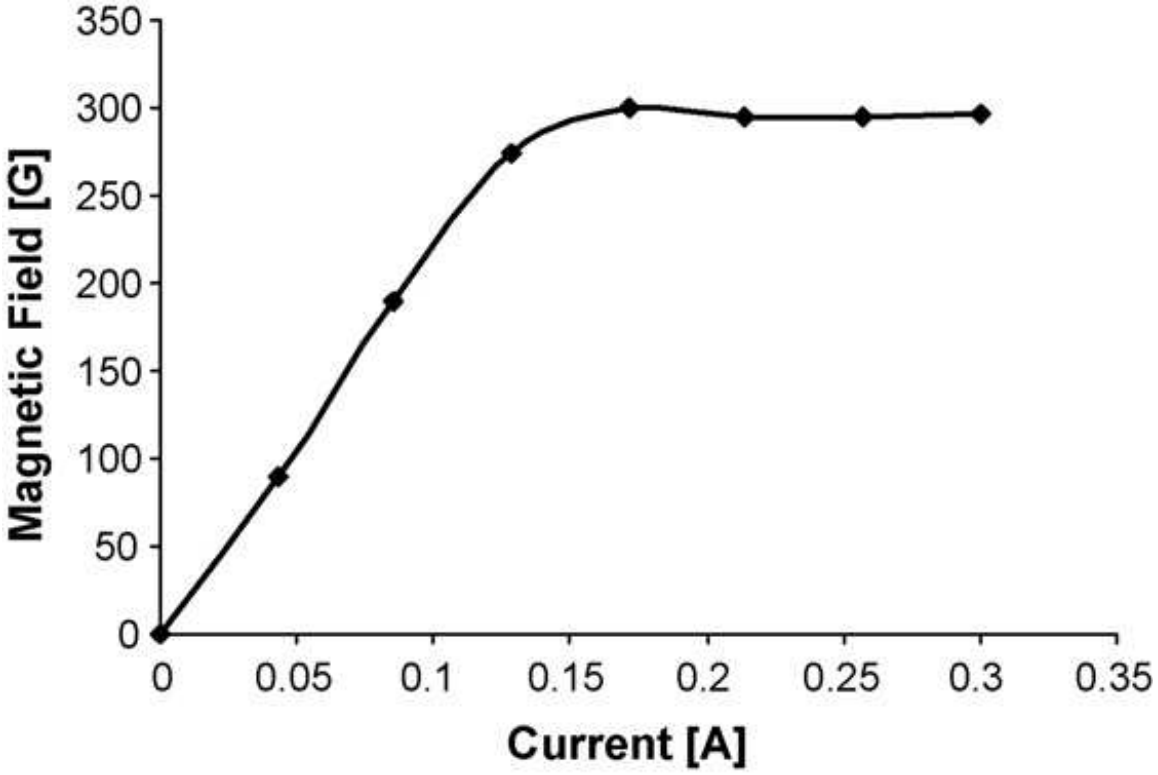

Fig. 28. Measured magnetic field output $20\mu m$ from the tip of the micro electromagnetic probe as a function of input current.

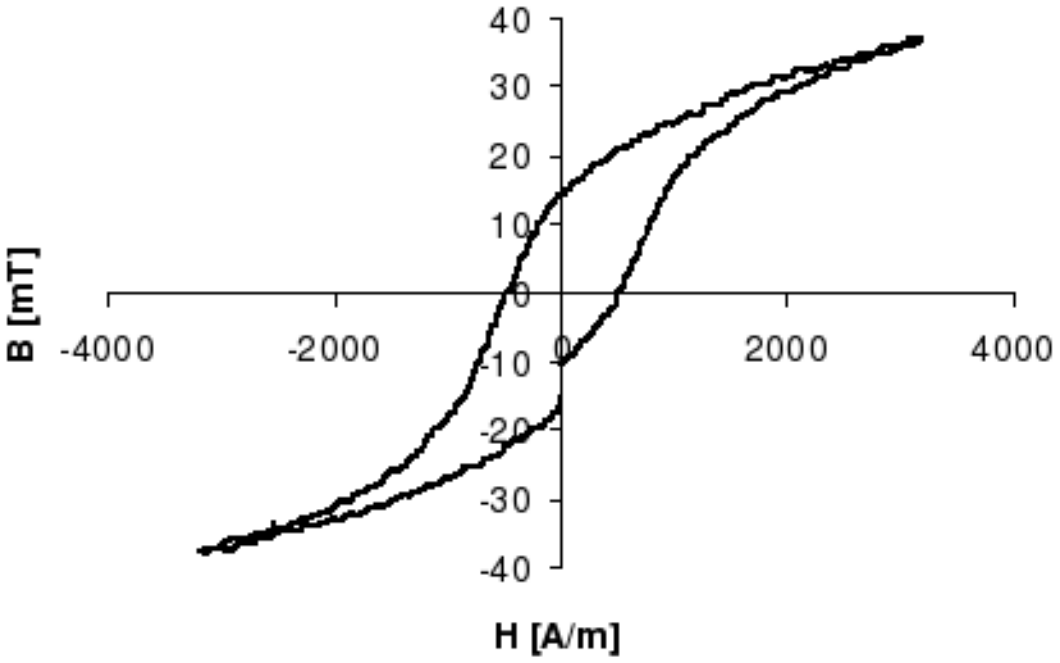

Fig. 29. The B-H curve of the permalloy magnetic core characterized by the scanning Hall probe microscope located about $20\mu m$ from the tip of the core.

tip. Therefore, the measurement setup and results are valid and useful in assessing the actual magnetic field that will be experienced by the biological samples since they reflect the real working condition of the probes.

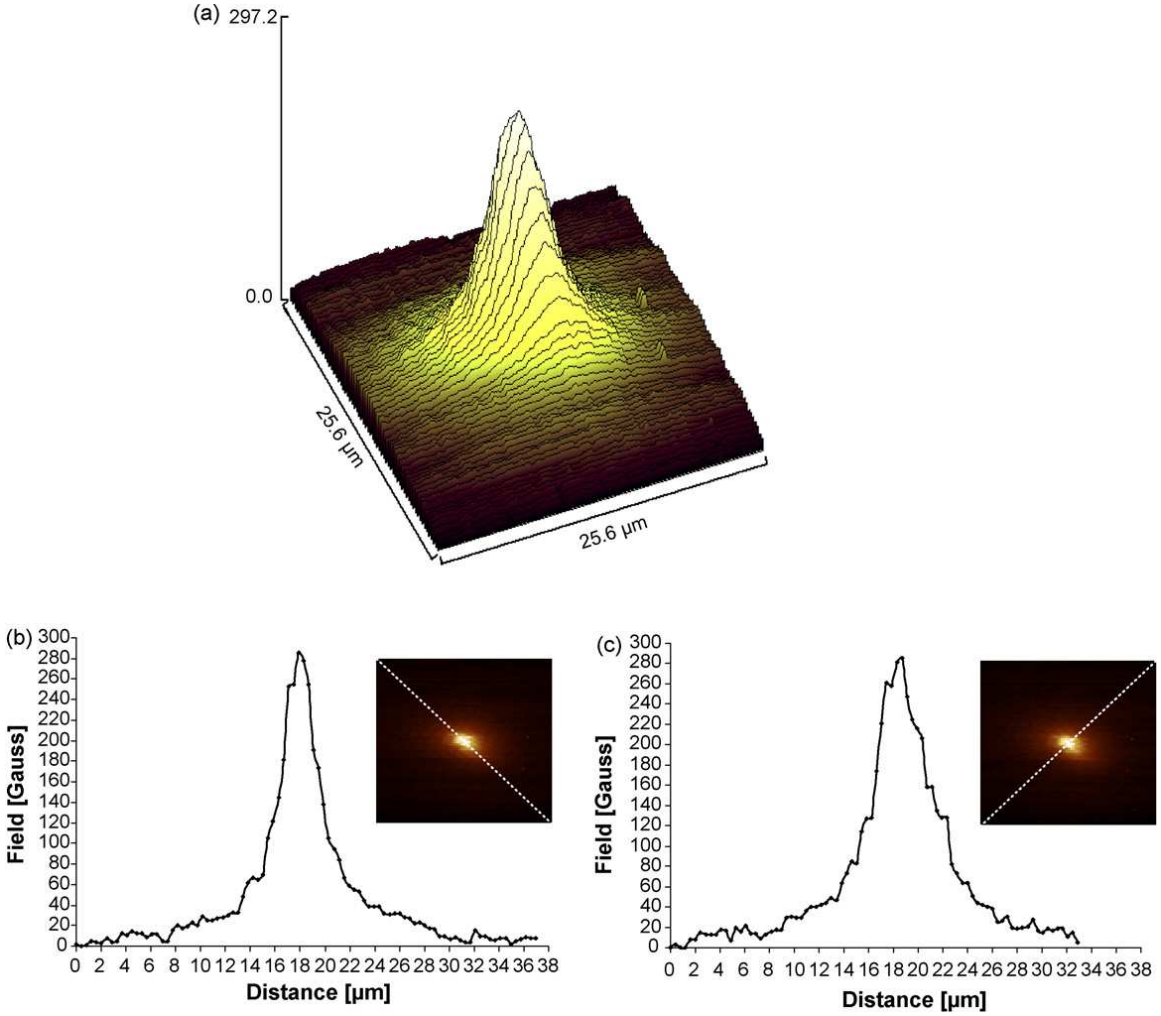

Fig. 30. Measured spatial distribution of the magnetic field output (the component parallel to the axis of the probe) with an input current of 300 mA: (a) surface plot; (b) and (c) axial field plots along the diagonals of the probe tip obtained from the cross-sectional field distribution.

In order to obtain the spatial distribution of the magnetic field, the Hall sensor probe is scanned across an area of $25\mu m \times 25\mu m$ around the probe tip, while maintaining the gap between the probe tip and the Hall sensor. Fig. 30 shows both

the axial and the 3D surface plot of the magnetic field distribution when an input current of 300 mA is applied. The field drops rapidly to half of its peak value (297 Gauss) within a distance of $4\mu m$ and to a few Gauss within a distance of about $12\mu m$ which is consistent with the simulation study reported in [59]. This translates into a large field gradient ($\partial B_z/\partial x$) of $\approx 2500T/m$ suitable for biological applications which require site-specific field delivery [62, 63, 64, 65]. Likewise, by measuring the magnetic field at two different Hall sensor to probe tip separations, the gradient term ($\partial B_z/\partial z$) important for force generation ($F = m_z \frac{\partial B_z}{\partial z} = V\chi_m H_z \frac{\partial B_z}{\partial z}$) was again found to be $\approx 2500T/m$. It was found that the spatial distribution of the magnetic field is extremely sensitive to the actual profile of the probe tip, which inevitably is different from the design due to imperfections in probe fabrication. This indicates that in applications where an accurate mapping of the field distribution is critical, a good experimental characterization is indispensable.

By using an SHPM with high spatial resolution and field sensitivity, a comprehensive experimental characterization of the fabricated probes was successfully conducted. The experimental measurement technique presented therein allowed real-time measurement of magnetic phenomena at the micro scale and provided a venue to evaluate the probe performance for optimized design and application. Results indicate that further improvement on the probe performance can be achieved through optimizations in the core geometry. For example, fabricating magnetic cores with sharper tips will increase the flux concentration (i.e. magnetic flux density or induction) thereby allowing a higher localization of the field. This can be achieved by using high-resolution pattern generation (e.g. electron beam lithography) or by further sharpening the tips, e.g. with focused ion beam (FIB) etching techniques.

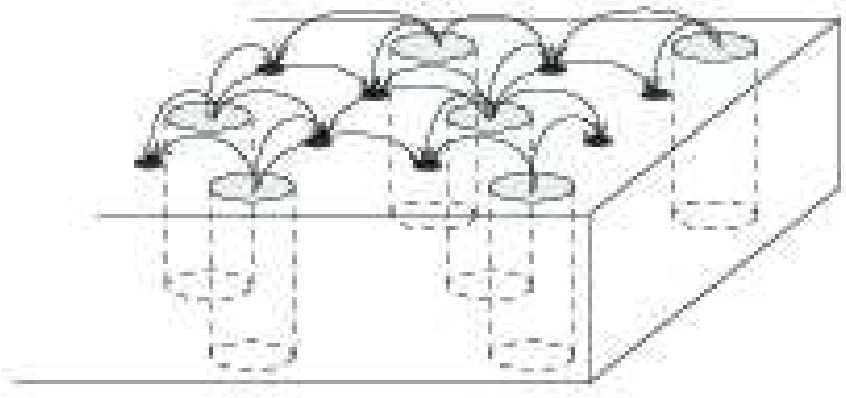

Fig. 31. Schematic magnetic field pattern on the surface of the MNR array. Lines show magnetic field lines. MNR are magnetized parallel to their axis as shown with large arrow.

Strong Spatially Alternating Magnetic Field from Magnetic Nanostructures

In this study magnetic characterization of magnetic columnar nanostructures, magnetic (Ni, Co) columns with small diameter (50nm) and a high aspect ratio (5-7), was performed. Arrays of Ni and Co nanorods 350 nm high and about 50nm diameter were grown electrochemically in PMMA templates prepared using electron beam nanolithography by K. Kim at the Texas A&M University, Physics Department. Imaging with Atomic Force Microscopy (AFM) and Magnetic Force Microscopy (MFM) was done by H. Lee at the same institution. Magnetic properties of such arrays were studied also with scanning Hall probe microscopy (SHPM). It was found that each nanorod remains a single domain (magnetized) in zero field at room temperature. The array of nanorods creates a spatially alternating magnetic field on the order of a Tesla at its surface which can be used in several applications.

Arrays of Magnetic Nanorods (MNR) enable studies of a new class of phenomena based on the interaction between spatially separated, but closely located ferromagnets

and superconductors [17, 18]. This approach offers vast opportunities for both science and technology and may ultimately enable improved superconducting materials. A comprehensive study of pinning properties of these arrays is described in Chapter V.

Effective use of these arrays as SC-FM hybrids requires: (i) high aspect ratio (length to diameter); (ii) small (< 100 nm) diameter; (iii) the possibility to fabricate arrays while independently controlling the magnetic rod diameter and the structure period over a wide range of values; (iv) a strong magnetic field in the Tesla range at the end of the nanorod top. Fig. 31 shows the magnetic field distribution on the surface of the MNR array schematically. In the overwhelming majority of magnetic micro/nano structures studied previously as a part of magnet-superconductor hybrids (see reviews [17, 18]), the magnetization is in-plane; consequently, the component of the magnetic field normal to the film is rather weak. Even when the magnetization is normal to the plane, as for CoPt films, the component of magnetization normal to the film is weak, due to the small aspect ratio of the magnetic elements which produces a large demagnetization field [17, 18]. Arrays of magnetic nanorods/nanopillars have been fabricated by different methods for patterned recording media, as described in the review by C. A. Ross [66]. The methods used by the Ross group [67, 68, 69] are probably closest to fulfilling requirements (i)-(iv) among those described in [66]: the aspect ratio was as large as 3 [68], and the ratio of diameter to period was 0.4-0.9 [68]. Another way to create very high aspect ratio arrays of nanorod/nanowires is to use an alumina template. This approach is described in detail in review [70]. However, with the alumina template techniques the ratio of the period to magnetic nanorod diameter is limited to an even narrower range than in [68]. The goal of this section is to evaluate e-beam nanolithography techniques for fabrication of magnetic nanostructures which fulfill the requirements (i)-(iv). It is demonstrated here that it is possible to fabricate magnetic (Ni, Co) columns with a high aspect ratio (5-7) and

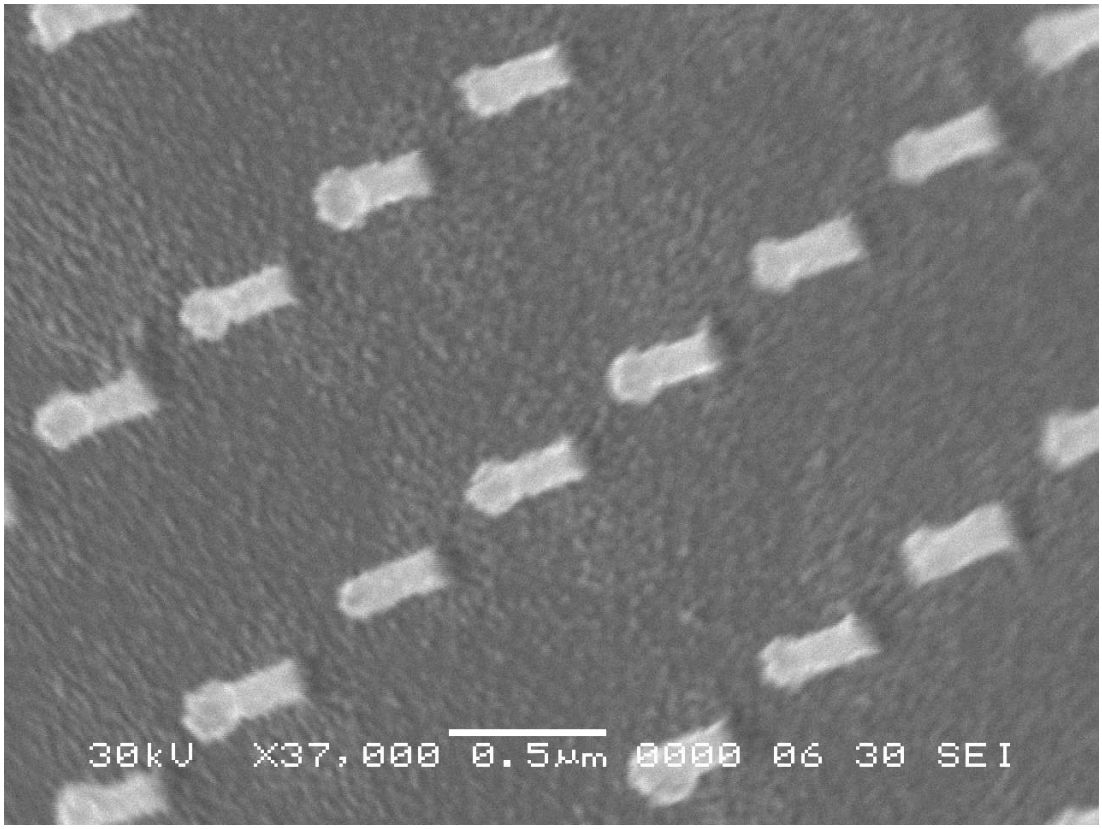

Fig. 32. SEM micrograph of a Ni nanorod array with a $2\mu m$ period, 50nm rod diameter and 350nm height. The chip is tilted by 45^o.

of sufficiently small diameter (50nm) to preserve the magnetization direction (parallel to the column), and with a period to diameter ratio varying in very wide range.

Nanostructures were studied by Atomic Force Microscopy (AFM) and Scanning Electron Microscopy (SEM). Fig. 32 shows an SEM image of a nickel MNR array with the period of $2\mu m$, but arrays with period as small as 250nm were also fabricated. Further increase in the MNR density resulted in lower quality arrays. Magnetic properties of the arrays were studied prior to lift-off of PMMA with magnetic force microscope (MFM) and scanning Hall probe microscopy (SHPM).

Fig. 33 shows a MFM image of Co nanorods in the PMMA matrix, and Fig. 34 shows a scan along the line marked in Fig. 33. The MFM scans of "phase shift"

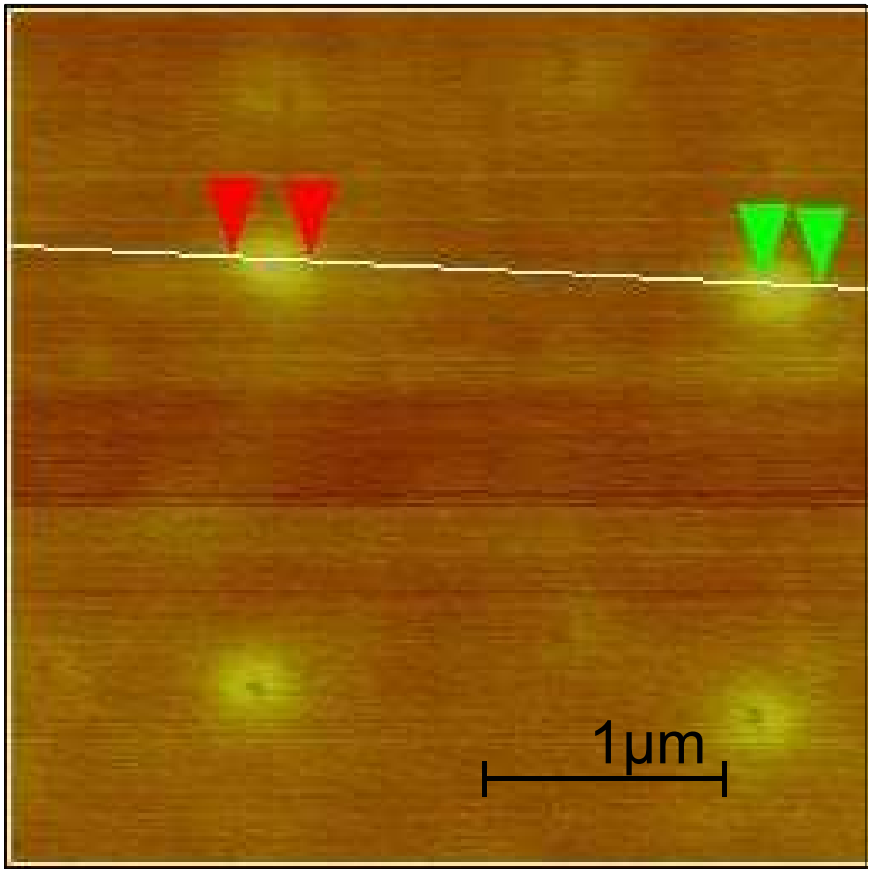

Fig. 33. Magnetic Force Microscope (MFM) image of Co nanorods in a PMMA matrix.

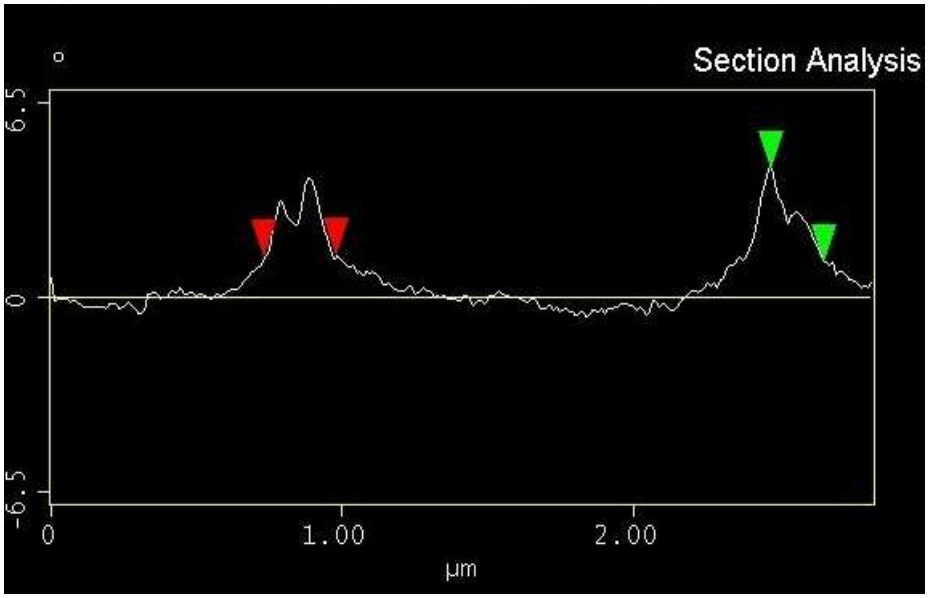

Fig. 34. Magnetic Force Microscope (MFM) scan of the "phase shift" along the line in Fig. 33 crossing two MNR. Different signs correspond to different directions of the vertical field component of the magnetic field.

show different signs corresponding to different directions of the normal component of the magnetic field. The amplitude is much larger above the Co nanorods, as expected. The normal component of the magnetic field between the MNR has a direction opposite to that just above the rods and is much weaker due to the very small ratio of areas of the 50nm diameter MNR and the large ($2\mu m \times 2\mu m$) unit cell of the array. Fig. 35 shows a scanning Hall probe microscope (SHPM) image of the same array. The SHPM scan at 200nm above the surface shows alternating magnetic field distribution with a $2\mu m$ period. Bright and dark spots correspond to opposite magnetic field directions normal to the film. The SHPM resolution is 500nm so that the magnetic field distribution shown in Fig. 35 is "smoothed". The bright and dark regions in Fig. 35 indicate magnetic field due to the nanorods and their return field. Within the bright regions there is no change in magnetic field direction. Therefore it can be concluded that each nanorod is single domain. However, one can estimate the

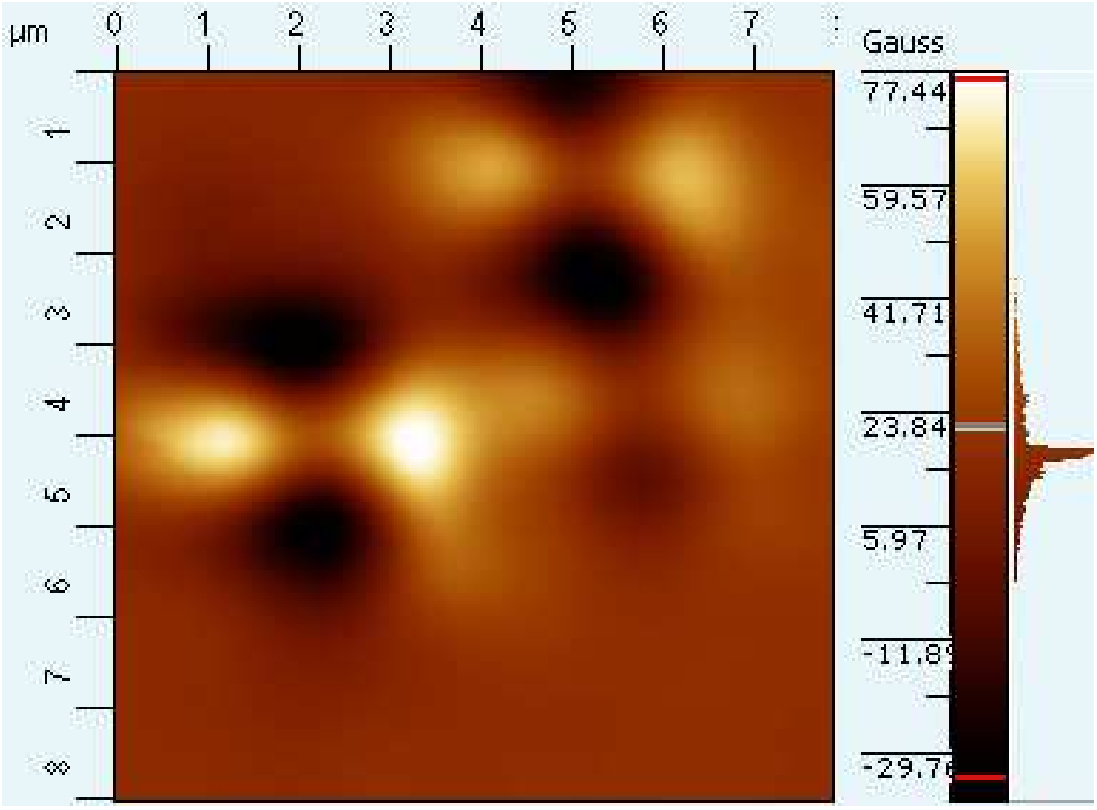

Fig. 35. Scanning Hall probe microscope (SHPM) scan of the alternating magnetic field distribution taken at 200nm above the surface of a magnetic nanostructure with a $2\mu m$ period. Bright and dark spots correspond to opposite directions of the magnetic field above the plane of the nanostructures.

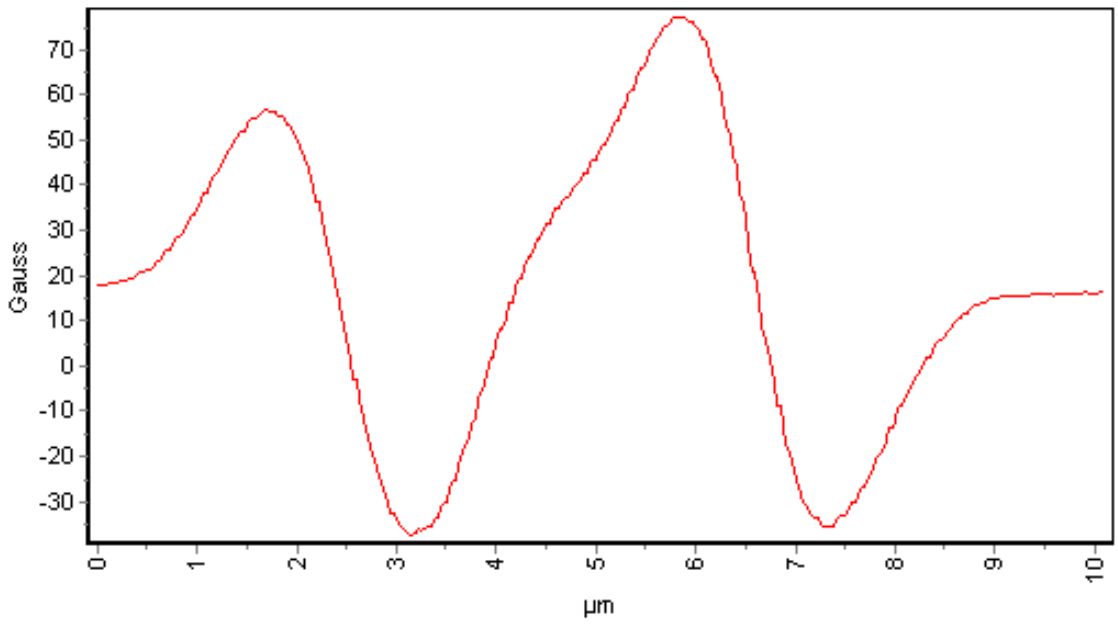

Fig. 36. Magnetic field distribution along the diagonal in Fig. 35.

average flux from a single nanorod in the direction normal to the substrate. Fig. 36 shows values of the magnetic field along the white line shown in Fig. 35. With an average value of 1.5 mT in the $1\mu m \times 1\mu m$ region between the rods, the total flux in the direction opposite to the magnetization direction of the rods is equal to 2/3 of a flux quantum. This value corresponds within a factor of 1.5-2 to the average flux in the opposite direction measured in the same way for a single rod. The rod diameter is 50nm which gives 0.7T for an estimate of the magnetic field on the Co nanorod surface, within the range (0.88T) found for magnetic nanowires in alumina templates [70]. Micromagnetic modeling by the Ross group [68, 69] up to an aspect ratio of 3 shows that, although a small aspect ratio favors a spiral/vortexlike magnetization, at an aspect ratio 3 the magnetization parallel to the nanorod axis prevails, as confirmed by our measurements at this larger aspect ratio.

This study shows that it is technically possible to fabricate magnetic nanos-

tructures which generate spatially alternating magnetic fields on the scale of tens of nanometers and with a field strength in the range of 0.1 to 0.7 Tesla. Such systems have bright prospects for application in different fields.

CHAPTER V

VORTEX PINNING BY MAGNETIC STRUCTURES

It has been shown that a patterned array of magnetic micron and submicron size structures affect an adjacent superconducting thin film layer [22, 23, 24, 50]. As discussed in chapter I, under the right circumstances, a variety of novel effects related to vortex pinning due to the interaction between ferromagnets and superconductors becomes observable. Several hybrid magnet-superconductor systems have been studied in the last decade both experimentally and theoretically (see reviews [17, 18, 71] and references therein). Practically all studies were focused on weak (mT) magnetic fields from arrays of pancake-like magnetic dots [17, 18] or from a network of domain walls in the underlying magnetic film or crystal (see recent works [72, 73, 74] and references in [17, 73]). With probably a single exception [74] magnetic fields from domain wall networks are also in mT range [17, 73]. The typical scale of magnetic field inhomogeneity in all these works on magnet-superconductor hybrids is in the micrometer range.

Typical for most magnet-superconductor hybrids studied, the second critical field H_{C2} is shifted in the 1-10 mT range with respect to a control superconducting system [17, 18, 71, 73]. The critical current changes more strongly [17, 18, 71, 73]. Arrays of magnetic dots provide a 2-D modulation of the magnetic field. Locally domain walls in the underlying magnetic film can be assumed parallel with reasonable accuracy but on the scale of tens of microns they are randomly oriented. Thus, it is very interesting to study the phase diagram and critical current I_C in a one-dimensionally periodic magnetic field (i.e. magnetic stripes). A much stronger influence is expected on superconductivity for this case than from those produced by arrays of magnetic dots or irregular domain wall networks.

Several magnetic structures of interest have been successfully fabricated using both e-beam and photolithography. These structures include macroscopic size arrays of iron - brass stripes and micron size arrays of Co stripes, as well as arrays of submicron size Co or Ni rods. The goal of this chapter is to better determine the nature of the interplay between a superconducting film and these three types of magnetic structures.

Alternating Iron-brass Stripes: Increase of Critical Field and Current in Magnet-superconductor Hybrids

In this study an array of linear magnetically soft iron layers is used to redistribute the magnetic field as shown in Fig. 37. Lyuksyutov and Naugle have previously predicted vortex pinning enhancement by magnetic defects in magnet-superconductor hybrids [75, 76, 77].

They also predicted that soft magnetic rods embedded into a superconductor can increase H_{C2} [77]. A homogeneous magnetic field cannot pin vortices; however an inhomogeneous external magnetic field creates barriers for vortex motion. In this study, experiments for the extreme case when an inhomogeneous magnetic field pins vortices are discussed. The study of this phenomenon can be of great importance for understanding vortex matter in superconductors and for practical applications.

In this work there is a very large period variation of the magnetic field. Nevertheless, with field variations on the scale of tens of microns, the effect of an inhomogeneous field on both H_{C2} and pinning is already strong. Previously an anisotropy was produced in a superconducting film placed atop an array of nickel stripes with inplane magnetization [78]. Strong anisotropy of the critical current I_C was found. However, the role of mechanical modulation of the film due to the underlying nickel

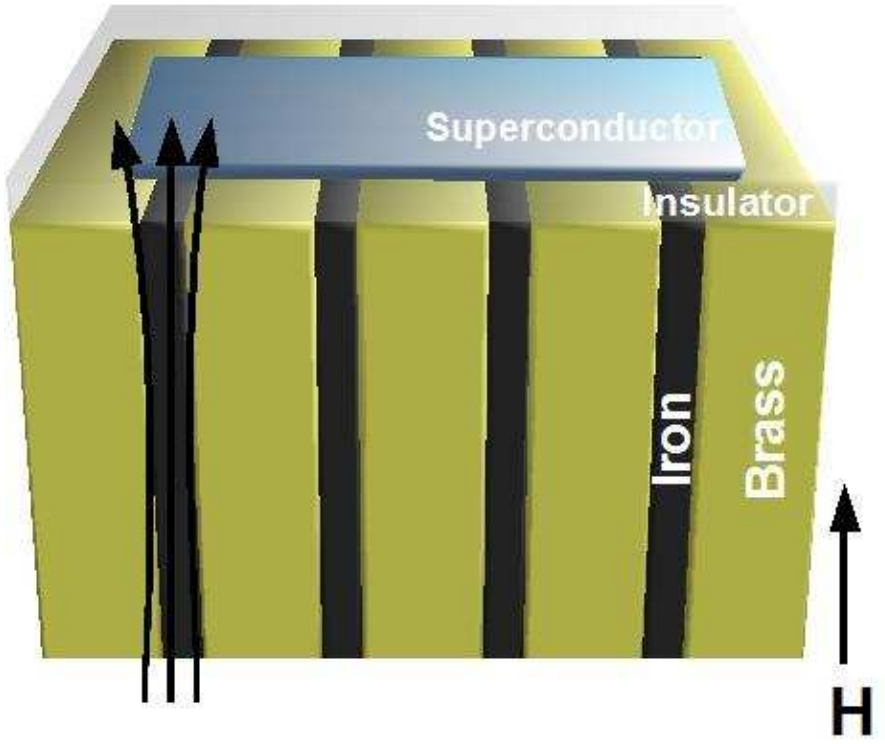

Fig. 37. Schematic design of the magnet-superconductor hybrid system and sketch of the magnetic field distribution when the field is below the saturation values.

stripes is not clear. Thus it is difficult to identify the main source of anisotropy in that experiment.

Alternating sheets of 25μm Fe and 250μm Brass shims were silver soldered to fabricate a laminate magnetic structure as schematically depicted in Fig. 37. The laminate Fe-brass structure was cut perpendicular to the sheets and polished to form smooth laminate substrates. A 5μm thick photoresist, SU-8 2005, was spin coated at 3000 rpm onto the substrate and exposed to UV light to form an insulating barrier. Superconducting thin ($Pb_{82}Bi_{18}$) films of 60nm thickness were deposited at 77K on this barrier in parallel and perpendicular orientation to the stripes by thermal evaporation using a shadow mask. A control sample was deposited on an equivalent non-magnetic substrate.

A NanoMagnetics Instruments scanning Hall probe microscope (SHPM) was used to image the perpendicular component of the surface magnetic field distribution shown in Fig. 38 (a). The sample was scanned at room temperature on a motorized X-Y stage at a height of approximately 5μm above the film. During the scan the sample was mounted on a permanent rare-earth magnet to keep it magnetized. This image illustrates the redistribution of the magnetic field by the magnetic sheets. The permanent magnet is used to apply a uniform field of about 0.15T. Fig. 38 (b) shows a SHPM line scan taken perpendicular to the magnetic field stripes. Samples were later mounted in a cryostat (Quantum Design PPMS) and field cooled to 10K in a 1T applied field. The applied field was then removed, and resistance vs. temperature $R(T)$ data were collected using a standard four-point method at various fields up to 1.4T. T_C of the three samples at different applied field values was determined by extrapolating the steepest part of the $R(T)$ curve to the residual resistance value ($\approx R(8K)$ with $H = 0$.

Typical normalized resistance curves for the current parallel, perpendicular to the

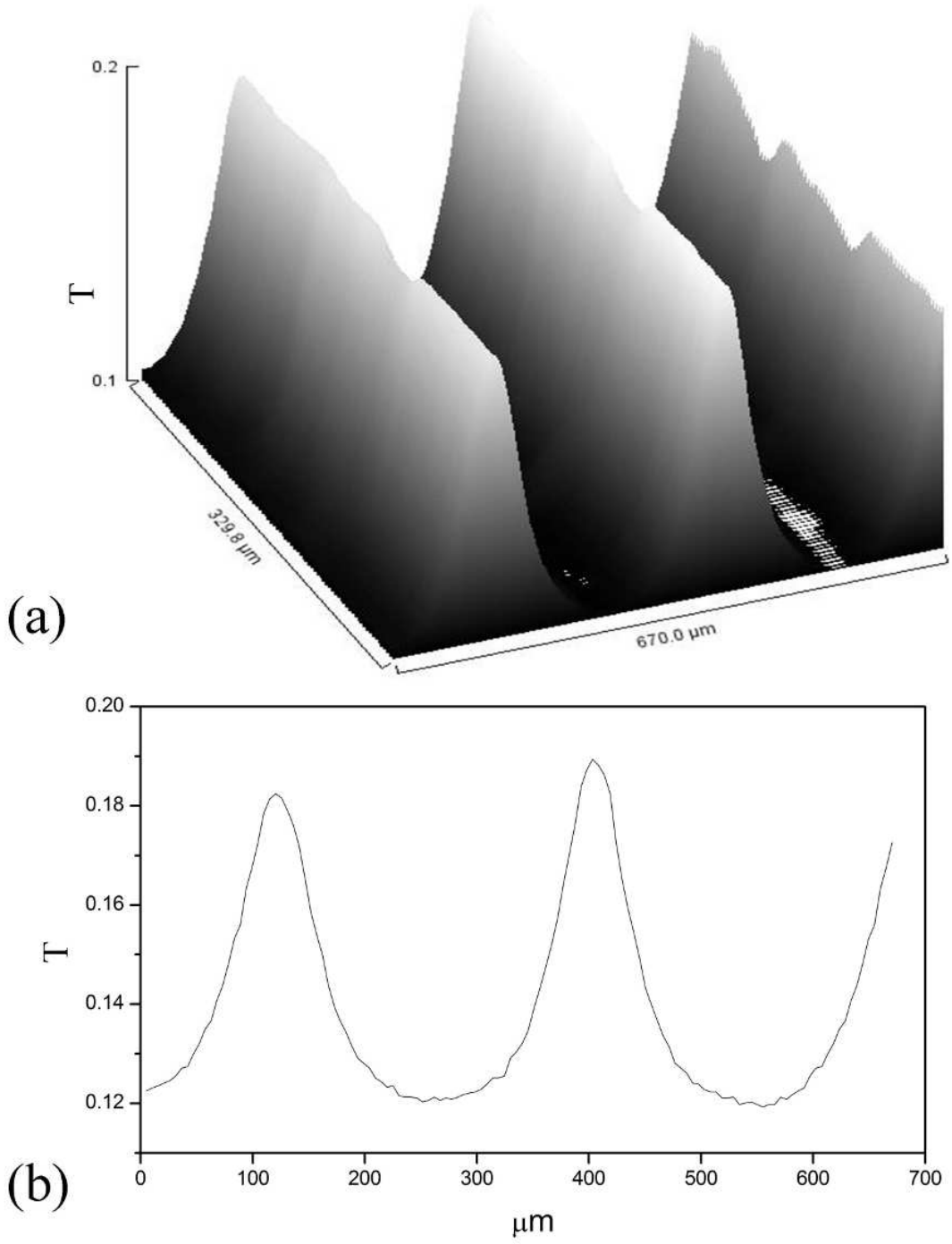

Fig. 38. (a) Normal component of magnetic field about 10μm above Fe-brass laminate measured with SHPM. (b) SHPM line scan perpendicular to the magnetic field stripes in (a).

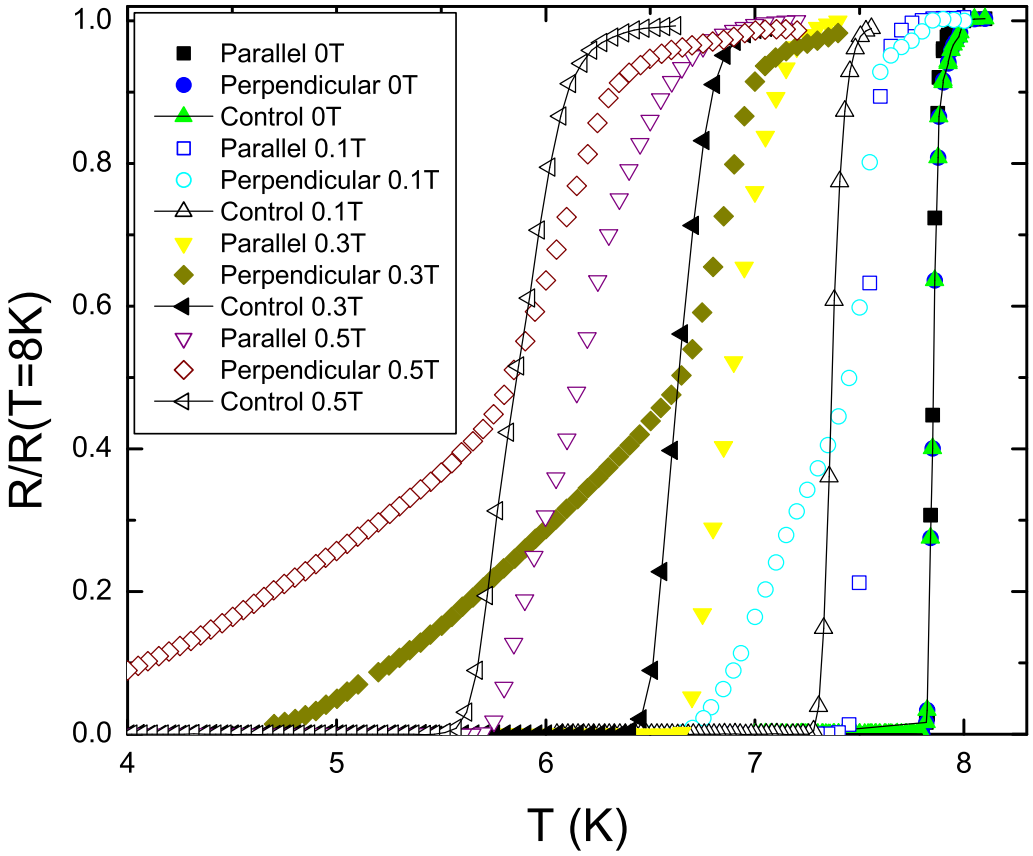

Fig. 39. Normalized resistance curves $R(T)/R(8K)$ for the current parallel and perpendicular to the magnetic stripes and for the control sample for $\mu_0 H$=0, 0.1T, 0.3T, 0.5T.

magnetic sheets and the control sample are shown in Fig. 39 for different values of the magnetic field ($\mu_0 H$=0, 0.1, 0.3, 0.5 T). Fig. 40 shows $\mu_0 H_{C2}(T)$ for current parallel and perpendicular to the magnetic stripes and for the control sample. The sample with current perpendicular to the magnetic stripes exhibits parts with quite different $T_C(H)$ that are effectively in series so that defining the critical current density J_C for that case is complicated and somewhat meaningless. This also gives an anomalous extra broadening of $R(T)$ in a magnetic field which makes $H_{C2}(T)$ less reliable for that case. Often the midpoint of the $R(T)$ curve or the extrapolation of the steepest part to $R = 0$ is chosen to determine $H_{C2}(T)$ for inhomogeneous thin films. Though the slopes of $H_{C2}(T)$ change with these choices, the relative behavior for the control film and current parallel to the stripes is not qualitatively different from that shown in Fig. 40.

The critical current I_C was determined by measuring I-V curves at various temperature and applied field values. The criterion for the I_C was chosen to be the current value at which the voltage drop across the sample reached 2μV (as described in Chapter III.). The highest I_C value measured corresponds to only about 20 $\mu\Omega$ while for the lowest value corresponds to about a $m\Omega$, as opposed to the 10Ω residual resistance value when the sample was in the normal state.

The magnetic field distribution normal to the superconducting film has been measured by SHPM (Fig. 38 (a), 38 (b)). These scans are taken at room temperature about 10μm above Fe-brass laminate or, equivalently, 5μm above $Pb_{82}Bi_{18}$ film. The amplitude of magnetic field variation measured is smaller than that actually present on the surface of the film due to the decay of the field strength with distance from the surface (see e.g. [79]).

The high amplitude periodic field variation on the surface of the superconducting film means that different values of the H_{C2} and critical current I_C for current

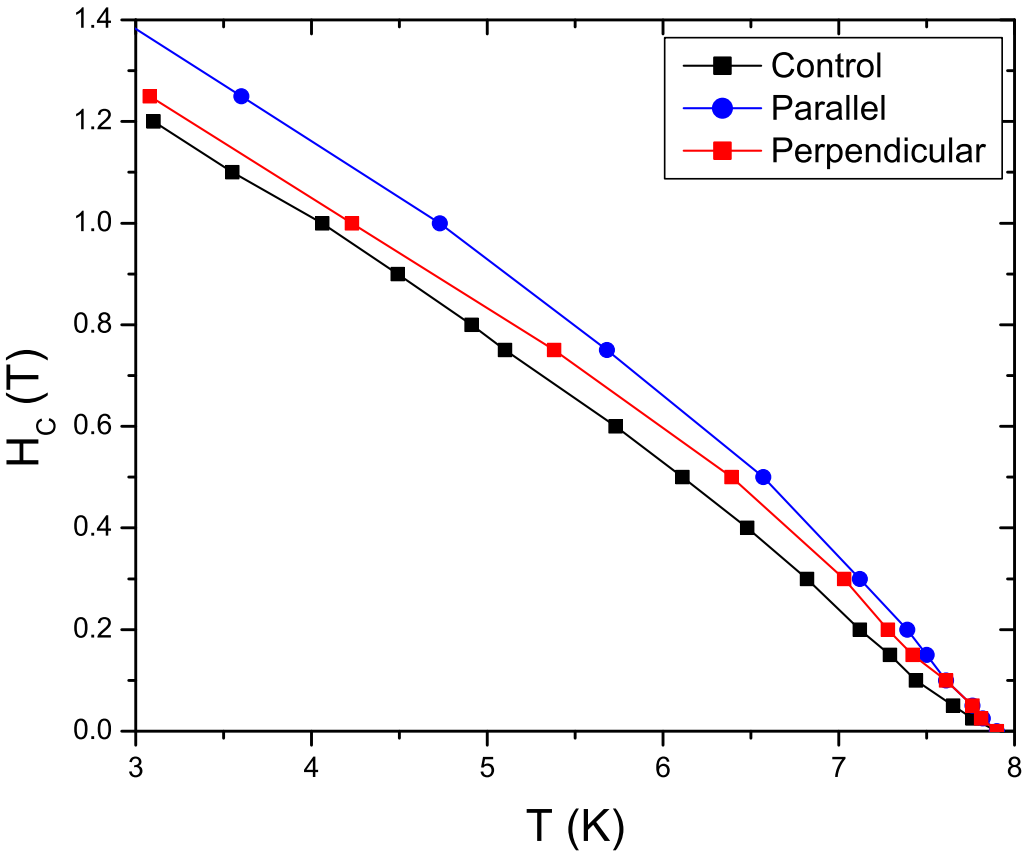

Fig. 40. $\mu_0 H_{C2}(T)$ for the current parallel and perpendicular to the stripes and for the control film. Lines are guides the eye.

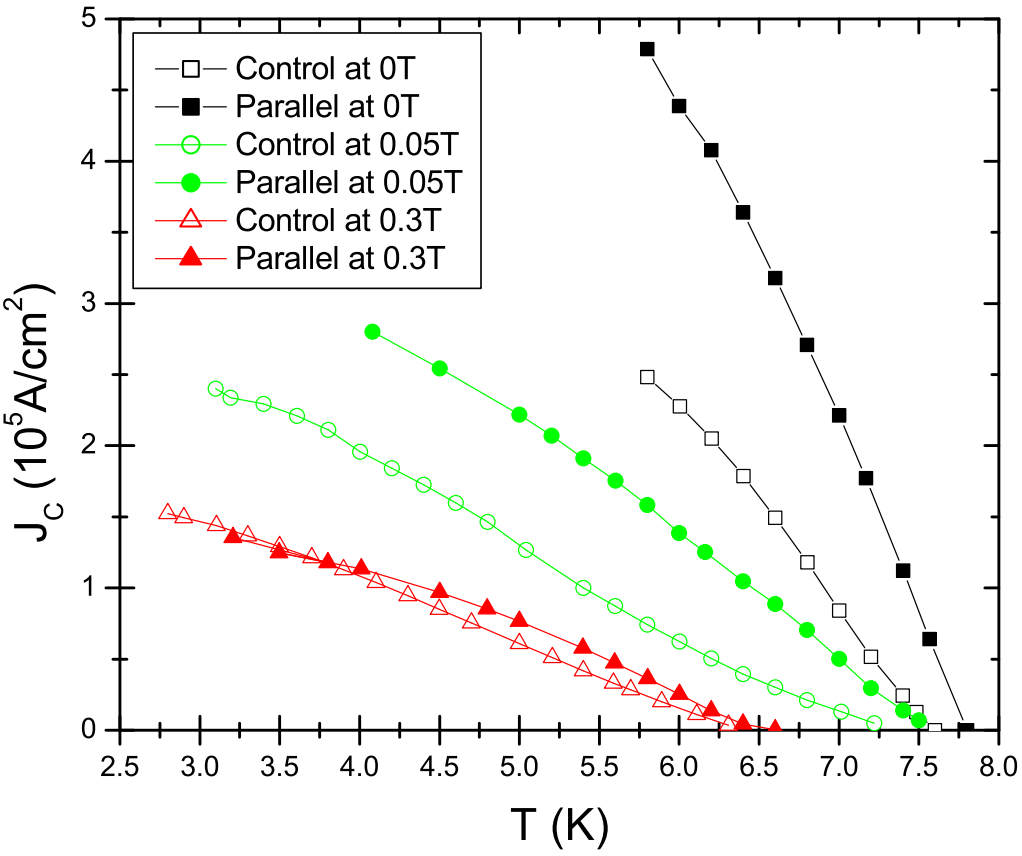

Fig. 41. Average critical current density J_C for current parallel to the stripes and for the control sample for ($\mu_0 H$ =0, 0.05, 0.3 T).

directions parallel and perpendicular to the magnetic stripes and the control film are expected. Indeed, the resulting magnetic field at the superconducting film above the brass stripe is lower than the applied magnetic field H, and the resulting field at the film above the iron stripe is higher than H. The second effect which needs to be taken into account is that the effective field is distributed inhomogeneously across the stripes. Since H_{C2} increases as T decreases, a larger portion of the film over the brass becomes superconducting while a smaller portion of the film over the iron is driven normal by the field as the temperature is decreased. These two effects can explain the differences between the measured H_{C2} for current parallel to the magnetic stripes compared to that of the control film as shown in Fig. 40. In Fig. 41 the average critical current density J_C (determined as I_C divided by the film crosssection) for current parallel to the stripes and the control film is shown. For $H < 0.3T$ J_C is higher above 4K for the film with current parallel to the magnetic stripes than for the control film. The enhancement in the self field near T_C is orders of magnitude due to a greatly enhanced pinning by the magnetic stripes. Note that in an applied field, the local J_C is very inhomogeneous for the current parallel to the stripes since J_C is enhanced above the brass region and it is reduced above the Fe region by the inhomogeneous field.

Fig. 38 (b). shows the distribution of the normal component of the field at a distance $d = 5\mu m$ from the superconducting film. The simple analysis presented in [79] shows that in a very large system the amplitude of the magnetic field variation drops exponentially with the distance from the film with a characteristic decay approximately equal to the period of the structure i.e. 275 μm. This period is much larger than d. Thus, Fig. 38 (b). gives an estimate of the magnetic field variation in the superconducting film that is of the order of a few tenths of a Tesla. Bulaevskii et al [80] have estimated vortex pinning due to the spatial variation of magnetic field due

to domains of different polarity in the ferromagnet. Substitution of the magnetization of the ferromagnet with the magnetic field at the superconducting film generated by the magnetized Fe stripes leads to a simple formula for the critical current density $J_C \approx \mu_0^{-1} dB/dx$. dB/dx is estimated to be about 0.1T over the length of $100\mu m$ from the data in Fig. 38 (b). As a result the critical current density is estimated to be about $10^5 A/cm^2$, in order of magnitude agreement with the data in Fig. 41.

This experiment demonstrates [81] that an inhomogeneous magnetic field can effectively pin vortices in an otherwise homogeneous superconducting film. The enhancement of $H_{C2}(T)$ for this hybrid magnet superconductor structure can be reasonably well described in terms of magnetic field redistribution due to the iron laminate.

Magnet-superconducting Hybrid Persistent Current Switch

As it was presented in previous section, FM stripes create a large dependence of I_C in current direction. In this study the possibility of using the current anisotropy in hybrid systems with 1D magnetic field modulation (i.e. FM stripes) to fabricate a functional SC-FM hybrid device is investigated. The capability of switching the SC on and off by changing the current direction in that SC with respect to the adjacent FM layers, makes devices like SC switches and SC current valves possible.

Persistent current switches are used to control the charging and discharging process of superconducting (SC) magnets. A SC switch is driven normal to allow the power supply to ramp the current to the desired value and the switch is later driven into the SC state to complete a SC closed loop. In this persistent state, the current in a SC magnet can last extended periods of time without any significant loss of energy. Driving the persistent switch back and forth between normal and SC state is generally achieved by heating a small portion of the switch (Joule heating) above

its critical temperature T_C [82]. In [20, 21] a good alternative to Joule heating is proposed by magnetically switching SC but it still requires controlling an externally applied magnetic field by a current source.

In many persistent current applications (i.e. magnetic resonance imaging, magnetic levitation and scientific instrumentation etc.) low power, fast response and small size would be extremely useful. In the previous Chapter (V.) the critical current I_C for a hybrid magnet superconductor was observed to be enhanced when the current was parallel to a series of Fe walls compared to a control sample [81]. Based on the results of this previous section, a novel technique for a mechanically driven SC persistent switch has been proposed and tested with a $Pb_{82}Bi_{18}$ alloy superconducting film. In contrast to other mechanical switch designs [83, 84, 85], this technique uses permanent contacts between the SC magnet coil and the switch leads; therefore, wear over many switching cycles is minimized, and sharp changes in current value during switching process is avoided. The switch can function at a fixed 4.2K temperature immersed in liquid He along with the SC magnet coil.

Technique proposed for mechanically driven persistent switch poses a number of advantages:

- There is no heat dissipation associated with Joule heating, therefore precious cryogenic resources can be conserved.

- The very short response time is limited by the speed of physical rotation of the switch, therefore lengthy heating and cooling cycles can be avoided; Typically around 200 sec for warming and even longer for cooling.

- Switches can be batch-fabricated using standard micro-fabrication processes providing compact and low-cost device structures.

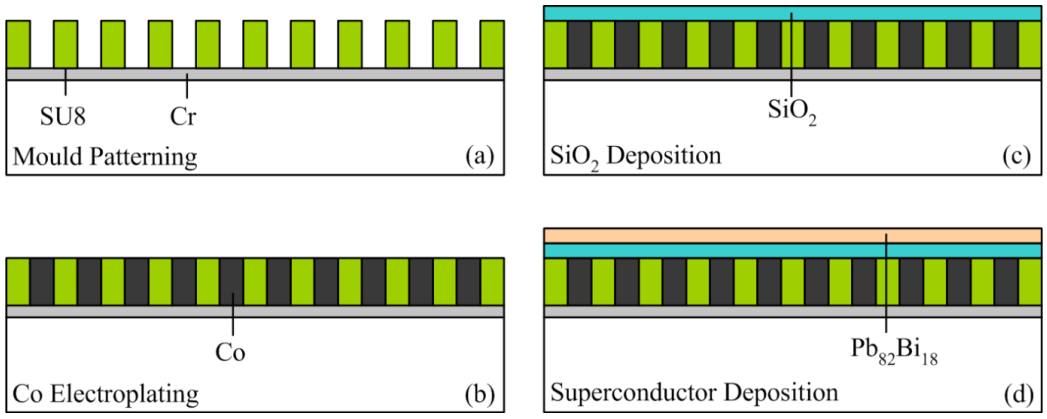

Fig. 42. Fabrication process for the micro-machined superconducting persistent current switch.

- The SC material and magnetic substructure for the switch can be chosen to permit operation under liquid He or liquid N_2.

The device is comprised of three layers stacked on top of each other. The bottom layer is the magnetizing Co stripes, on top is the superconducting film, and an oxide layer is sandwiched between them for insulation and to prevent proximity effects.

The fabrication process for the switch is illustrated in Fig. 42. Silicon was chosen as the substrate material and a 150 nm thick Cr seed layer was thermally evaporated (Fig. 42a). Next, SU(8)-5 was spin coated at 2000 rpm, and patterned to create $7.5\mu m$ deep and $3.5\mu m$ wide trenches (aspect ratio of more than 2) with a period of $10\mu m$ to serve as a mold for subsequent Co electroplating (Fig. 42b). After electroplating Co, a 200nm layer of SiO_2 is e-beam deposited as an insulator (Fig. 42 c). Finally, 100nm of $Pb_{82}Bi_{18}$ alloy is thermally evaporated at 77K (Fig. 42d). In order to test the concept a test structure composed of two separate $Pb_{82}Bi_{18}$ films was deposited on the same substrate i.e. one with current flow direction parallel to the Co trenches and one with perpendicular orientation as shown in Fig. 43. Figs. 44,45 show SEM micrographs of the substrate after electroplating Co.

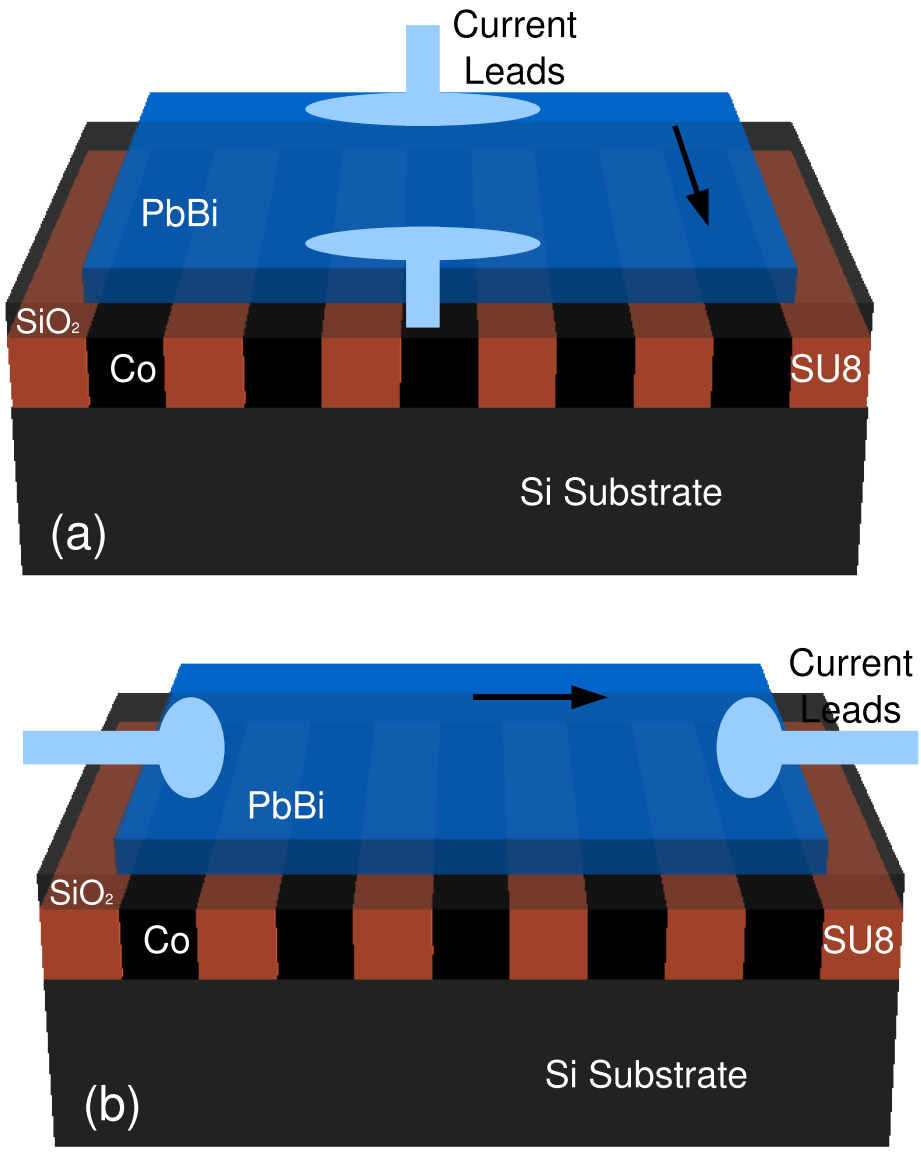

Fig. 43. Schematic drawing of the superconducting-magnetic hybrid persistent switch test structures.(a) sample with current direction parallel to the Co trenches, (b) sample with current direction perpendicular to the Co trenches.

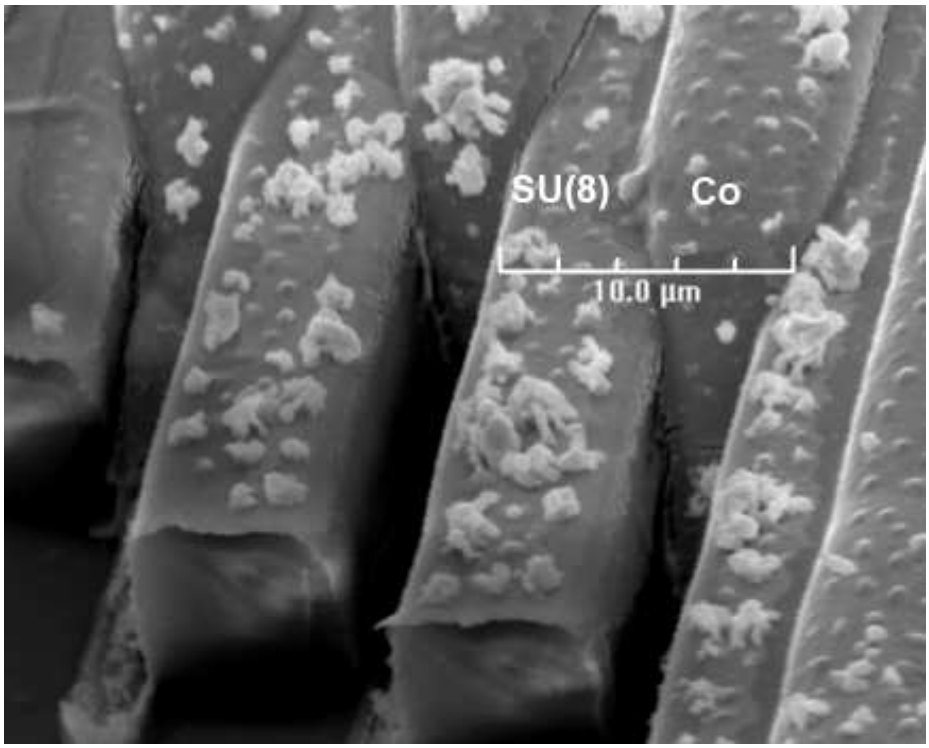

Fig. 44. SEM micrograph of patterned photoresists slightly overfilled with Co after electroplating (45^o view).

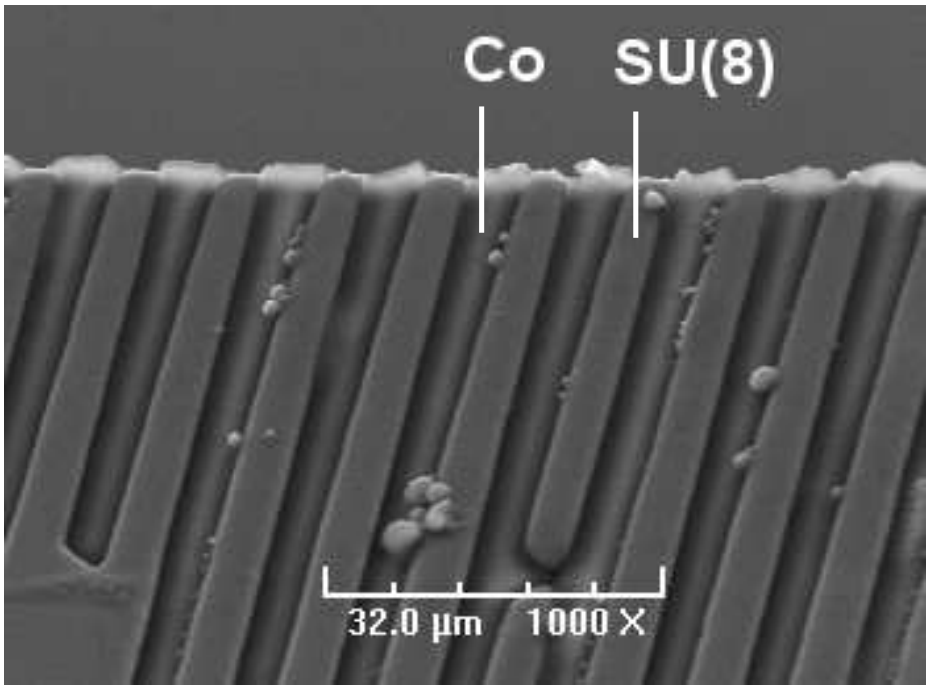

Fig. 45. SEM micrograph of patterned photoresists slightly underfilled with Co after electroplating (top view).

SHPM imaging was then performed in PPMS at room temperature and 5kOe applied field. Fig. 46 shows the periodic magnetic field variation of the substrate. The apparent distortion in Fig. 46 is due to a slight miscalibration in the electronics that control the Hall probe positioning. Also, the magnetic field profile (Fig. 47) indicates that there is approximately ≈3kG difference between the field regions above Co trenches and photoresist ones. At 5kOe applied field, magnetic field at the regions directly above the Co stripes is around 6.8kG as opposed to that of 3.7kG above the nonmagnetic regions. In addition to images of magnetic field distribution, the SHPM was also used to acquire B-H curves above the magnetic and nonmagnetic regions at 50K (Fig. 48). B-H curves indicate that the relative high permeability of Co stripes effectively channels the flux lines until Co reaches saturation at about ≈3kOe applied field. After the saturation of Co stripes, the magnetic field increases uniformly.

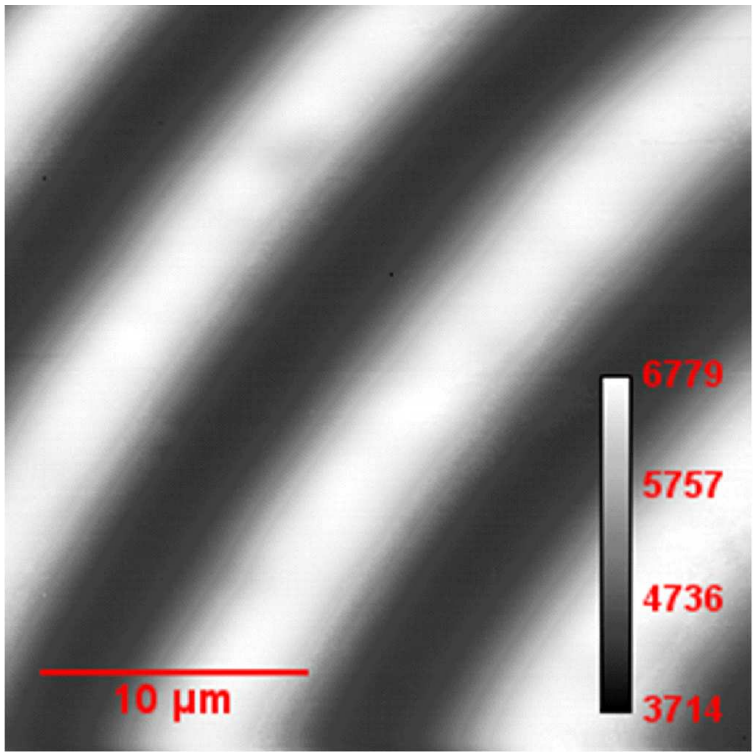

Fig. 46. SHPM image of the hybrid sample at 300K and 5kOe applied field. Image was acquired in STM tracking mode at a Hall probe sample separation of ≈200nm. Values of B on the gray scale are in Gauss.

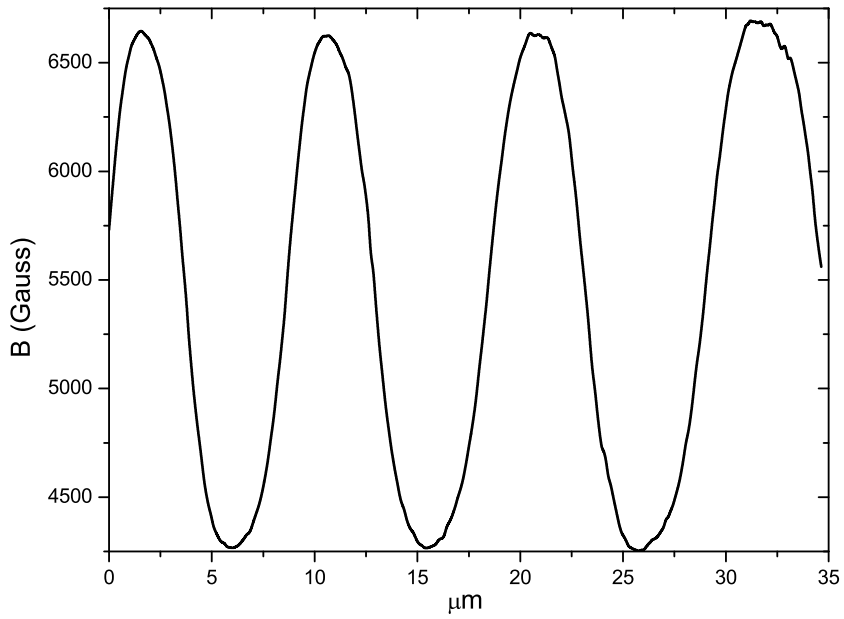

Fig. 47. Magnetic field profile across the Co stripes measured with SHPM.

Second critical field H_{C2} was also acquired by measuring T_C of a nonmodulated control film of the same thickness at different applied field values up to 10kOe (Fig. 49). A different criterion than that used in the previous section was chosen in determining T_C. For a switch application, first signs of a voltage across the sample is more relevant. Therefore, T_C was determined by the lower 1% point of the resistive transition curve $R_H(T)$. Consequently, the $H_{C2}(T)$ values presented here are somewhat smaller than those shown for a $Pb_{82}Bi_{18}$ control film shown in Fig. 40 due to this different criterion.

The critical current density I_C was determined by measuring I-V curves at 4.2K for various applied field values. In preparation for I_C measurements, the sample was first magnetized at 5kOe applied field then the field was removed. The criterion for the I_C was chosen to be the current value at which the voltage drop across the sample

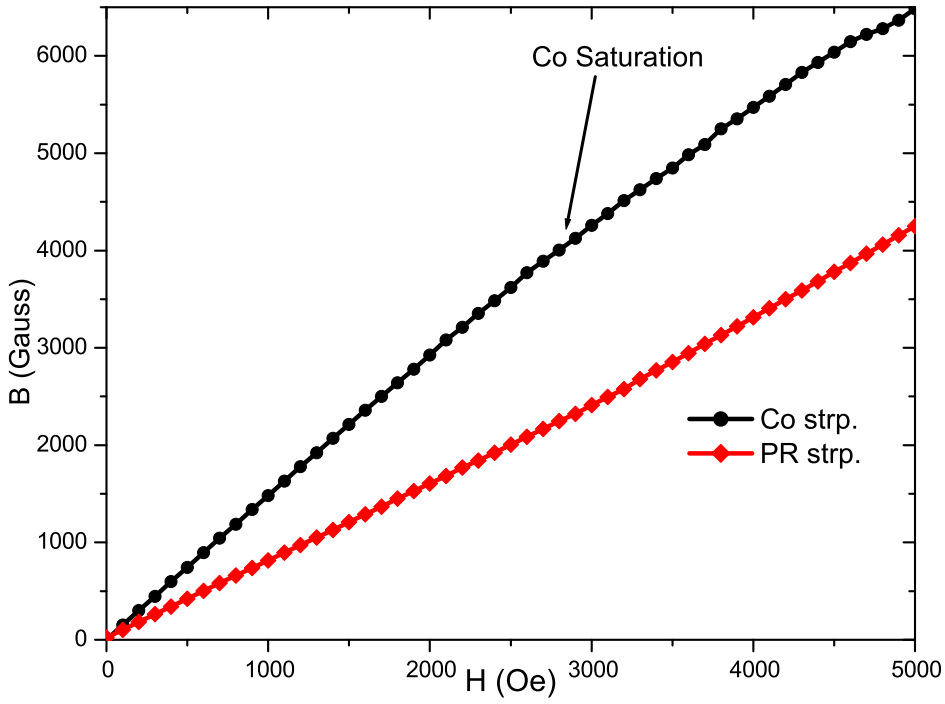

Fig. 48. B-H curves above Co stripe (round symbol) and photoresist (square symbols) at 50K.

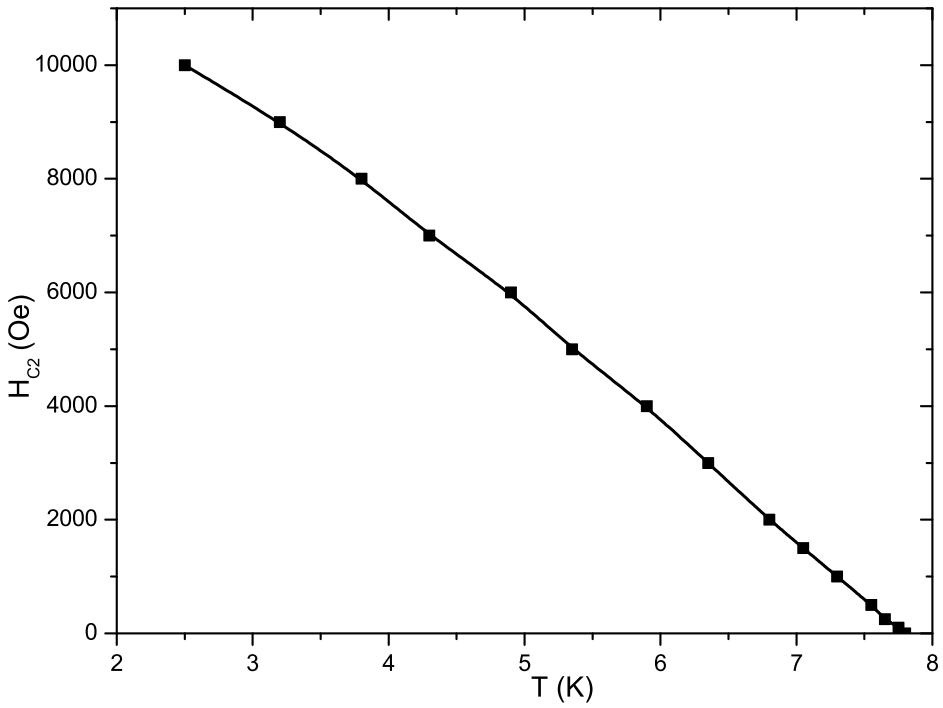

Fig. 49. $H_{C2}(T)$ plot of non-modulated control film.

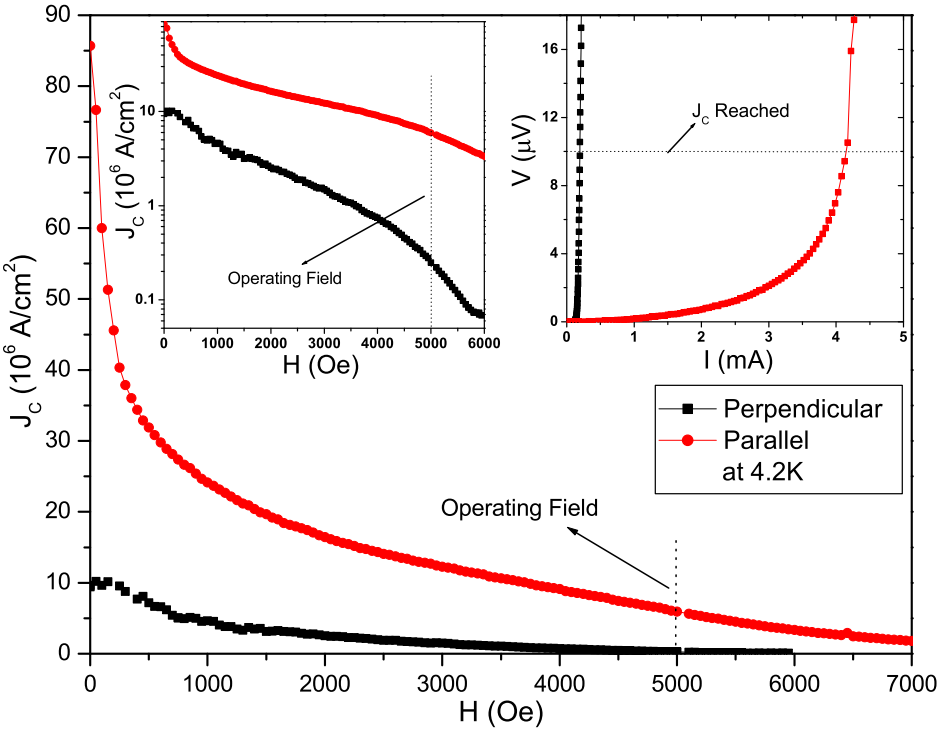

Fig. 50. Critical current density $J_C(H)$. Inset 1: Same data in log scale. Inset 2: I-V curves at 4.2K and 5kOe for both current directions.

reached 10μV. This criterion was chosen to be larger than the typical 1μV in order to be consistent with the other switch work in the literature [20, 21]. The crossection of the sample was then used to calculate J_C. Fig. 50 indicates the strong dependence of J_C on current direction. Also inset 2 in Fig. 50 shows a sample I-V curve at 4.2K and 5kOe applied field. For this I-V curve the ratio of critical currents for the two samples was around $\approx$40.

Transport measurements of J_C for both current orientations and H_{C2} of a control sample, combined with SHPM magnetic characterization of the substrate demonstrates that the proposed technique has potential application in functional device development. However, there are still some challenges that need to be overcome be-

fore a working prototype is fabricated. A functioning persistent switch using this technique requires fabrication of two major units (Fig. 51).

1. An array of Co stripes similar to the one that was described above, fabricated on top of a 5kOe - 7kOe permanent magnet. The permanent magnet will serve to keep the Co stripes magnetized at all times. The magnetic structure fabricated will require careful polishing, since this surface will be the interface between the two units.

2. A SC film deposited on top of a suitable substrate such as silicon wafer. The SC film will be buried in a protective coating such as low temperature epoxy once the permenant current contacts are made. The bottom side of the S substrate will then need to be polished to a thickness of a few micrometers. Again, this surface will be the interface between the two units. The remaining thickness of this substrate after polishing is critical. For proper operation of the switch, the substrate can not be thicker than a fraction of the width of Co stripes to prevent straying of the modulated magnetic field.

The entire switch assembly would be operated in the liquid He bath along with the SC magnet. Once the two units are fabricated, the switching action can be done by rotating the magnetic substrate 90^o with respect to the SC film assembly above. The magnetic substrate will create alternating SC and normal regions in the SC film above. Regions directly above the Co stripes will experience a magnetic field above the second critical field $H_{C2}(4.2K)$ and thus will be driven normal (Fig. 47, 49). On the other hand, regions directly above the photoresist stripes will remain superconducting. As is schematically depicted in Fig. 52, current flowing in SC film will either flow parallel to the Co stripes below (the switch is in SC state) or

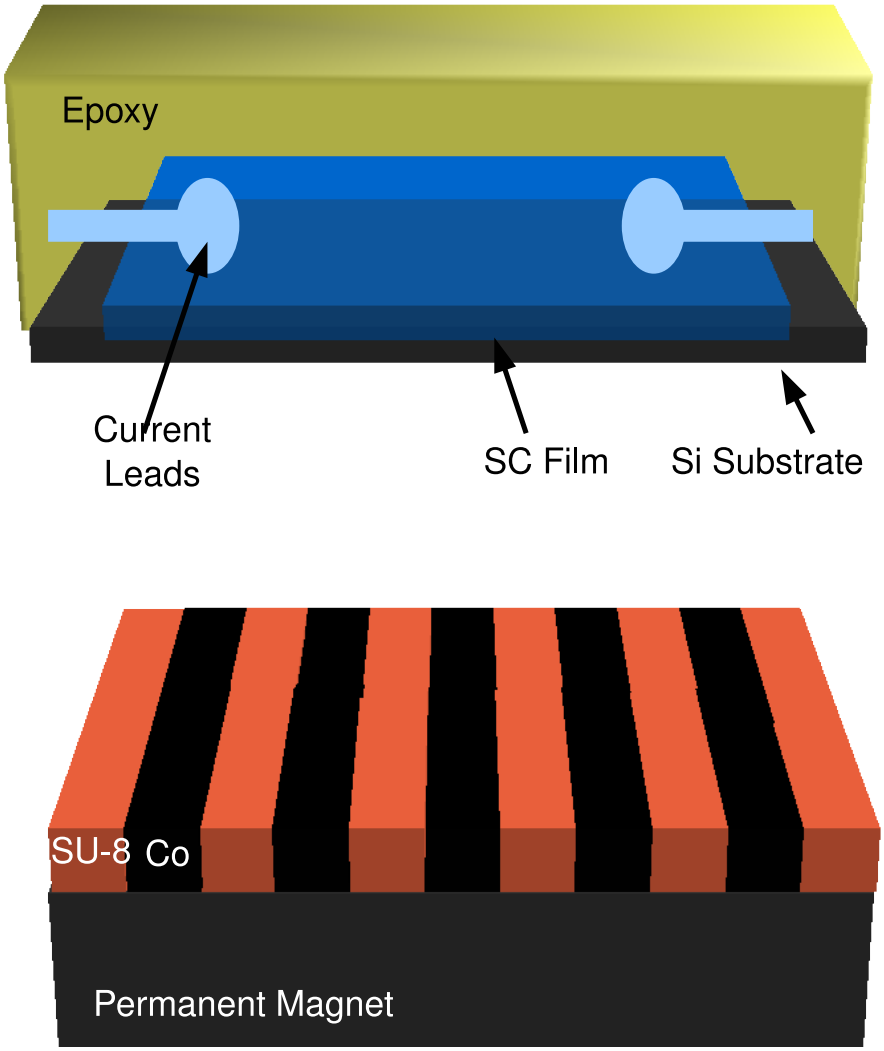

Fig. 51. Two units that make up the switch assembly.

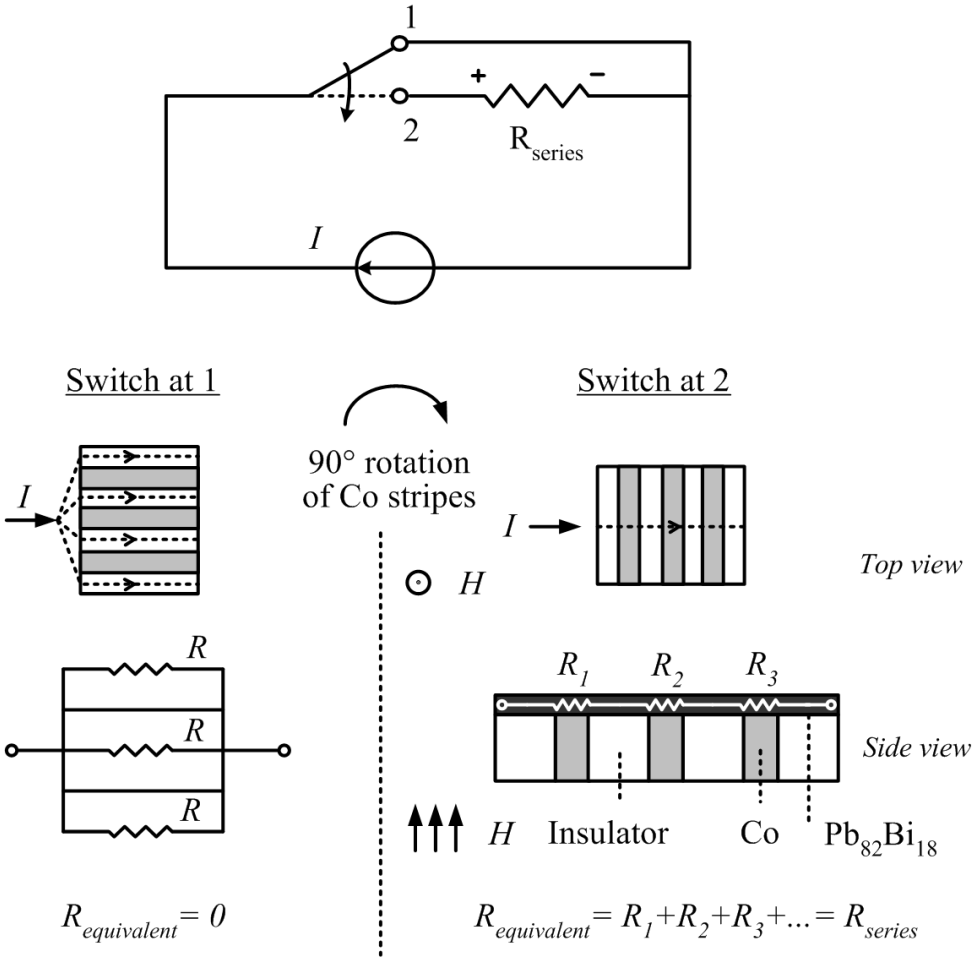

Fig. 52. Schematic illustrating the operation principle of the superconducting switch.

perpendicular to the Co stripes (the switch is in normal state) depending on the relative orientation of the two units.

Pinning Effects of High Aspect Ratio Ni Rods

In this section, effects of a square array of high aspect ratio (≈ 7) Ni columnar nano structures embedded in a SC $Pb_{82}Bi_{18}$ thin film on critical transport current I_C will be presented. An array of 50nm diameter Ni columnar nanostructures was fabricated on a silver coated silicon wafer in a similar fashion to that described in Chapter IV.

Then, a 100nm thin film of $Pb_{82}Bi_{18}$ was evaporated onto the structure after removing PMMA. An additional 100nm thin film of $Pb_{82}Bi_{18}$ was simultaneously deposited on the same substrate without the Ni nanorods as a control sample. The array period was 250nm; thus, SHPM imaging could not be directly performed on this sample due to its limitation in resolution. However, in Chapter IV. SHPM and MFM imaging was performed for a similar system with a $2\mu m$ period. A large variation in magnetic field strength was observed ($\approx 0.1T$ to $\approx 0.7T$). Also, it was shown that each Ni nanorod remained single domain even at room temperature.

Critical current I_C measurements were performed with a standard AC four probe technique in the PPMS. The I_C was determined by measuring I-V curves at each temperature and applied field value. The criterion for the I_C was chosen to be the current value at which the voltage drop across the sample reached $1\mu V$. This criterion was chosen considering the accepted convention $1\mu V/cm$ that was discussed in Chapter III. and measurement limits of the AC transport option of the PPMS. Since both the control and the hybrid sample were fabricated with the same physical dimensions, I_C instead of J_C (critical current density) is presented. At every temperature before starting the magnetic field sweep, the sample was magnetized in a 2kOe applied field in a direction opposite to that in which the field was being ramped.

Due to the large aspect ratio, the Ni rods retained their out of plane magnetization once magnetized above saturation. This property leads to a significant hysteretic behavior in the I_C measurements (Fig. 53). Fig. 53 shows the variation of I_C of the hybrid sample with changing applied field at T=7.4K, 7.6K, 7.7K and 7.75K. The main source of hysteresis can be identified as follows; the Ni rods can initially retain their magnetization either parallel or anti-parallel to the applied field. In the case of parallel magnetization; flux lines due to the Ni rods forming a closed loop will partially cancel out the flux lines due to the applied field in regions between the rods,

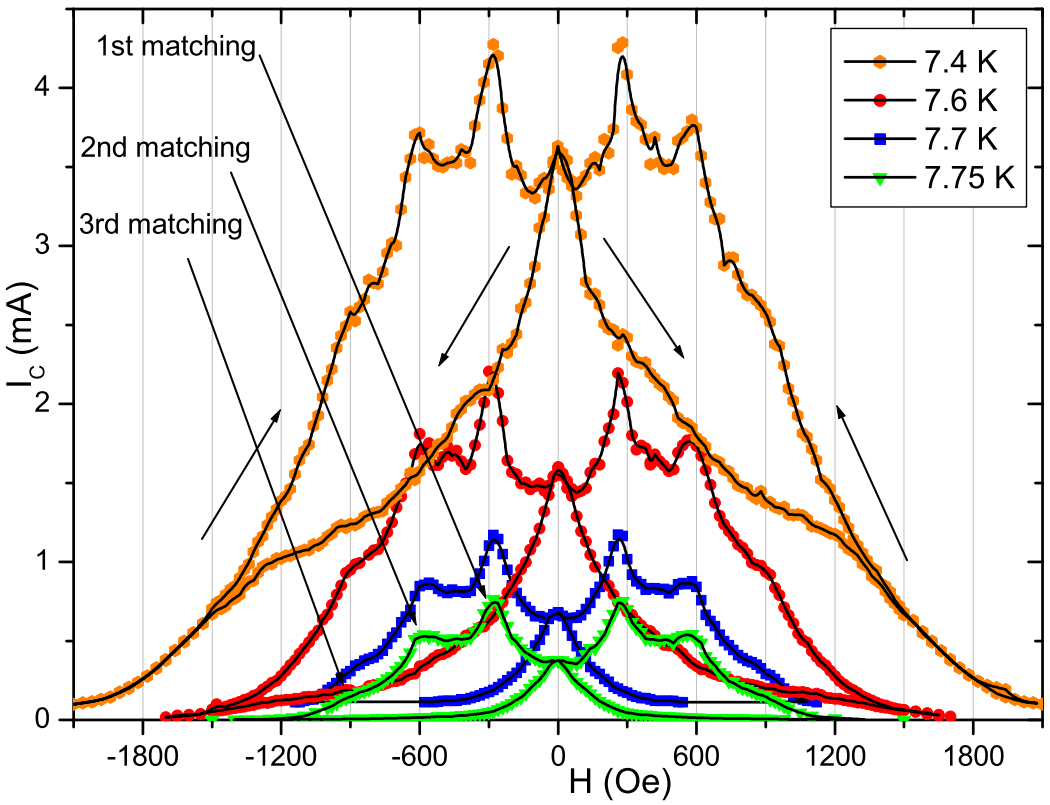

Fig. 53. $I_C(H)$ Field sweep for hybrid sample at T=7.4K, 7.6K, 7.7K and 7.75K.

as illustrated in Fig. 4, reducing the effective magnetic field on the SC film. In the case of anti-parallel magnetization; flux lines forming a closed loop will actually add to the net flux due to the applied field, further increasing the effective magnetic field on the SC film. This anisotropy between ramping the field up or down disappears when the Ni rods are fully saturated at ($\approx 1200G$) parallel to the applied field (Fig. 53).

Due to an increase in pinning when the vortex lattice is commensurate with the lattice of magnetic pinning centers, a matching field effect was observed when the applied field was in the same direction with the magnetization of the rods. Three

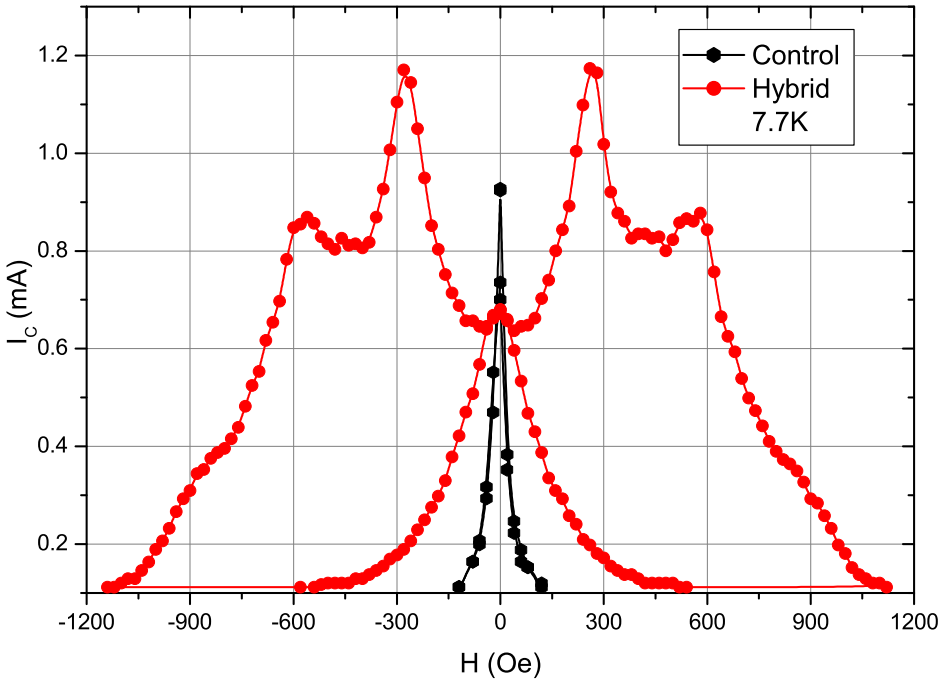

Fig. 54. $I_C(H)$ Field sweep for control and hybrid sample at 7.7K.

matching field peaks are clearly visible in Fig. 53 for applied fields that are integer multiples of slightly less that $300Oe$. The theoretical matching field corresponds to one flux quantum per unit lattice cell (as discussed in Chapter I.) (Eq. 5.1).

$$H_{match} = \frac{\Phi_0}{D^2} \tag{5.1}$$

Here $D = 250nm$ is the period of rods in the square lattice and $\Phi_0 = \frac{h}{2e} = 2.06 \cdot 10^{-15}Wb$. Thus Eq. 5.1 yields a theoretical value of $H_{match} = n \times 329Oe$ (n is an integer). The observed matching field value of $H = 300Oe$ is close to the calculated value.

Fig. 54, 55, 56 indicate a large I_C enhancement with applied field in the hybrid sample compared to control sample of same thickness, except very close to H=0. Due

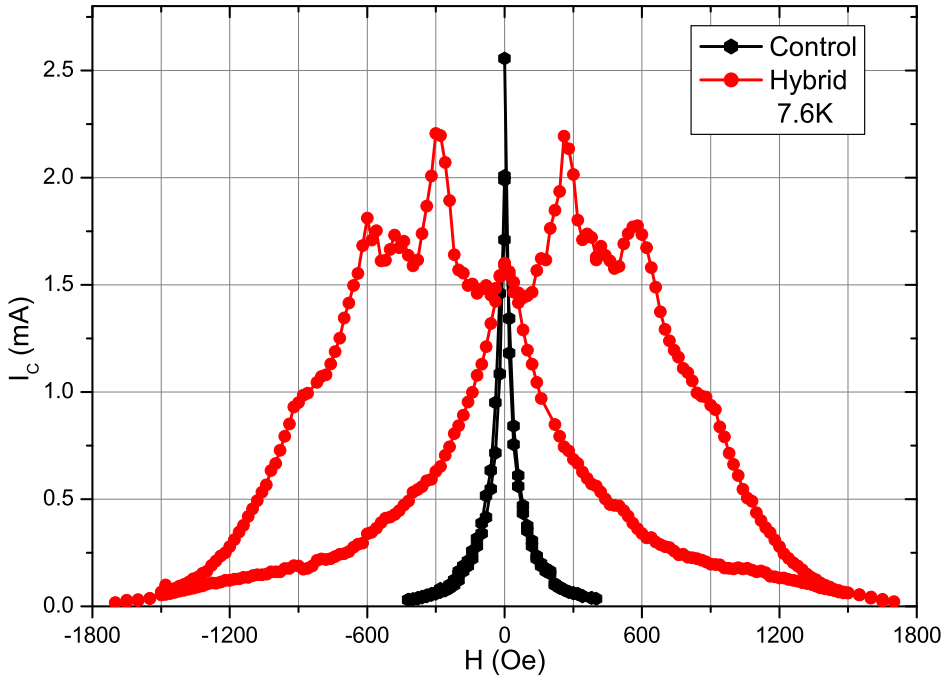

Fig. 55. $I_C(H)$ Field sweep for control and hybrid sample at 7.6K.

to larger vortex size, pinning is stronger when the temperature is closer to the T_C. Fig. 57 shows the I_C enhancement of a hybrid sample at the first matching field for different temperatures. This enhancement in I_C was defined as the ratio of critical currents of hybrid and control samples measured at the first matching field peak ($\approx 300Oe$). Coupled with the observed matching field effect, this enhancement in I_C is a clear evidence for additional vortex pinning in the hybrid sample.

Altough Fig. 57 was measured in the case of parallel alignment of Ni rods and the applied field, I_C is still enhanced significantly for the anti-parallel alignment case (Fig. 54, 55, 56). Enhancement in I_C for anti-parallel and parallel cases (field ramped up and down respectively) presents different physics. In the case of anti-parallel alignment (the field is being ramped up) there is no matching field effect. Since the

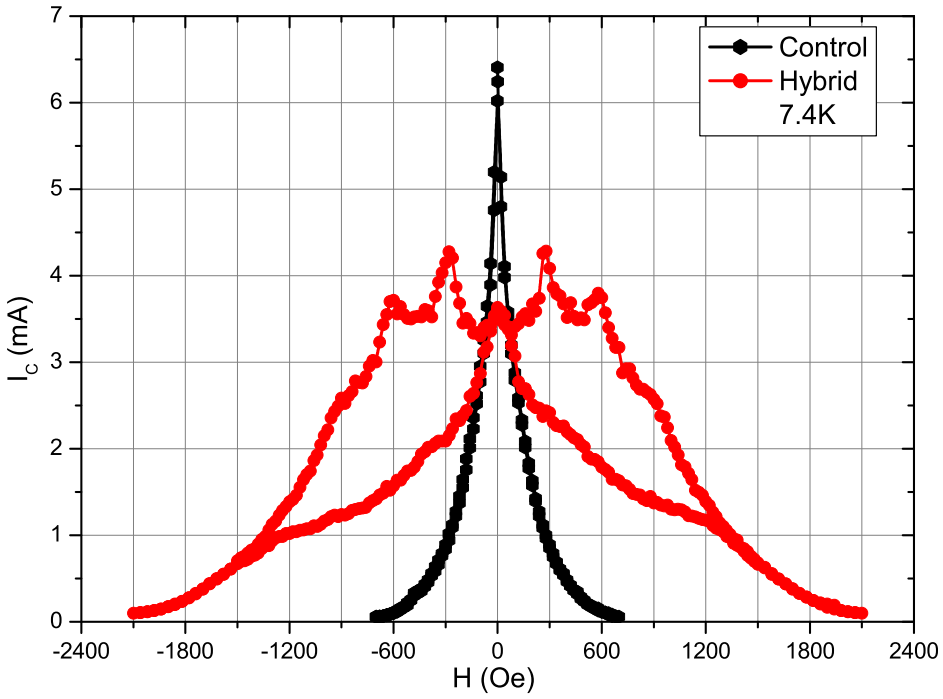

Fig. 56. $I_C(H)$ Field sweep for control and hybrid sample at 7.4K.

return field due to the Ni rods and the applied field add in this case, the compensation effect works against the enhancement. However, there is still an enhancement in I_C, except again for H very close to zero. This indicates that the Ni nanorods form very effective pinning sites on the SC film. In the case of parallel alignment (the field is being ramped down from a higher value) field compensation and pinning work together. Thus the enhancement in I_C is very large compared to the control film except for H close to zero. In the hybrid system, due to the protruding nanorods the effective crossection of the sample is smaller. This can explain the higher I_C of the control sample near H=0.

I-V measurements demonstrate similar evidence. The I-V plots in Fig. 58 show that at zero applied field I_C of the control sample is higher than that of the hybrid

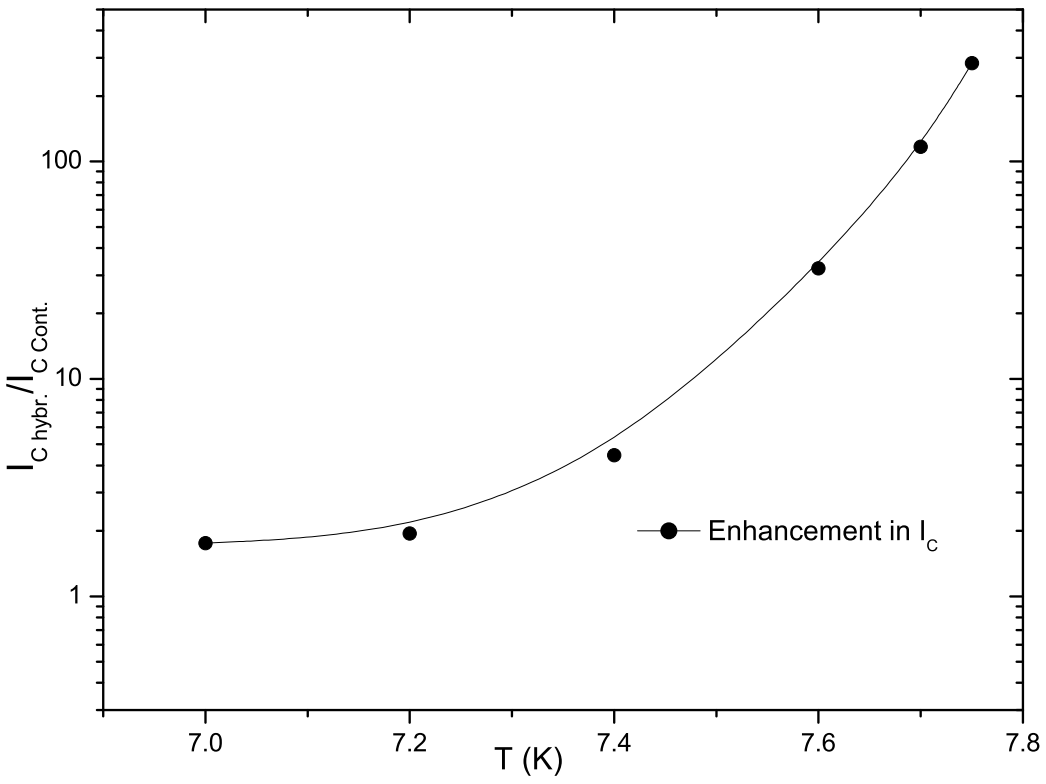

Fig. 57. Enhancement of I_C as a function of temperature in Log scale. Enhancement was defined as $I_{C-Hybr.}/I_{C-Cont.}$ measured at the first matching field (H=0Oe).

sample, however as the applied field is increased, the value of critical current of the hybrid sample is significantly enhanced.

The typical I-V curve for a SC shows a near zero voltage response for a ramped current until it reaches the break-down point of the vortex lattice (see I-V plot for the control sample in Fig. 58). At this break-down point vortices spontaneously start to move, and induce a voltage across the sample in the process. It is possible to separate a typical I-V curve of a SC into three distinct regions: (i) SC region (near zero response to ramping current), (ii) Vortex motion (voltage is induced due to moving vortices), (iii) Ohmic region (SC is completely driven normal). In region

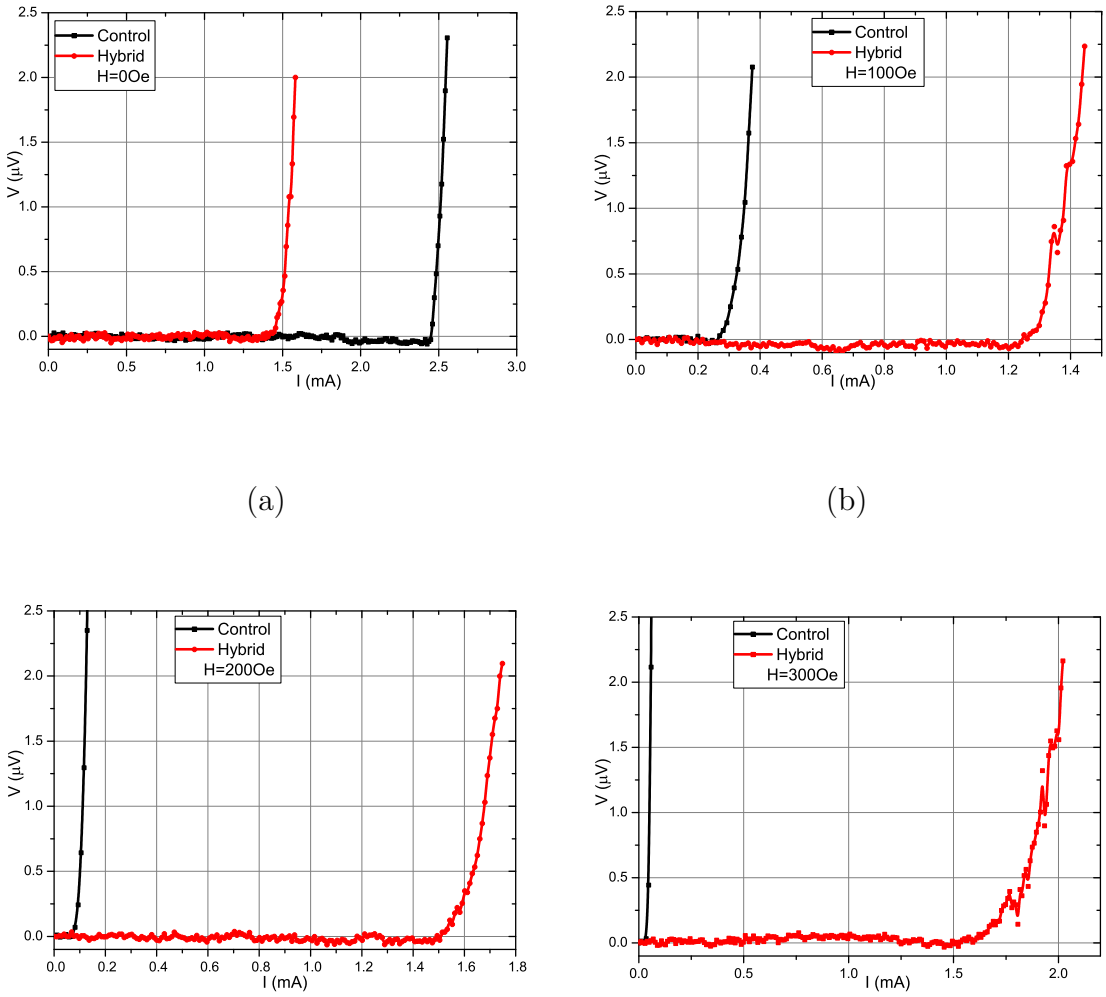

Fig. 58. I-V curves for both control and hybrid sample at $T = 7.6K$ and (a) H=0e, (b) H=100Oe, (c) H=200Og and (d) H=300Oe.

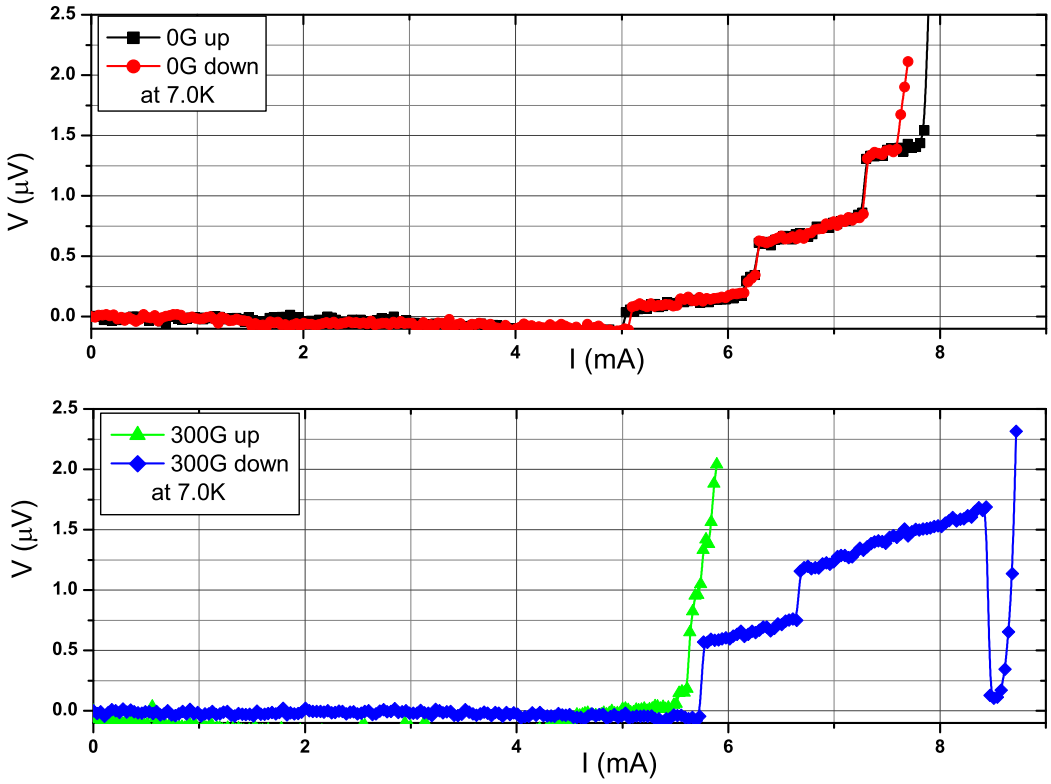

Fig. 59. I-V curves of the hybrid sample at T=7K and $H = 0Oe, 300Oe$ for both anti-parallel (ramp up) and parallel (ramp down) alignment cases.

(i) the pinning forces are stronger than the depinning Lorenz forces; in region (ii) the vortex lattice spontaneously collapses and Lorenz forces on the vortices are stronger than the pinning forces.

The I-V curves in Fig. 59, however, reveal an unusual step like behavior after vortex motion has started. This behavior is never observed in the control film. It appears that large clusters of vortices collapse (a vortex avalanche) due to depinning forces overcoming pinning forces of the artificial pinning sites. There is possibly a variation in the strength of the artificial pinning sites, causing different clusters of vortices to collapse at different current values. This effect decreases as the temper-

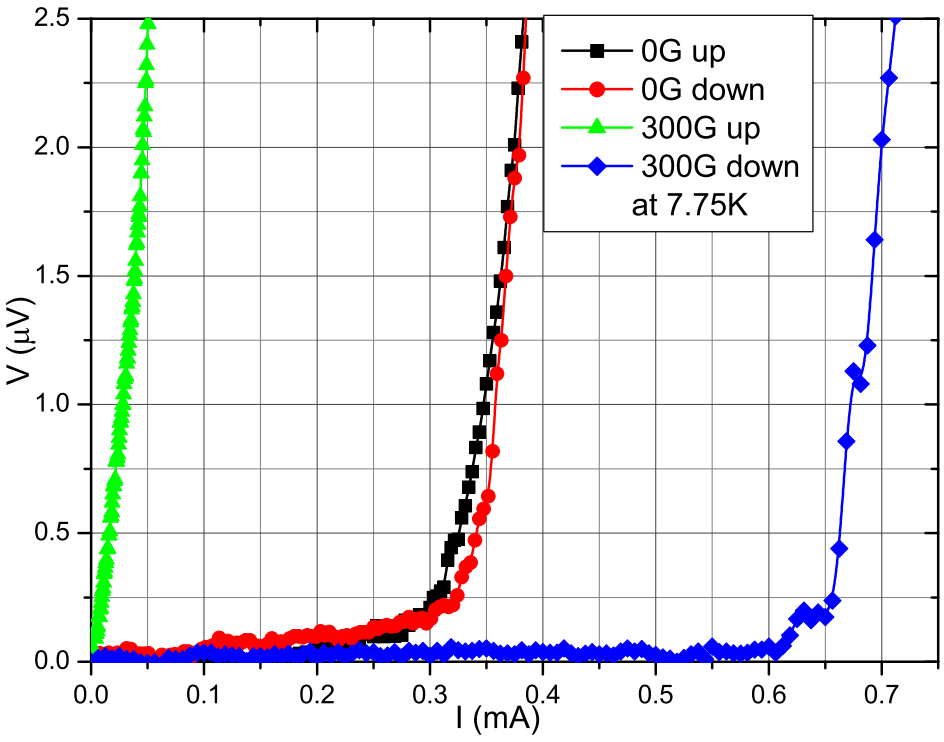

Fig. 60. I-V curves of the hybrid sample at T=7.75K and $H = 0Oe, 300Oe$ for both anti-parallel (ramp up) and parallel (ramp down) alignment cases.

ature approaches T_C (Fig. 60). Vortex size is largest around T_C, thus the pinning due to Ni rods is strongest. Collective depinning in the form of a vortex avalanche is more measurable when the pinning is weaker, in other words when the temperature is further below T_C. Also it is worth mentioning that the fact that the overlapping step-like behavior in the I-V curves (Fig. 59) at zero applied field for both parallel and anti-parallel case is very reassuring for the reliability of the measurements.

CHAPTER VI

CONCLUSION

SHPM is proved to be an effective characterization tool for magnetic sub-structures as well as novel magnetic and superconducting-ferromagnetic hybrid devices. The SHPM system currently has a spatial resolution of about $1\mu m$; thus, it is a sufficient imaging tool for micrometer-size magnetic structures. However for sub-micron magnetic structures or systems with magnetic domain size smaller than a micron, images that the SHPM provides, need to be carefully interpreted and supplemented with MFM. In this dissertation several magnetic structures and devices have been characterized using SHPM and MFM:

(i) A micrometer size permalloy needle with a magnetizing coil was characterized. Images of spacial distribution of magnetic flux density along with $B-H$ and $B-I_{coil}$ data show that the permalloy needle creates a large, controllable magnetic field gradient.

(ii) A square array of 50nm size Ni rods with 2 μm period was characterized. It was demonstrated that it is technically possible to fabricate magnetic nanostructures which generate spatially alternating magnetic fields on the scale of tens of nanometers and with a field strength in the range of 0.1 to 0.7 Tesla.

(iii) A macroscopic iron-brass alternating stripe structure was fabricated. The large period variation of magnetic field at the surface of this structure was observed.

Furthermore, resistivity and critical transport current measurements were performed for SC films deposited on top of three different sets of magnetic substructures. These structures are:

(i) A macroscopic iron-brass alternating stripe structure.

(ii) An array of micrometer size Co stripes.

(iii) An array of 50 nm size Ni rods.

In these studies $R_H(T)$, $H_{C2}(T)$, $I_C(T)$, $I_C(H)$, and $I(V)$ data was reported. It was demonstrated that an inhomogeneous magnetic field can be used to effectively pin vortices in an otherwise homogeneous superconducting film. A variety of novel effects such as enhancement of second critical field H_{C2} and critical transport current I_C, a field compensation effect, a matching field effect and spontaneous vortex avalanches were observed.

REFERENCES

[1] J. Bardeen, L. N. Cooper, J. R. Schrieffer, Phys. Rev. 108 (1957) 1175.

[2] P. G. De Gennes, Superconductivity of Metals and Alloys, New York, (1966).

[3] N. W. Ashcroft, N. D. Mermin, Solid State Physics. (1976).

[4] W. Meissner, R. Ochsenfeld, Naturwiss. 21 (1933) 787.

[5] A. B. Pippard, Physica 19 (1953) 765.

[6] G. Blatter, M.V. Feigelman , V.B. Geshkenbein , A.I. Larkin , V.M. Vinokur, Rev. of Mod. Phys. 66 (1994) 1125.

[7] A. A. Abrikosov, JETP 5 (1957) 1142.

[8] A. A. Abrikosov, L. P. Gorkov JETP 12 (1961) 1243.

[9] V.V. Metlushko, M. Baert, R. Janckheere, V.V. Moshchalkov and Y. Bruynseraede, Solid State Comm. 91 (1994) 331.

[10] M. Baert, V.V. Metlushko, R. Jonckheere, V.V. Moshchalkov and Y. Bruynseraede, Phys. Rev. Lett. 74 (1995) 3269.

[11] V.V. Moshchalkov , M. Baert, V.V. Metlushko, E. Rosseel, M.J. VanBael, K. Temst, R. Jonckheere, Y. Bruynseraede, Phys. Rev. B 54 (1996) 7385.

[12] K. Harada, O. Kamimura, H. Kasai, T. Matsuda, A. Tonomura and V.V. Moshchalkov, Science 274 (1996) 1167.

[13] V.V. Metlushko, L.E. DeLong, M. Baert, E. Rosseel, M.J. Van Bael, K. Temst, V.V. Moshchalkov and Y. Bruynseraede, Europhys. Lett. 41 (1998) 333.

[14] M.J. Van Bael, J. Bekaert, K. Temst, L. Van Look, V.V. Moshchalkov, Y. Bruynseraede, G.D. Howells, A.N. Grigorenko, S.J. Bending and G. Borghs, Phys. Rev. Lett. 86 (2001) 155.

[15] M. Lange, M.J. Van Bael, L. Van Look, K. Temst, J. Swerts, G. Guntherodt, V.V. Moshchalkov and Y. Bruynseraede, Europhys. Lett. 53 (2001) 646.

[16] S.J. Bending, G.D. Howells, A.N. Grigorenko, M. J. Van Bael, J. Bekaert, K. Temst, L. Van Look, V.V. Moshchalkov, Y. Bruynseraede, G. Borghs and R.G. Humphreys, Physica C 332 (2000) 20.

[17] I.F. Lyuksyutov and V.L. Pokrovsky, Adv. in Phys. 54 (2005) 67.

[18] M. Velez, J.I. Martin, J.E. Villegas, A. Hoffmann, E.M. Gonzalez, J.L. Vicent, I.K. Schuller, J. of Magn. and Magn. Mat., 320 (2008) 2547.

[19] M. Lange, M.J. Van Bael, Y. Bruynseraede and V.M. Moshchalkov, Phys. Rev. Lett., 90 (2003) 197006.

[20] T.W. Clinton, M. Johnson, Appl. Phys. Lett., 76 (2000) 2116.

[21] T.W. Clinton P.R. Broussard, M. Johnson, J. of Appl. Phys., 91 (2002) 1371.

[22] D.J. Morgan and J.B. Ketterson, Phys. Rev. Lett. 80 (1998) 3614.

[23] J.I. Martin, M. Velez, J. Nogues and I.K. Schuller, Phys. Rev. Lett. 79 (1997) 1929.

[24] Y. Otani, B. Pannetier, J.P. Nozieres and D. Givord, J. of Magn. and Magn. Mat., 126 (1993) 622.

[25] F. Bitter, Phys. Rev. 38 (1931) 1903.

[26] P. Rice, J. Moreland, Rev. of Scientific Inst., 62 (1991) 844.

[27] L. D. Livingston, J. Appl. Phys., 52 (1981)2506.

[28] N. Saha, R. Surdeanu, M. Marchevsky, G.J. Nieuwenhuys, C.D. Dewhurst, R.J. Wijngaarden, D.M. Paul, P.H. Kes, Phys. Rev. B 63 (2001) 02050.

[29] L.Y. Vinnikov, T.L. Barkov, P.C. Canfield, S.L. Budko, and V.G. Kogan, Phys. Rev. B, 64 (2001) 024504.

[30] C.A. Fowler and E.M. Fryer, Phys. Rev., 92 (1953) 532.

[31] F. Schmidt, W. Rave, and A. Hubert, IEEE Trans. Magn., 21 (1985) 1596.

[32] G. Binning, H. Rohrer , C. Gerber, and E. Weibel, Phys. Rev. Lett., 49 (1982) 57.

[33] K. Itaya, Prog. in Surface Sci., 58 (1998) 121.

[34] H.F. Hess, R.B. Robinson, R.C. Dynes, J.M. Valles Jr., and J.V. Waszczak, Phys. Rev. Lett., 62 (1989) 214.

[35] F. Mielke, U. Memmert, A.A. Golubov, and U. Hartmann, J. Vac. Sci. Technol. B, 14 (1996) 1224.

[36] G. Binnig, C.F. Quate , and C.P. Gerber, Phys. Rev. Lett., 56 (1986) 930.

[37] G. Neubauer, S.R. Cohen, G.M. McClelland, D. Horne and C. Mate; Rev. Sci. Inst., 61 (1990) 2296.

[38] F.J. Giessibl, Rev. of Mod. Phys., 75 (2003) 949.

[39] D. Rugar, H.J. Mamin, R, Erlandsson, J.E. Stern and B.D. Terris, Rev. Sci. Inst., 59 (1988) 2337.

[40] G. Meyer, N.M. Amer, Appl. Phys. Lett., 53 (1988) 1045.

[41] Y. Martin, H. K. Wickramasinghe, Appl. Phys. Lett., 50 (1987) 1455.

[42] J.J. Saenz, N. Garcia, P. Grutter, P. Grtter, E. Meyer, H. Heinzelmann, R. Wiesendanger, L. Rosenthaler, H.R. Hidber, and H.J. Gntherodt, J. Appl. Phys., 62 (1987) 4293.

[43] J.J. Saenz, N. Garcia, J.C. Slonczewski. Appl. Phys. Lett., 53 (1988) 1449.

[44] L. Abelmann, S. Porthun, M.A.M. Haast, J.C. Lodder, A. Moser, M.E. Best, P.J.A. Schendel, B. Stiefel, H.J. Hug, G.P. Heydon, A. Farley, S.R. Hoon, T. Pfaffelhuber, R. Proksch, K. Babcock, J. Magn. Magn. Mater., 190 (1998) 135.

[45] Low Temperature Scanning Hall Probe Microscope (LT-SHPM) Manual Nano-Magnetics Instruments Ltd. Suite 290, 266 Banbury Road, Oxford OX2 7DL UK. Ver. 1.8 Feb. (2006).

[46] S.J. Bending, K.V. Vonklitzing, and K. Ploog, Phys. Rev. B, 42 (1990) 9859.

[47] A.M. Chang, H.D. Hallen, L. Harriot, H.F. Hess, H.L. Kao, J. Kwo, R.E. Miller, R. Wolfe, J. Vanderziel, T.Y. Chang, Appl. Phys. Lett., 61 (1992) 1974.

[48] A. Sandhu, K. Kurosawa, M. Dede, A. Oral, Jap. J. of Appl. Phys., 43 (2004) 777.

[49] R. B. Dinner, M. R. Beasley, and K. A. Moler, Rev. Sci. Inst., 76 (2005) 103702.

[50] M.V. Milosevic, F.M. Peeters, Phys. Rev. B, 68 (2003) 094510.

[51] J.R. Kirtley, C.C. Tsuei, K.A. Moler, V.G. Kogen, J.R. Clem, A.J. Turberfield. Appl. Phys. Lett., 74 (1999) 4011.

[52] P.G. Bjornsson, Y. Maeno, M.E. Huber and K.A. Moler, Phys. Rev. B, 72 (2005) 012504.

[53] H. Bluhm, S.E. Sebastian, J.W. Guikema, I.R. Fisher, K.A. Moler, Phys. Rev. B, 73 (2006) 014514.

[54] J. K. Gregory, S. J. Bending and A. Sandhu, Rev. Sci. Inst., 73 (2002) 3515.

[55] A. Oral, J.C. Barnard, S.J. Bending, I.I. Kaya, S. Ooi, T. Tamegai, M. Henini, Phys. Rev. Lett., 80 (1998) 3610.

[56] G.D. Howells, A. Oral, S.J. Bending, S.R. Andrews, P.T. Squire, P. Rice, A. de Lozanne, J.A.C. Bland , I. KaYa, M. Henini, J. Magn. Magn. Mat., 196 (1999) 917.

[57] K. Urkmen, Scanning Hall probe microscopy (SHPM) using quartz crystal AFM feedback M.S. Thesis (2007).

[58] M. Dede, A. Oral, T. Yamamoto, K. Kadowaki, H. Shtrikman, Jap. J. of Appl. Phys., 45 (2006) 2246.

[59] M.K. Yapici, A.E. Ozmetin, J. Zou, D.G. Naugle, Sens. and Act. A: Physical, 144 (2008) 213.

[60] M.K. Yapici, A.E. Ozmetin, J. Zou, D.G. Naugle, TRANSDUCERS 2007. International, (2007) 2365.

[61] J.Y. Park, M.G. Allen, J. Micromech. Microeng., 8 (1998) 307.

[62] C.S. Lee, H. Lee, R.M. Westervelt, Appl. Phys. Lett., 79 (2001) 3308.

[63] N. Pekas, M. Granger, M. Tondra, A. Popple, M.D. Porter, J. Magn. Magn. Mater., 293 (2005) 584.

[64] M. Berger, J. Castelino, R. Huang, M. Shah, R.H. Austin, Electrophoresis, 22 (2001) 3883.

[65] C.H. Ahn, M.G. Allen, W. Trimmer, Y.N. Jun, S. Erramilli, J. Microelectromech. Syst., 5 (1996) 151.

[66] C.A. Ross, Annu. Rev. Mater. Sci., 31 (2001) 203.

[67] M. Hwang, M.C. Abraham, T.A. Savas, H.I. Smith, R.J. Ram, C.A. Ross, J. Appl. Phys., 87 (2000) 5108.

[68] C.A. Ross, M. Hwang, M. Shima, J.Y. Cheng, M. Farhoud, T.A. Savas, H.I. Smith, W. Schwarzacher, F.M. Ross, M. Redjdal, and F. B. Humphrey, Phys. Rev. B, 65 (2002) 144417.

[69] C. Pike, C.A. Ross, R.T. Scalettar, G. Zimanyi, Phys. Rev. B, 71 (2005) 134407.

[70] D. J. Sellmyer, M. Zheng and R. Skomski, J. Phys. Condens. Matter., 12 (2000) L497.

[71] A.I. Buzdin, Rev. Mod. Phys., 77 (2005) 935.

[72] L.Y. Zhu, T.Y. Chen, C.L. Chien, Phys. Rev. Lett., 101 (2008) 017004.

[73] V. Vlasko-Vlasov, U. Welp, G. Karapetrov, V. Novosad, D. Rosenmann, M. Iavarone, A. Belkin, W.K. Kwok, Phys. Rev. B., 77 (2008) 134518.

[74] Z. Yang, M. Lange, A. Volodin, R. Szymczak and V. V. Moshchalkov, Nature Mater., 3 (2004) 793.

[75] I.F. Lyuksyutov, D.G. Naugle, Modern Phys. Lett. B, 13 (1999) 491.

[76] I.F. Lyuksyutov, D.G. Naugle, Intern. J. Mod. Phys., 17 (2003) 3441.

[77] I.F. Lyuksyutov, D.G. Naugle, Intern. J. Mod. Phys., 17 (2003) 3713.

[78] D. Jaque, E.M. Gonzalez, J.I. Martin, J.V. Anguita, J.L. Vicent, Appl. Phys. Lett., 81 (2002) 2851.

[79] I.F. Lyuksyutov, Mod. Phys. Lett., 16 (2002) 569.

[80] L. N. Bulaevskii, E. M. Chudnovsky and M. P. Maley, Appl.Phys.Lett., 76 (2000) 2594.

[81] A.E. Ozmetin, K.D.D. Rathnayaka, D. G. Naugle, I. F. Lyuksyutov, J. of Appl. Phys., 105 (2009) 07E324.

[82] T. Tosaka, T. Kuriyama, M. Yamaji, K. Kuwano, M. Igarashi, M. Teraiet, IEEE Trans. Appl. Supercond., 14 (2004) 1218.

[83] K. Sawa, M. Suzuki, M. Tomita, M. Murakami, Physica C: Superconductivity, 378 (2002) 803.

[84] M. Tomita, M. Murakami, S. Nariki, K. Sawa, Physica C: Superconductivity, 378 (2002) 864.

[85] M. Tomita, K. Nagashima, M. Murakami, Physica C: Superconductivity, 357 (2001) 832.

APPENDIX

SCANNING HALL PROBE MICROSCOPY

Sample Preparation

This particular SHPM system relies on keeping the tunneling current that flows to the sample surface constant to find and track the surface. It utilizes a fast electronic feedback loop to achieve that purpose. When the sample and the Hall probe chip are in close proximity the tunneling current is achieved between the STM tip and the sample. The STM tip is fabricated on one corner of the Hall probe chip. The Hall probe is also fabricated on chip approximatelly 10μm away from the STM tip (Fig. 61). This assures that the Hall probe is kept as close as possible to the sample without actually contacting the sample surface.

In order to track the surface with the STM, the sample surface needs to be coated with a continuous layer of gold. Coating the sample surface with gold assures that the bias voltage between the STM tip and the sample is uniform throughout the sample. Thermal evaporation is commonly used to coat the sample. Later, the sample is mounted on a gold coated X-Y slider puck with conductive silver paint. Continuity must be established between the gold coated sample surface and the X-Y slider puck by smearing excess silver paint over the sample side to the gold layer on the sample surface. For samples that are smooth and devoid of sharp feature profiles, a 5 to 10 nm thick gold layer is sufficient. If the sample has sharp features or it is not smooth, the thickness of the gold layer must be increased to accommodate possible discontinuities in the gold layer.

The sample surface needs to be cleaned typically with isopropinol and thoroughly dried with clean nitrogen gas. Cleaning the surface with acetone poses some risks to

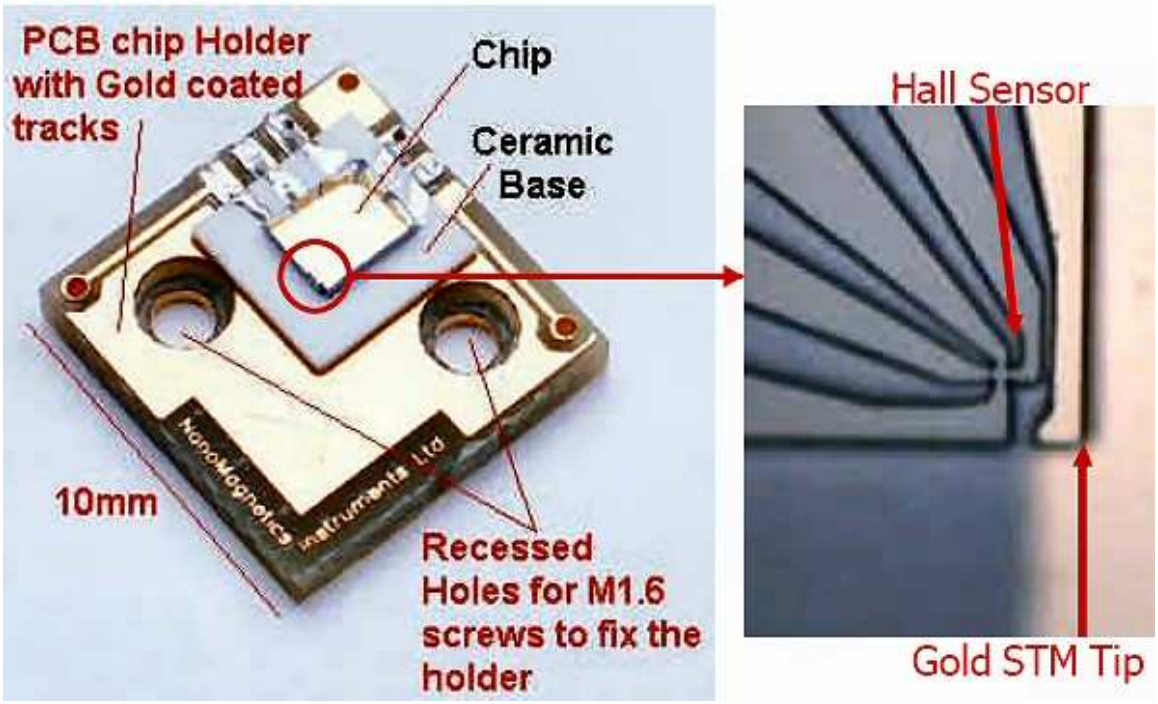

Fig. 61. A photograph of a hall probe chip [45]. Courtesy of NanoMagnetics Instruments Inc. http://web.nanomagnetics-inst.com.

both the continuity of the silver paint and structural integrity of the sample since silver paint and common photoresists are soluble in acetone. If it is necessary to use acetone and other strong solvents, a different type of conductive epoxy should be used to mount the sample.

Sample Mounting and Alignment

Sample Mounting

Once the sample surface is ready, the X-Y slider puck can be mounted on the sample slider puck using a spring loaded set screws (Fig.62). The whole assembly must be thoroughly cleaned and dried. Especially, the brass shim leaf that is used to tighten

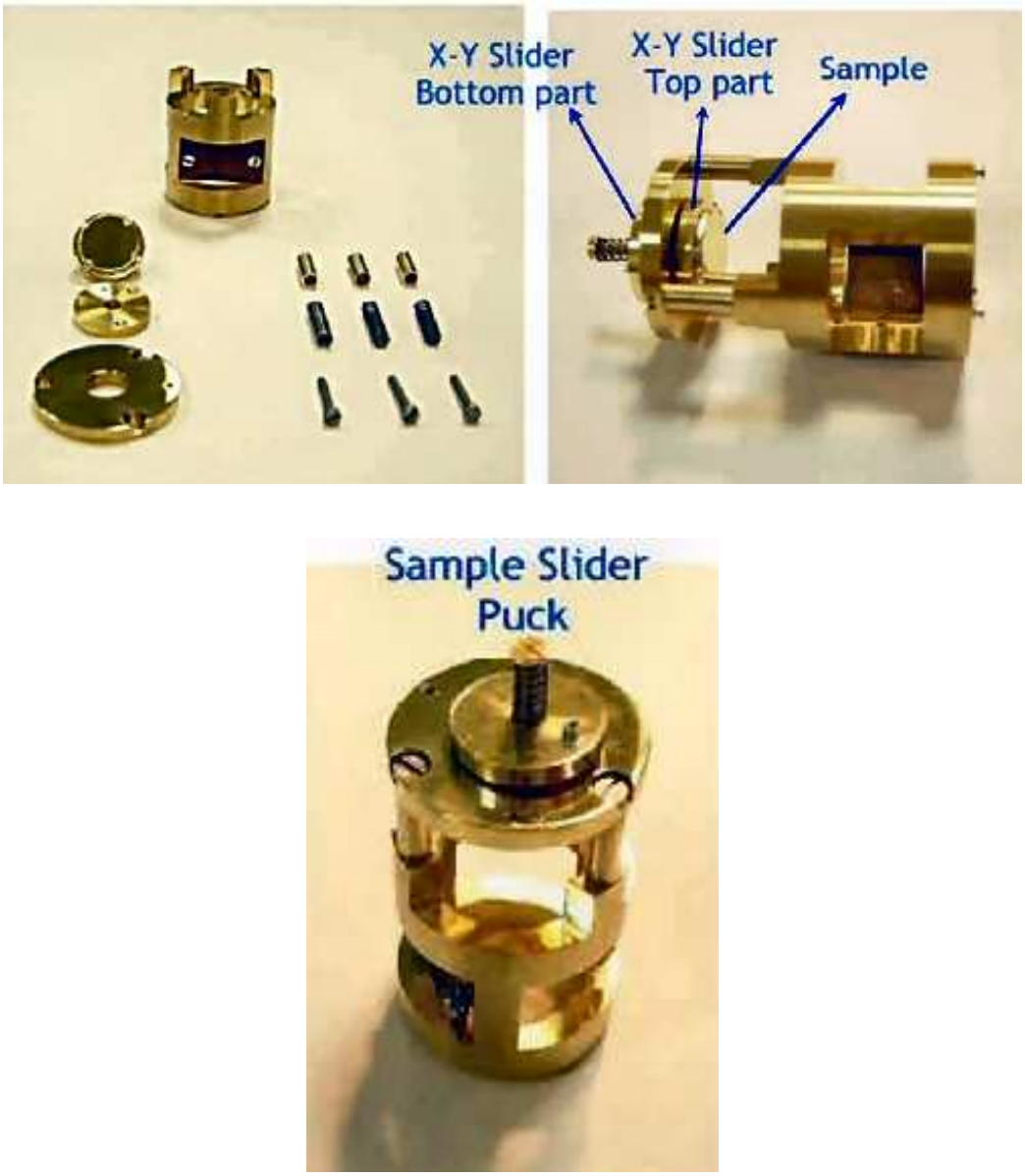

Fig. 62. Sample slider puck and X-Y slider puck assembly. Courtesy of NanoMagnetics Instruments Inc. http://web.nanomagnetics-inst.com.

Fig. 63. Quartz slider tube cleaning. Courtesy of NanoMagnetics Instruments Inc. http://web.nanomagnetics-inst.com.

the slider puck into the quartz slider tube must be extremely clean. The sample slider puck assembly should not be handled with bare hands for low temperature applications. The quartz tube in turn must be cleaned with acetone and wiped with a lint-free cloth as in Fig. 63. Hall probes need to be cleaned in acetone in the ultrasonic bath, rinsed with isopropinol and properly dried each time before they are used. Since gold bond wires are extremely delicate, care must be taken when agitating the Hall probe in the ultrasonic bath and drying it. The sonicater should be operated at a lower power.

In order to mount the Hall probe on the microscope, the microscope is suspended upright on the wooden stand. A protective aluminum shield is placed over the quartz

tube and the Hall probe is mounted on the scanner head with two set screws as in Fig. [64]. Overtightening the set screws must be avoided. At this point, the gold coated brass coil tube can be mounted, and the Hall probe can be checked to ensure proper function before the sample slider assembly is mounted (Fig. 65). When the "check Hall probe" feature is selected in the SPM software, the electronics applies a 10 V sinusoidal signal to the coil. The Hall voltage response and the original signal can be monitored by an oscilloscope. Also a powerful permanent magnet can be moved near to the Hall probe. The Hall voltage response can be checked by flipping the permanent magnet poles.

After a proper Hall probe signal is observed, the brass shield should be removed to mount the sample slider puck as in Fig. [65, 66]. Care must be taken when inserting the sample slider puck as crashing the sample against the Hall probe will permanently destroy the Hall probe. One of the three set screws in the sample slider puck needs to be aligned with Hall probe chip diagonal. This practice makes the sample - Hall probe alignment significantly easier. The brass shim leaf should only be tightened as much as one can tighten it with fingertips without applying extra force.

Adjusting the Sample - Hall Probe Angle

In order to ensure that the STM tip is the closest point of the Hall probe to the surface, the angle between the Hall probe chip plane and the sample surface plane must be adjusted ideally to 1.25^o as in Fig. 67. Since one of the three spring loaded screws located on the top part of the slider puck was aligned earlier to be in line with the Hall probe diagonal, the angle can be adjusted to the desired value by rotating the other two set screws (Fig. 68).

This is generally the most difficult and time consuming part of the preparation process. If the angle is set too shallow, the Hall probe remains too close to the

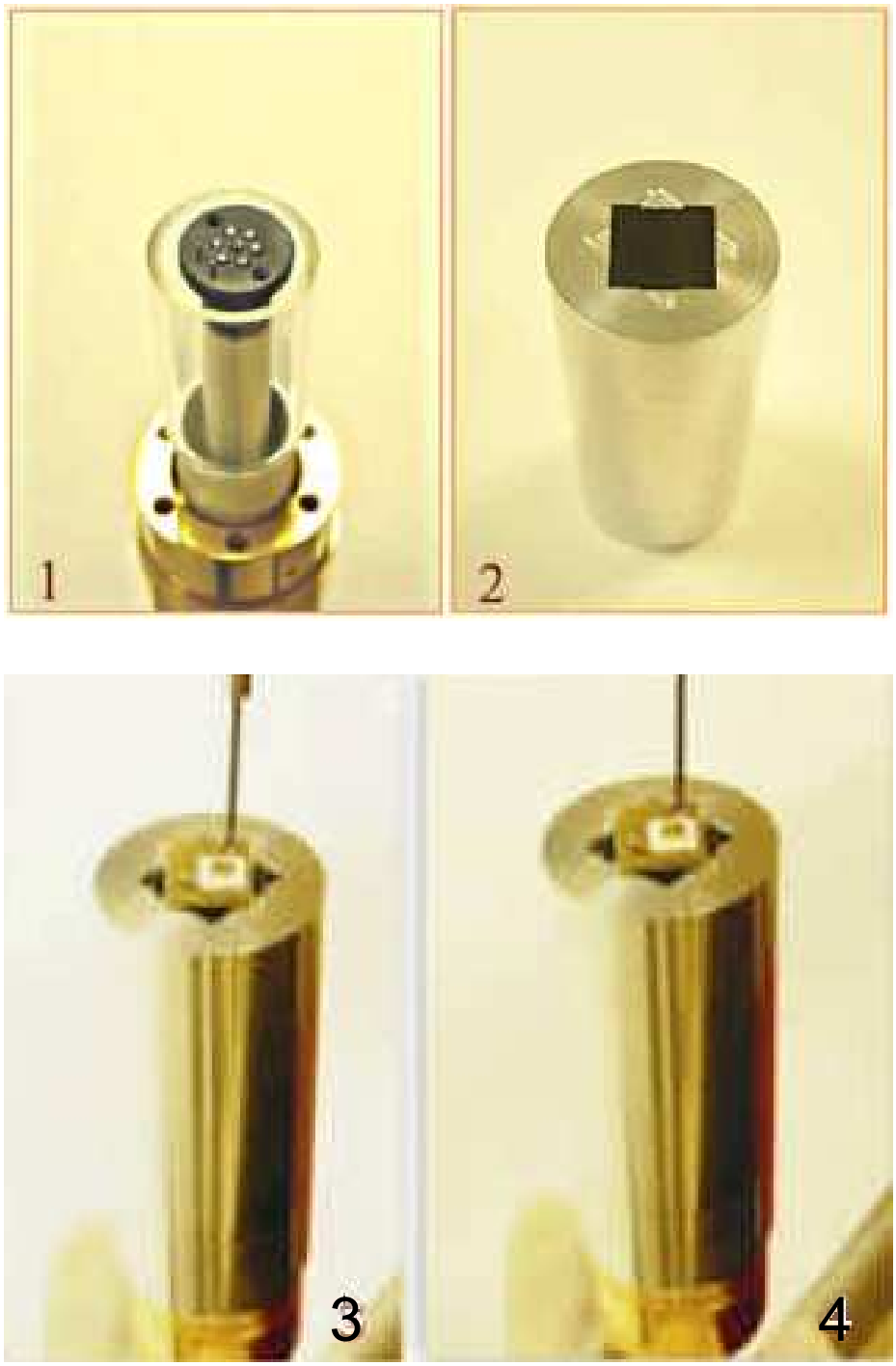

Fig. 64. Mounting hall probe on scanner head. Courtesy of NanoMagnetics Instruments Inc. http://web.nanomagnetics-inst.com.

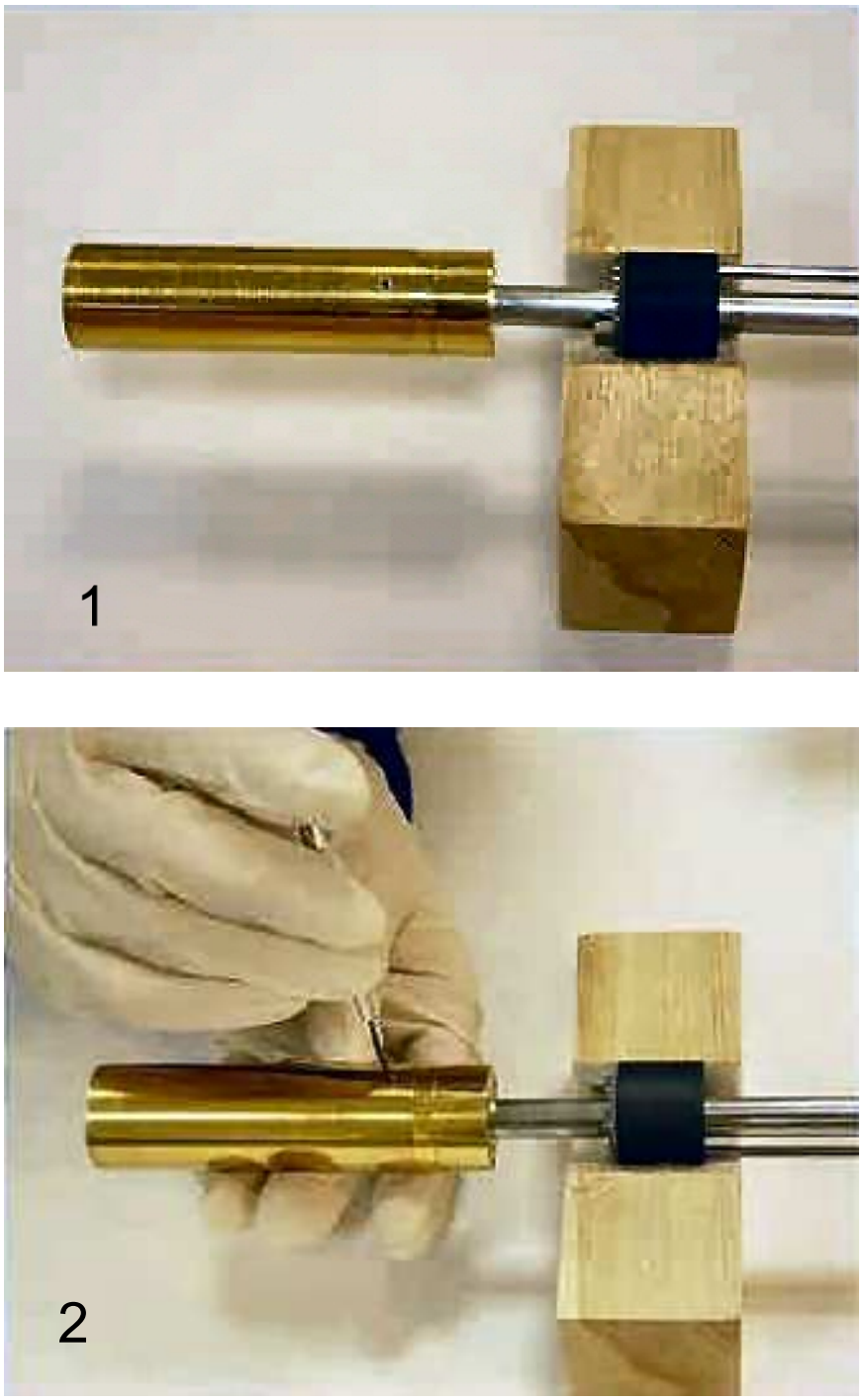

Fig. 65. Brass coil and shield assembly 1-2. Courtesy of NanoMagnetics Instruments Inc. http://web.nanomagnetics-inst.com.

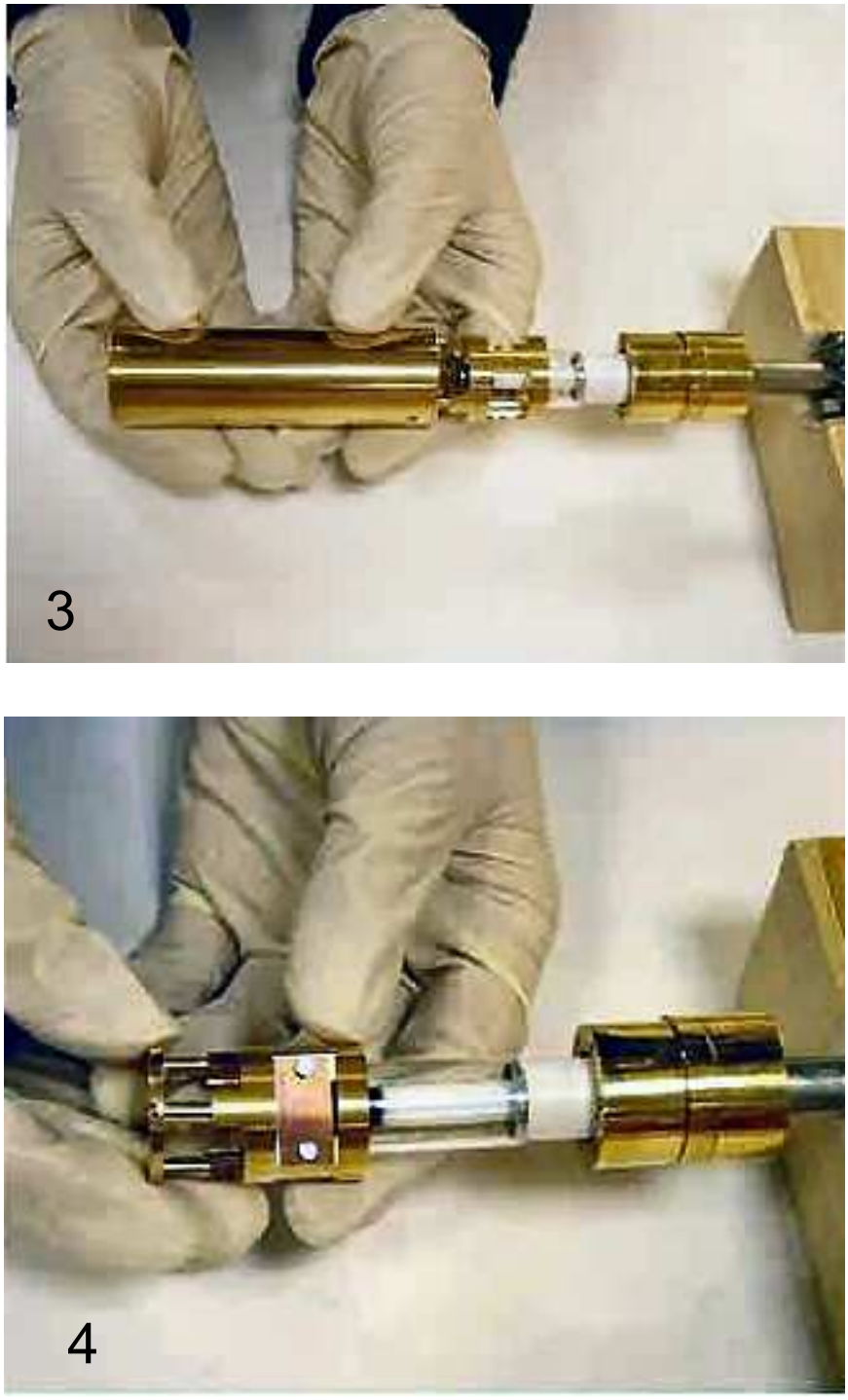

Fig. 66. Brass coil and shield assembly 3-4. Courtesy of NanoMagnetics Instruments Inc. http://web.nanomagnetics-inst.com.

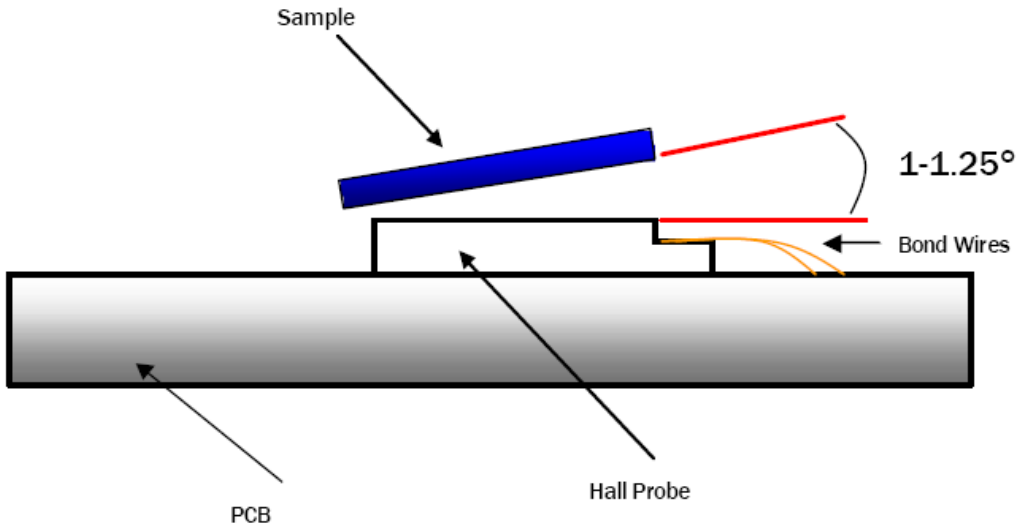

Fig. 67. The proper angle between Hall probe chip and sample planes. Courtesy of NanoMagnetics Instruments Inc.
http://web.nanomagnetics-inst.com.

sample surface and can possibly be damaged. If the angle is too steep, the probe chip corner can hit the surface without the STM tip registering tunneling current and also the Hall probe will also remain too far from the surface resulting in a weaker Hall signal. The Hall probe should be moved near to the sample using the slider stick - slip mechanism to a distance where the user feels comfortable judging the angles. These adjustments must be done while the user is looking at the sample with a microscope from the side. Adjusting the angles correctly is crucial and often a half a turn of the set screws makes the difference between perfect image and no image at all. The user must check the angles repeatedly by rotating the microscope back and forth by 90^o as the adjustment is being made (Fig. 69,70).

Sample Cool Down and Surface Approach

After the sample is correctly aligned and the brass shield placed over the probe, the complete LT-SHPM unit (Fig. 71) can be placed in the PPMS for cool down. Once

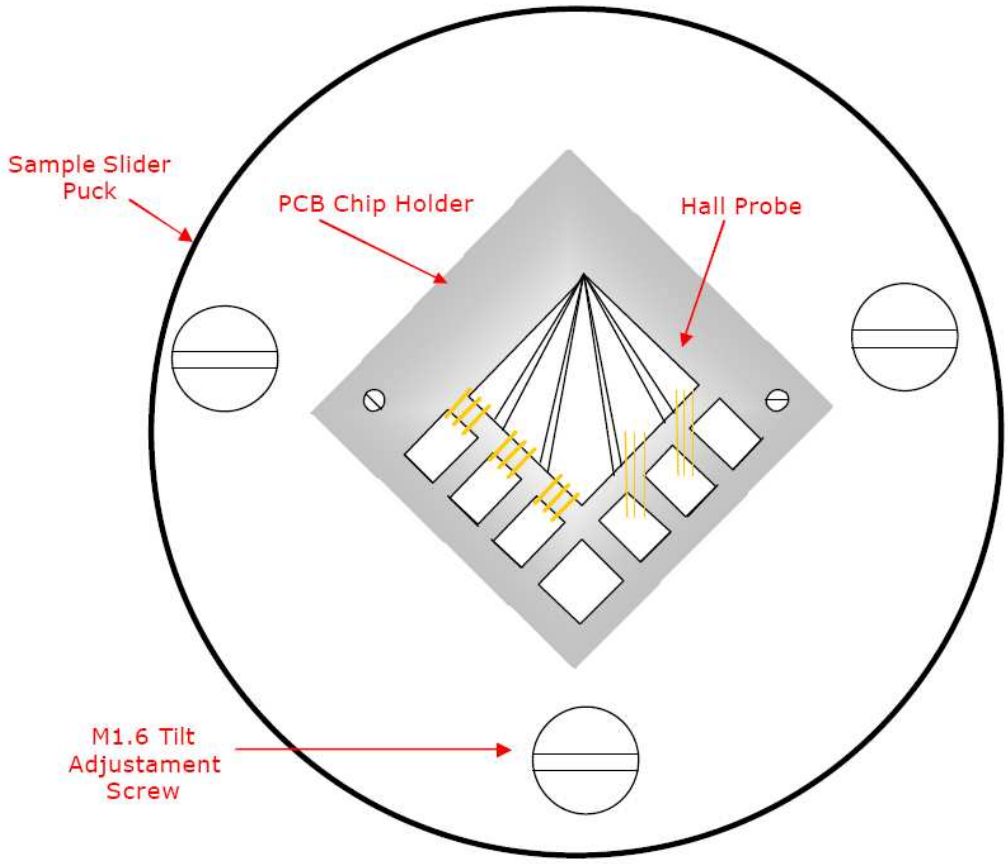

Fig. 68. Top view of sample slider puck. Courtesy of NanoMagnetics Instruments Inc. http://web.nanomagnetics-inst.com.

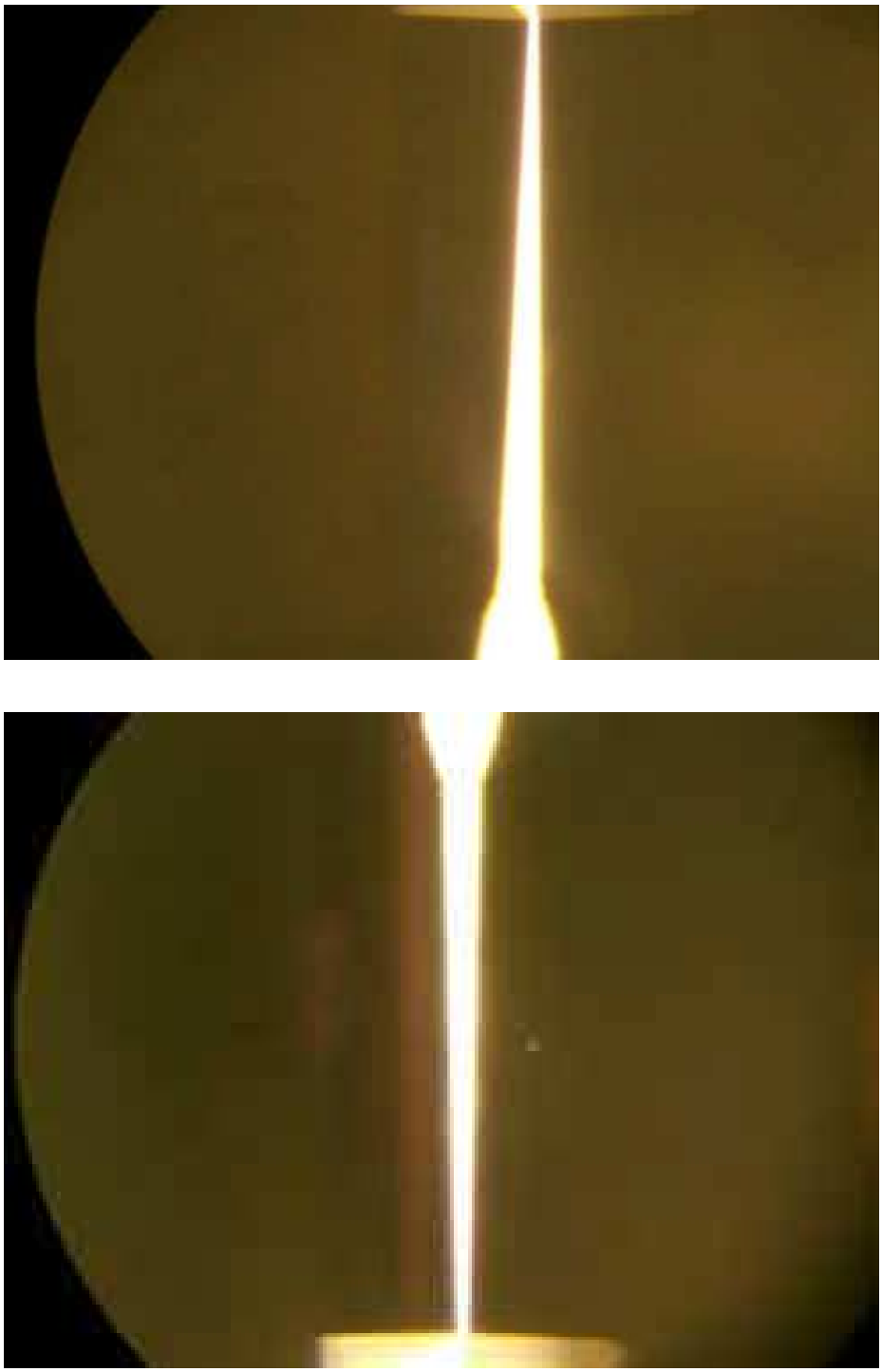

Fig. 69. Hall probe and its reflection on the sample surface with correct angle achieved. Courtesy of NanoMagnetics Instruments Inc. http://web.nanomagnetics-inst.com.

Fig. 70. Observing the Hall probe - sample surface angle with a microscope. Courtesy of NanoMagnetics Instruments Inc.
http://web.nanomagnetics-inst.com.

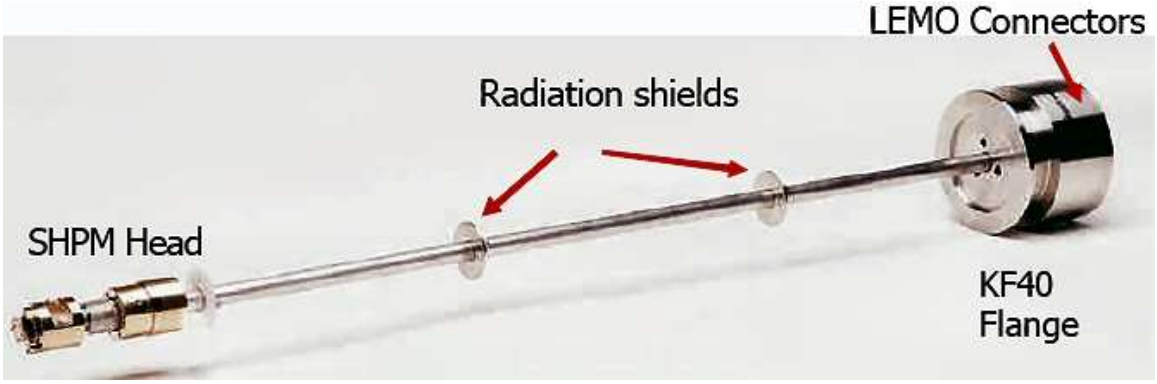

Fig. 71. Complete view of LT-SHPM unit. Courtesy of NanoMagnetics Instruments Inc. http://web.nanomagnetics-inst.com.

the system is carefully placed in the PPMS and several cycles of "purge and seal" are performed, the probe can be approached to the sample. This is achieved by activating "automatic approach" tab. Though, electronics control this part automatically, the user should observe the tunneling signal and overall function of the SPM software. The response speed of the feedback loop is determined by the set value of "feedback loop gain". During the approach this value should never be set over 250, as the approach steps are taken extremely fast for higher values. Once the system finds the surface, a quick scan of the sample can be performed before cool down to assure that the alignment was done properly and sample surface is smooth enough for further scans. If for any reason the "bias voltage" value reads anything other than the set value, the probe head must be withdrawn and system must be thoroughly examined immediately. This occurrence usually indicates a severe misalignment or something on the sample surface shorting to the Hall probe.

Since cooling the sample creates significant physical vibrations, the probe head should be withdrawn several steps and the "automatic retract" option should be selected. The quartz tube that the sample slider puck is mounted on is very sensitive to rapid temperature gradients. Therefore care must be taken during the cool down

and the warm-up processes. Maximum allowed cooling rate is 2 K/min. The built-in diode thermometer mounted near the scanner piezoelectric crystal can be used to monitor the sample temperature with a typical 1μAmp forward current. It takes the sample significantly longer to reach the target temperature than the PPMS system. Therefore, the user should allow extra time for the sample temperature to catch up with the set PPMS temperature. A typical cool down from room temperature to 200K takes about two hours.

Actively using the Hall probe at low temperature (below 50K) depletes the charge carriers. In order to replenish the depleted charge carriers a small UV lamp located near the Hall probe must be turned on for a few seconds.

Scanning the Sample

Scanning the sample in the SHPM can be performed by several distinct methods. Each of these methods is suitable for different imaging scenarios.

STM Tracking Scan

In this method feedback electronics keeps the preset tunneling current constant and moves the Hall probe head up and down. Therefore, the Hall probe remains at the same distance from the surface. By setting the feedback loop gain to its maximum value of 999, reasonably fast images can be achieved. The control electronics generates feedback faster at low temperatures, thus the sample can be scanned progressively faster as the sample temperature drops. Once the surface is located, the system is ready for scanning images. Scans can be started by selecting the "scan multiple images" option from the SPM software. The user determines parameters such as scan speed, scan area, and number of consecutive scans to be performed. Typical STM tracking magnetic and topographical images are shown in Figs. 72, 73. These parameters should be adjusted by the user considering following criteria:

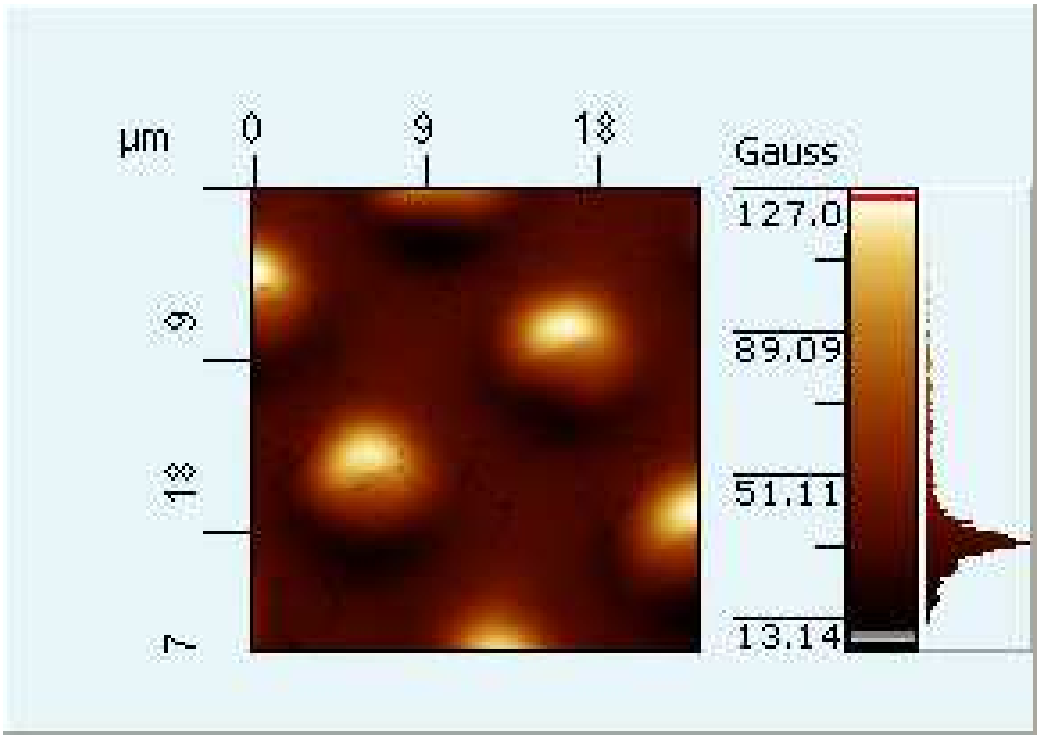

Fig. 72. A typical STM tracking (V_{Hall}) image of an array of $6\mu m$ x $6\mu m$ Co square dots with $12\mu m$ period.

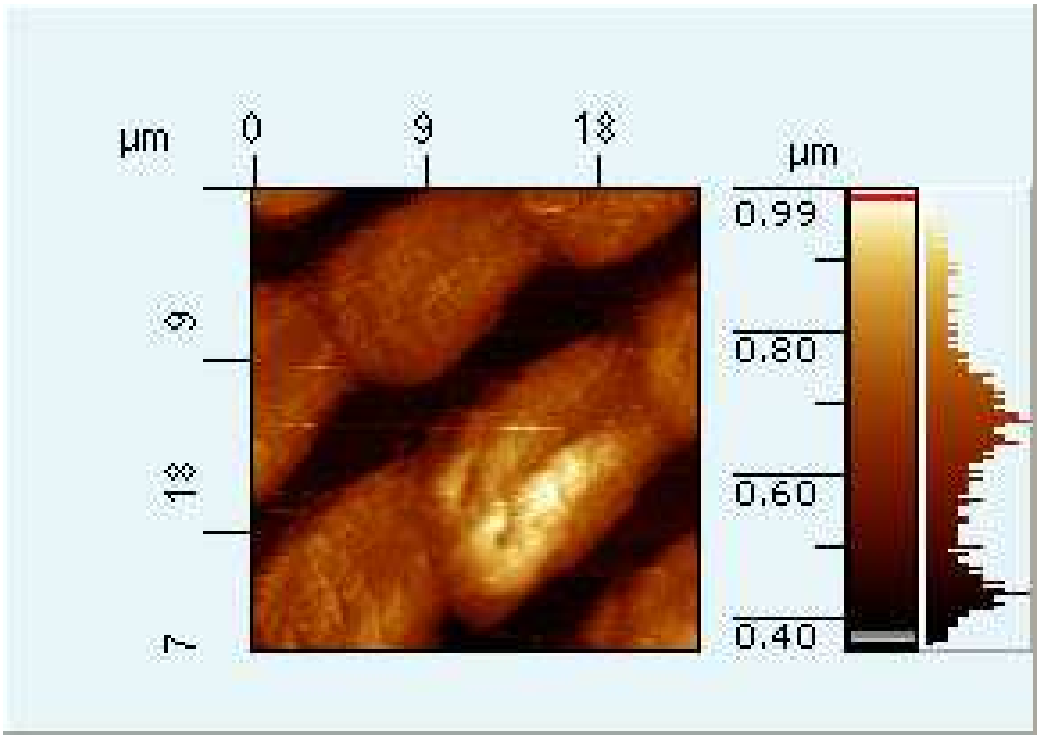

Fig. 73. A typical STM tracking simultaneous (V_Z) image of an array of $6\mu m$ x $6\mu m$ Co square dots with $12\mu m$ period. Image appears diffused due to the dull STM tip.

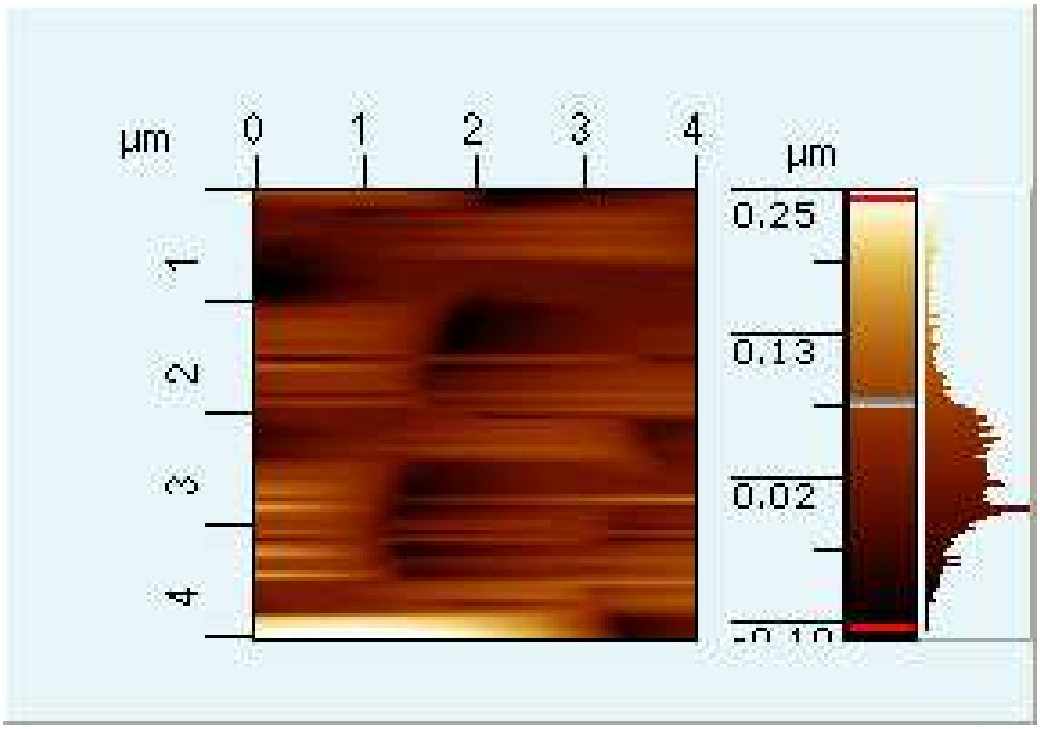

Fig. 74. A smeared V_Z image of Au standard featuring an array of $1\mu m$ x $1\mu m$ pits. This image was acquired too fast.

- For smooth samples a scan speed of 10μm/sec can be achieved at room temperature. The user should lower the speed for rougher samples. At around 100K and below, scanning speeds up to 25μm/sec is possible. Smeared or diffused topographical images usually indicate that the sample is being scanned too fast (Fig. 74). Occasionally the user might deliberately lower the feedback loop gain to slow the system responses to changes in tunneling current. This becomes useful for STM spectroscopy measurements.

- At room temperature, the maximum scan area is 57μm x 57μm Since the response of the piezoelectric crystal to an applied voltage sharply depends on the temperature, necessary size adjustments must be made as the sample temperature changes. The user can calibrate the the piezoelectric crystal by "selecting

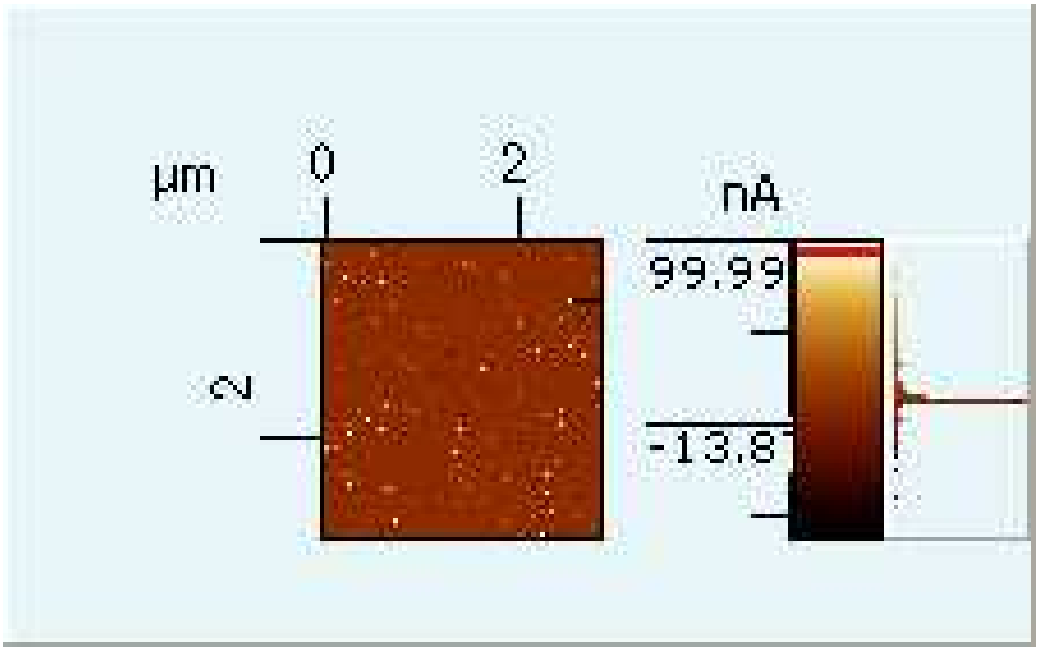

Fig. 75. A typical I_{Tunnel} image of an Au standard featuring an array of $1\mu m$ x $1\mu m$ pits.

PPMS view" and changing the set temperature accordingly. At about 4K, the maximum scan area shrinks to 7.2μm x 7.2μm.

- The user can choose data channels recorded from the "scan multiple images" tab. Among the choices, there are V_{Hall} (magnetic signal) (Fig. 73), V_Z (topography imaging) (Fig. 76), I_{Tunnel} (spectroscopy imaging) (Fig. 75).

Lift-off Fast Scan

In contrast to the STM tracking scan, the user has the option of lifting the probe head by a preset amount and performing a constant probe height scan. In this mode scan speeds up to $30\mu m$/sec can be achieved. On the other hand, since the Hall probe is positioned higher than the STM tracking mode, Hall signals are relatively weaker (Fig. 78(a)). In order to protect the Hall probe, the user must move the probe around

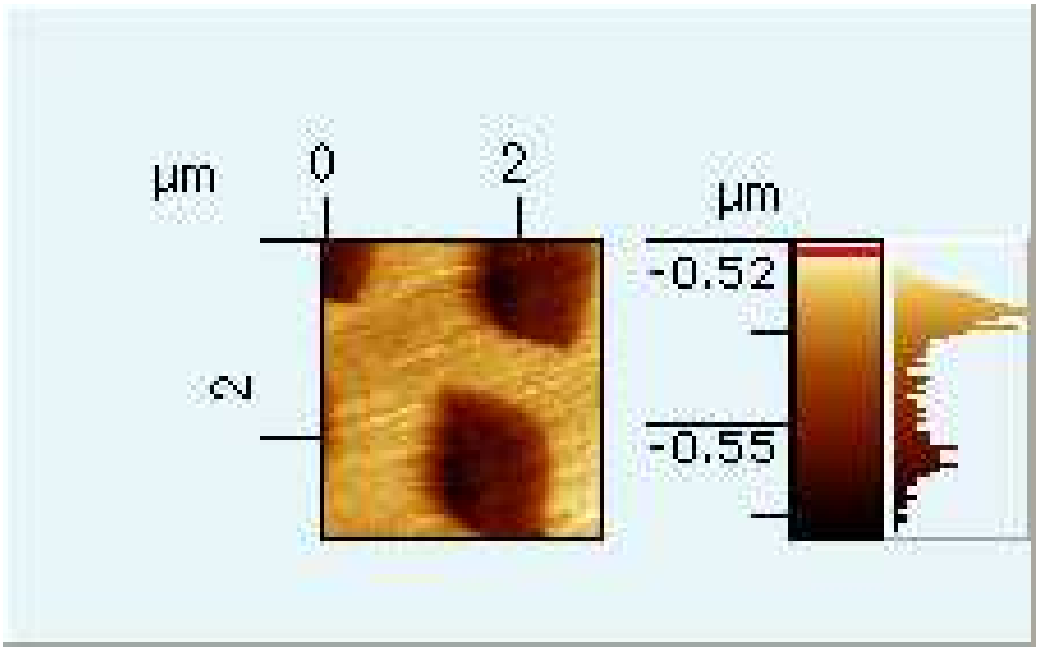

Fig. 76. A typical V_Z image of Au standard featuring an array of $1\mu m$ x $1\mu m$ pits.

the scan area corners and watch the tunneling current on the oscilloscope before the actual scan. If any tunneling signal is observed, the probe must be positioned to the closest point to the sample surface and lifted up for a larger set height.

Lift-off Real-time Scan

Another option, once the probe is lifted off from the sample surface is to perform a real-time scan. Unlike other scan modes, in this scan mode only a signal during forward motion is recorded. In this scan mode a typical 128 x 128 data point image takes about 1.5 sec (Fig. 77, 78). This setting is ideal for observing dynamic changes in surface magnetization such as for imaging vortex motion.

Motor Scan

At room temperature the user has the option of scanning large samples at a constant height using the motor scan option. Since there is no feedback protecting the Hall

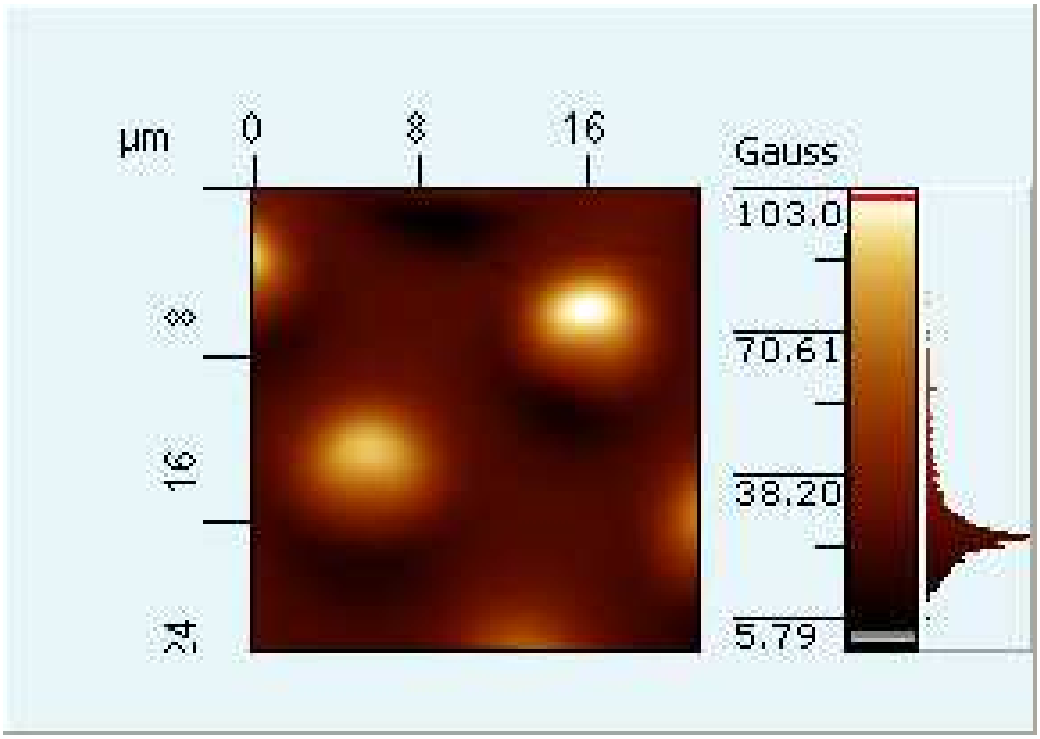

Fig. 77. A typical lift-off fast scan (V_{Hall}) image of an array of $6\mu m$ x $6\mu m$ Co square dots with $12\mu m$ period.

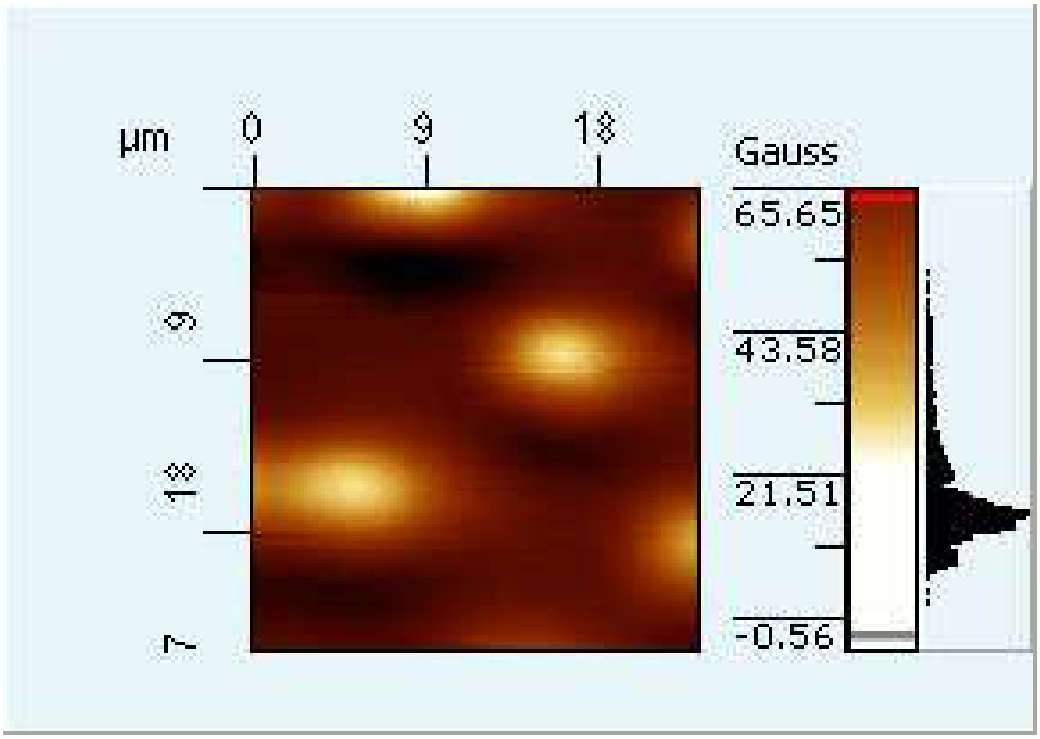

Fig. 78. A typical lift-off real-time (V_{Hall}) image of an array of $6\mu m$ x $6\mu m$ Co square dots with $12\mu m$ period.

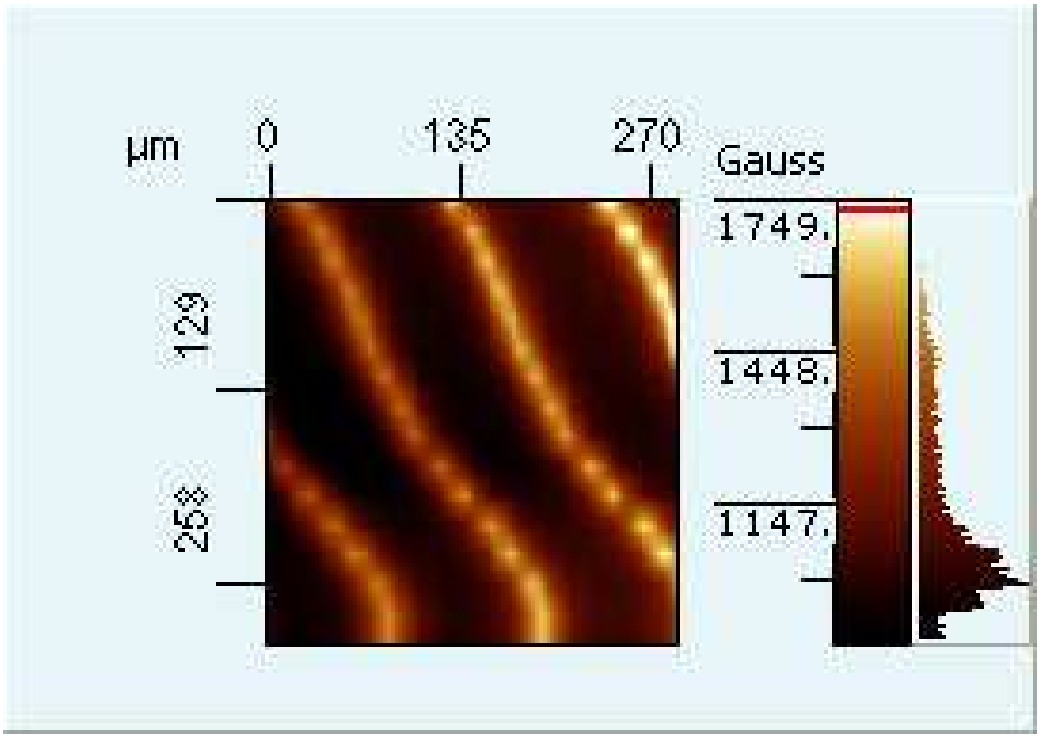

Fig. 79. A typical motor scan V_{Hall} image of laminated $25\mu m$ iron and $250\mu m$ brass alternating shim stock.

probe, the user must take great care to ensure that the probe head is high enough from the sample surface. Images acquired with this option are extremely slow and can take hours to finish. The user determines the parameters such as scan step size and image resolution. As an example, the image in Fig. 79, covers a scan area of $300\mu m$ x $250\mu m$ and takes about one hour to complete.

VITA

Ali Esad Ozmetin was born in 1973, to Hayrettin and Gulsen Ozmetin in Samsun, Turkey. He received his B.S. degree in physics from Bogazici University in 1995. He received his M.S. degree in physics and Ph.D. degree in materials science and engineering from Texas A&M University in 2002 and in 2009.

Department of Physics

c/o Dr. Donald Naugle

Texas A&M University,

College Station, TX 77843-4242